



저작자표시-비영리-변경금지 2.0 대한민국

이용자는 아래의 조건을 따르는 경우에 한하여 자유롭게

- 이 저작물을 복제, 배포, 전송, 전시, 공연 및 방송할 수 있습니다.

다음과 같은 조건을 따라야 합니다:



저작자표시. 귀하는 원저작자를 표시하여야 합니다.



비영리. 귀하는 이 저작물을 영리 목적으로 이용할 수 없습니다.



변경금지. 귀하는 이 저작물을 개작, 변형 또는 가공할 수 없습니다.

- 귀하는, 이 저작물의 재이용이나 배포의 경우, 이 저작물에 적용된 이용허락조건을 명확하게 나타내어야 합니다.
- 저작권자로부터 별도의 허가를 받으면 이러한 조건들은 적용되지 않습니다.

저작권법에 따른 이용자의 권리는 위의 내용에 의하여 영향을 받지 않습니다.

이것은 [이용허락규약\(Legal Code\)](#)을 이해하기 쉽게 요약한 것입니다.

[Disclaimer](#)

약학박사학위논문

종양미세환경 특이적
나노구조체 기반 약물전달
Tumor microenvironment specific
nanostructure-based drug delivery

2018 년 8 월

서울대학교 대학원
약학과 약제과학전공
진혜림

Abstract

Tumor microenvironment specific nanostructure-based drug delivery

Hyerim Jin

Physical Pharmacy, Department of Pharmacy

The Graduate School

Seoul National University

Tumor microenvironment (TME) is composed of tumor tissue and its related immune cells, extracellular matrix and secreted proteins. TME is one of the critical factors for disease treatment and it has been attracting the interest of scientists. Targeted drug delivery originally has the highly expressed proteins

on tumor cells and its targetable range has been expanded to TME. Recently, TME specific targeted drug delivery has been rising as promising strategy for improving anticancer treatment efficiency and the applicable field is getting bigger. First, DNA nanostructure was formed by self-assembly using successive 15 guanine sequence extended to the end of DNA aptamer sequence which can specifically bind to protein tyrosine Kinase 7 (PTK7). Methylene blue (MB) was loaded into the G-quadruplex based DNA nanostructure and the complex showed significantly high delivery effect only to PTK7 overexpressing cancer cells. Then the LED irradiation was followed to generate reactive oxygen species (ROS) and resulting in effective cancer cell killing. Secondly, chlorin e6 (Ce6) having cyclic peptide was designed for loading onto reduced graphene oxide (rGO) nanosheets. The peptide was delivered to and cleaved at cathepsin L enzyme-rich TME. Then targetable peptide was activated to recognized the cancer cell surface proteins and receptor mediated endocytosis occurred. NIR irradiation generated hyperthermia at rGO accumulated tumor cell. The photothermal therapy (PTT) showed complete tumor ablation. Lastly, tight junction (TJ) was selected for targeted drug delivery. TJ is the main protein which limits drug delivery to center of tumor mass. TJ binding peptide was loaded onto rGO nanosheets and the TJ disruption-mediated drug delivery efficiency was

evaluated in cell spheroid models and tumor bearing mice models.

Keywords: Tumor microenvironment, targeted drug delivery, DNA nanostructure, reduced graphene oxide, photodynamic therapy, photothermal therapy, tight junction, penetration depth

Student Number: 2013-21618

Contents

Abstract	i
Contents	v
List of Tables	viii
List of Figures	ix
List of Abbreviations	xiii

Chapter I. Overview

1. Introduction.....	2
2. Tumor microenvironment.....	4
3. Active drug delivery system.....	9
4. Scope of the studies.....	14
5. References.....	16

Chapter II. Stemmed DNA nanostructure for selective delivery of therapeutics

1. Introduction.....	35
2. Materials and methods.....	37

3. Results	46
4. Discussion	71
5. References	76

Chapter III. Serial-controlled delivery of nanomaterials by sequential activation in tumor microenvironment

1. Introduction	84
2. Materials and methods	86
3. Results	97
4. Discussion	118
5. References	121

Chapter IV. Enhanced delivery of nanomaterials by overcoming inter-cellular junction at tumor microenvironment

1. Introduction	127
2. Materials and methods	129
3. Results	139
4. Discussion	156
5. References	160

Conclusion.....**165**

국문초록.....**167**

List of Tables

Table I -1. Tumor microenvironment-rich cytokines for active drug delivery

Table I -2. Strategies for improving drug delivery efficiency

Table I -3. Recognizing strategies for proteins on tumor cell surfaces

Table I -4. Stimuli-controllable active drug delivery

List of Figures

- Fig. II -1.** Oligodeoxynucleotide sequences and schematic structures
- Fig. II -2.** Electrophoresis and circular dichroism (CD) spectroscopy
- Fig. II -3.** TEM imaging and Raman spectroscopy
- Fig. II -4.** NMR spectra of stemmed DNA nanostructures
- Fig. II -5.** The morphologies of gold-incorporated DNA nanostructures
- Fig. II -6.** Binding of MB to DNA nanostructures
- Fig. II -7.** DOX loading onto stemmed DNA nanostructures
- Fig. II -8.** MTO loading onto stemmed DNA nanostructures
- Fig. II -9.** PPIX loading onto stemmed DNA nanostructures
- Fig. II -10.** *In vitro* reduction of target PTK7 expression
- Fig. II -11.** Cellular uptake of MB/AptG15 in PTK7-negative, PTK7-knockdown, and PTK7⁺-positive cells
- Fig. II -12.** Cellular uptake of various drugs delivered by AptG15
- Fig. II -13.** ROS production of PTK7-negative, -knockdown and ⁺-positive cells

- Fig. II -14.** ROS production of PTK7-negative, PTK7-knockdown and PTK7 γ -positive cells upon LED irradiation
- Fig. II -15.** Photodynamic anticancer activity of DNA-nanostructure-treated PTK7-negative, -knockdown and γ -positive cells
- Fig. II -16.** ROS production-inducing cell killing effect
- Fig. II -17.** Schematic of the mechanism for the delivery and therapeutic effect of MB/AptG15
- Fig. III-1.** Nanostructure of CUP loaded rGO and a schematic illustration of mechanism of action
- Fig. III-2.** Synthesis scheme of PEG₂₀₀₀-Ce6 conjugated peptide
- Fig. III-3.** Size and zeta potentials of the surface-modified rGO nanosheets
- Fig. III-4.** Loading amount of peptides onto rGO nanosheets
- Fig. III-5.** Enzyme cleavable activity analysis on TCMK-1, CCRF-CEM, and HT-29 cells
- Fig. III-6.** UPAR expression and targeting efficacy of CUP/rGO
- Fig. III-7.** Uptake of CUP/rGO nanosheets in UPAR positive cancer cell

- Fig.III-8.** Photothermal activities of the surface-modified rGO following treated to cells
- Fig.III-9.** Photothermal anticancer effects
- Fig.III-10.** Biodistribution of Ce6 conjugates-loaded rGO in tumor-bearing mice
- Fig.III-11.** Photothermal effect of the CUP/rGO in mice
- Fig.III-12.** Immunohistochemistry of laser irradiated tumor tissues after various rGO treatment
- Fig.IV-1.** Schematic diagram
- Fig.IV-2.** Claudin4 expression
- Fig.IV-3.** Cleavage activity of cell secreting enzyme
- Fig.IV-4.** Cytotoxicity of tight junction opening peptide
- Fig.IV-5.** TJ peptide effect on TEER value
- Fig.IV-6.** In vitro photothermal effect on spheroids

Fig.IV-7. In vitro anticancer effect

Fig.IV-8. Penetration analysis on cell spheroids

Fig.IV-9. Biodistribution of MEPTJ peptide loaded rGO nanosheets

Fig.IV-10. In vivo penetration evaluation of TJ peptide

List of Abbreviations

Abbreviation	Word
ANOVA	analysis of variance
Apt	aptamer
AptC15	aptamer with cytosine 15
AptG15	aptamer with guanine 15
BSA	bovine serum albumin
CCL	chemokine ligand (C-C motif)
CD	circular dichroism
Ce6	chlorin e6
CSP	CTSL cleavable and UPAR scrambled peptide
CTSL	cathepsin L
CUP	CTSL cleavable and UPAR peptide
CXCL	chemokine ligand (C-X-C motif)
Cy5.5	cyanin 5.5 dye
DAPI	4',6-diamidino-2-phenyl- indole dihydrochloride
DMF	dimethylformamide
ECM	Extracellular matrix

EPR	enhanced permeability and retention
EGFR	epidermal growth factor receptor
FBS	fetal bovine serum
FITC	fluorescence isothiocyanate
Fmoc	fluorenylmethyloxycarbonyl
GO	graphene oxide
HER	human epidermal growth factor receptor
HPLC	high performance liquid chromatography
LED	light-emitting diode
LOX	lysyl oxidase
LRP	lipoprotein receptor-related protein
MB	methylene blue
MDSC	myeloid-derived suppressor cell
MEP	meprin cleavable peptide
MEPTJ	MEP with tight junction binding peptide
MEPTJ/rGO	MEPTJ loaded rGO
MMP	matrix metalloproteinase
MTT	3-(4, 5-dimethylthiazol-2-yl)

	-2,5-diphenyltetrazolium bromide
NIR	near infrared
PBS	phosphate buffered saline
PCNA	proliferating cell nuclear antigen
PDGF	platelet-derived growth factor
PEG	polyethylene glycol
PSMA	prostate specific membrane antigen
PTK7	protein tyrosine kinase 7
PTT	photothermal therapy
rGO	reduced graphene oxide
ROS	reactive oxygen species
SP	UPAR scramble peptide
ScrG15	PTK7 scramble with guanine 15
siPTK7	PTK7-silencing RNA
ssDNA	single stranded DNA
TDW	triple distilled water
TEER	trans epithelial electrical resistance
TEM	transmission electron microscopy
TfR	transferrin receptor
TIMP	tissue inhibitor of

	metalloproteinase
TJ	tight junction binding peptide
TME	tumor microenvironment
TUNEL	terminal deoxynucleotidyl transferase dUTP nick-end labeling
UP	UPAR binding peptide
UPAR	urokinase-type plasminogen activator receptor
VEGF	vascular endothelial growth factor

Chapter I

Overview

1. Introduction

Targeted drug delivery has been developed for enhancing therapeutic delivery efficacy with minimizing normal cell damage. Overexpressed proteins on tumor cell surface are the major targeting site of drug loaded cargos. As the ligand for the target protein, nucleic acid based aptamer, short peptide sequence or small proteins are widely characterized. Conventionally, tumor cell receptor mediated drug endocytosis was the core mechanism in the drug delivery field. Significant tumor cell targeting and its anticancer effect was analyzed. However, the limited delivery efficiency are remaining problem and it is understood as the effect of biological barriers.

Tumor microenvironment is the structure constructed by broad types of cells and their surrounding architectures. The heterogeneous cells requires multi targeting ability of drug loaded materials. The complex architecture ECM requires softening of pressure and tumorous condition (hypoxia, acidic pH) recognizing system.

Stimuli-responsive materials have been reported as promising anticancer therapeutical strategy. Anticancer drugs or silencing of cancerous genes showed limitations of complete cancer treatment. However, administered photoresponsive materials within drug carrier can induce heat-mediated or reactive oxygen species (ROS)-mediated therapeutic effects. These external

stimuli attracts the interests of scientist that it can treat cancer neighbor lesion as well as cancer cells with requiring small amount of anticancer drug.

2. Tumor microenvironment

Tumor microenvironment (TME) consists of various types of cells and noncellular components. The cells include cancer cells, endothelial cells, fibroblasts, immune cells and noncellular components include extracellular matrix (ECM), growth factors such as VEGF, TGF- β , PDGF, enzymes such as matrix metalloproteinase (MMPs), tissue inhibitors of metalloproteinases (TIMPs), lysyl oxidase (LOXs). Collectively, these cellular and noncellular factors interact each other to construct extraordinary network which is optimal for tumor cell growth, migration and invasion as well.

2.1. Environmental rich component

Extracellular matrix (ECM) is an integral compartment existing in all types of tissues. ECM shows tissue-type dependent variation and its composition is responsible for maintaining tissue homeostasis as well as cell supporting function [1]. ECM proteins can be classified into two groups; fibrous proteins and proteoglycans. Fibrous proteins include collagen [2,3], fibronectin [4], tenascin [5] and laminin. Proteoglycans consist of decorin, lumican, versican and hyaluronan [6].

On the other hand, dysregulation of ECM components is implicated in various cancer progression because the irregular ECM condition is the main

characteristic found in cancer patient derived tissues. The ECM remodeling is led by tumor cells through promoting secretion or inhibition of ECM components and it results in tumorigenic environment where tumor cell could survive well [7]. Major enzymes playing ECM remodeling are MMP [8], LOX [9] and hyaluronidase [10]. Moreover, various chemokines at TME play the critical roles in either protumor or antitumor effect. The chemokines modulate tumor vascularization [11], cancer cell invasion and metastasis [12,13], or recruitment of immune cells [14-17] for tumor progression. Some chemokines increase immunogenicity of tumor [18] or inhibition of angiogenesis [19] to suppress the tumor growth. These TME-rich chemokines have been novel target which can synergistically recognize target lesion and further treatment. For ultimate cancer treatment, understanding of the role of the ECM and the mechanism of cancerous cell inducing ECM variation is required.

Table I -1. Tumor microenvironment-rich chemokines for active drug delivery

	Chemokine	Effect on tumor cells	Effect on immune cells	Reference
Pro-tumor effect	CCL2	Tumor vascularization	Recruitment of monocytes and natural killer cells	[11]
	CCL3	Cancer extravasation	Recruitment of monocytes and macrophages	[20]
	CCL5	Cancer invasion		[21]
	CCL18	Cancer invasion and metastasis		[12]
	CCL25			[13]
	CXCL8	Resistance to hypoxia	Recruitment of neutrophils	[14]
	CXCL12	Proliferation, survival	Recruitment of B cells	[15]
	CXCL14	Cancer invasion and motility	Recruitment of dendritic cells	[16]
CXCL17	Angiogenesis	Recruitment of granulocytic myeloid-derived suppressor cells (MDSCs)	[17]	
Anti-tumor effect	CXCL8	Improve immunogenicity of tumor	Recruitment of neutrophils and granulocytic MDSCs	[18]
	CXCL9, CXCL10	Angiogenesis inhibitor	Recruitment of T cells and natural killer cells	[22]
	CXCL14	Proliferation inhibition	Recruitment of dendritic cells	[19]

2.2. Strategy for overcoming ECM barrier

The high density and heterogeneity of ECM restrict drug delivery to tumor site. To enhance the delivery efficacy, tumor targeting has been widely studied but it is limited to the tumor surface protein targeting for cell-type specific internalization of administered drug. Some studies concentrated on increasing drug delivery to complex tumor ECM. Inhibition of tumor neoangiogenesis [23] and alteration of endothelium barrier [24] modified blood flow to tumor site [25-29]. By agonizing bradykinine [30] or targeting vascular endothelial growth factor (VEGF) [28,31] or targeting platelet-derived growth factor (PDGF) [32,33], the interstitial fluid pressure was adjusted [34]. Also, collagenase or relaxin decreased ECM compactness [35-38]. Further studies are required for enhanced drug loaded nanomaterial delivery by overcoming tumor ECM environment.

Table I -2. Strategies for improving drug delivery efficiency.

Target	Purpose	Mechanism	Reference
Tumor blood flow	Neoangiogenesis inhibition	Pseudonormalization of tumor vessel	[25-27]
Tumor blood permeability	Tumor endothelium damage	Alternation of endothelial barrier function	[28,29]
Interstitial fluid pressure (IFP)	VEGF	Vessel permeability decrease	[28,31]
	Bradykinin	Increase of pore size at tumor vessel	[30]
	PDGF-beta	Decrease of stromal cell-ECM interaction	[32,33]
ECM	ECM degradation	ECM remodeling for antiadhesive effect	[35-38]

3. Active drug delivery systems

3.1. Carriers

Nano-ranged carriers have been widely developed to deliver therapeutic agents to interested biological sites. The nanocarriers show negligible internal toxicity and enhanced protection ability for loaded agents against enzymatic or biological degradation. Due to their easy loading process and superior enhanced permeability and retention (EPR) effect on existing microcarriers [39], the nanocarriers have been actively utilized for optical imaging, magnetic resonance imaging [40], and cancer therapy [41]. It is well known that intracellular drug delivery into tumor cells depends on the physicochemical and morphological properties of the drug carriers as well as pathophysiological characteristics of the organism and tumor microenvironment. The ideally standardized nanocarriers are graphene oxide [42,43], DNA architecture [44,45], liposomes [46], polymer nanoparticles [47], polymer micelles [48] and they are comprised of GO, DNA, phospholipids and cholesterol, polymers, or metals, respectively [49].

3.2. Targeting moiety

Various proteins expressed at high density on tumor cell surface or cancer vasculature have been identified as potential targets to enhance the therapeutic effect of active drug delivery [50]. Major mechanisms include ligand-receptor binding, antigen-antibody binding and biomimicking or synthetic materials for molecular recognition [51]. For cancer treatment, several kinds of targeting moieties, such as antibody, aptamer or peptide, are dynamically utilized (Table I -3). Significant expression on cancer cell surface proteins such as HER2 [52,53], EGFR [54,55], TfR [56,57], PSMA [58-61], PTK7 [62,63] are the main targets. Delivering drug molecules to specific disease locations demonstrates the therapeutic advance with eliminating the possible toxicity to healthy tissues [64,65].

Table I -3. Recognizing strategies for proteins on tumor cell surfaces.

	Targeting moiety	Target	Target disease	Reference
Anti body	Trastuzumab	Human epidermal growth factor receptor2 (HER2 receptor)	Breast cancer	[52,53]
	Cetuximab	Epidermal growth factor receptor (EGFR)	Epithelial cancer	[54,55]
	OX26	Transferrin receptor (TfR)	Brain capillary endothelial cell	[56,57]
	J591	Prostate-specific membrane antigen (PSMA)	Prostate cancer	[58,59]
	Rituximab	CD20	Lymphoma	[66,67]
Ab fragment	Single chain variable fragments (scFV)	ED-B fibronectin c-Met	Tumor tissue Liver cancer	[68,69]
	Antigen-binding fragments (Fab)	human beta1 integrin	Non-small cell lung carcinoma	[70]
Aptamer	A10	PSMA	Prostate cancer	[60,61]
	AS1411	Nucleolin	Breast cancer	[71]
	MUC1	Membrane mucin	Adenocarcinoma Breast cancer	[72]
	anti EGFR	EGFR	Lung cancer	[73]
	anti CD30	CD30	Lymphoma	[74]
	sgc8	Protein tyrosine kinase 7 (PTK7)	Acute leukemia	[62,63]
Ligand	Transferrin	Transferrin receptor (TfR)	Lung cancer	[75]
	Folate	Folate receptor	Ovarian cancer	[76]
Peptide	Cyclic RGD	Integrin $\alpha_v\beta_3$	Kaposi's sarcoma	[77,78]
	Angiopep-2	lipoprotein receptor related protein (LRP)	BBB, glioma	[79]

3.3. Stimuli

Recently, stimuli-responsive systems have been intensively developed in targeted drug delivery systems. Due to the additional recognizable biomaterials, the target selectivity has been significantly improved and it leads to effective therapeutic results. There are wide range of exogenous or endogenous stimuli options (Table I -4). For externally introducing stimuli, drug loaded nanocarriers can be conjugated to thermosensitive [80-82], magnetic sensitive [83-85], ultrasound sensitive [86-88], light sensitive [89-91], or electric field sensitive [92,93] components for exogenous stimuli induced pathological lesion treatment. For intrinsic stimuli, pH change [94,95], redox condition [96-98], or enzyme activity [99,100] can be potential candidates. The stimuli-controllable drug delivery systems demonstrate huge advance in smart active drug delivery and it is promising strategy for clinical use when overcoming penetration depth of the applied stimulus.

Table I -4. Stimuli-controllable active drug delivery

	Stimuli	Mechanism	System	Reference
Exo- genous	Temperature	Inflammation-induced hyperthermia	Thermoresponsive polymer (pNIPAM) Thermoresponsive liposome	[80-82]
	Magnetic field	Magnet-induced drug accumulation	Magnetic core-shell nanoparticle Metallic nanocapsule	[83-85]
	Ultrasound	Local hyperthermia or microconvection-induced cell membrane destruction	Cavitation phenomena Radiation force	[86-88]
	Light	Photo-induced structural change	Photosensitive amphiphilic conjugate	[89-91]
	Electric field	Electrochemical reduction-oxidation	Conductive polymer conjugate Multiwalled carbon nanotube	[92,93]
Endo- genous	pH	Pathological area or inflammation site specific cleavage	pH-responsive complex	[94,95]
	Redox	Pathological cells specific high glutathione concentration	Reducible cationic polymer Disulfide linker	[96-98]
	Enzyme	Pathological area specific high enzyme concentration	Enzyme cleavable peptide/linker functionalization	[99,100]
	Self-regulated	Responding to concentration changes of specific analytes	Physiological condition based drug release	[101,102]

4. Scope of the studies

Tumor microenvironment (TME) has been emerged as an extraordinary target lesion in active drug delivery systems with suppressing the possibility of tumor reoccurrence. Dual targeting against tumor tissues and its neighbor environment could reduce the unexpected damages of anticancer drugs at normal tissue and improve cancer cell-specific cellular uptake. With the photoresponsive agent delivery and light irradiation, tumor could be completely treated. For TME targeting, cancer cell-overexpressing surface receptors and released enzyme around tumor sites were selected. For photoresponsive therapy, reduced graphene oxide (rGO) nanosheets and methylene blue (MB) were suggested as photothermal and photodynamic agents, respectively.

In chapter II, MB intercalated DNA nanostructures were prepared for protein tyrosine kinase 7 (PTK7) receptor-expressing acute lymphoblast leukemia cell-specific photodynamic therapy. The successive guanine sequences were self-assembled into stem-like nano-sized structure and MB can be loaded within the structure. The nanostructure could bind to PTK7 receptor through aptamer recognition. The intracellularly delivered MB could exert photodynamic effect following generating reactive oxygen species (ROS).

In chapter III, chlorine e6 (Ce6)-conjugated cyclic peptides loaded rGO

nanosheets were developed for sequential activation and photothermal therapy (PTT). The peptide linked Ce6 were loaded onto rGO nanosheets via pi-pi interactions. At cathepsin L-rich environment, the designed part of the sequence was cleaved and the targetable peptide was exposed out. Following peptide to UPAR binding, cancer cell surface receptor, the rGO nanosheets were accumulated in cytoplasm. Upon 808 nm near infrared laser irradiation, the rGO nanosheets generate heat over 50 °C at targeted site. Moreover, tumor was completely abolished by NIR irradiation following systemic administration in the target cancer cell xenografted mice.

In chapter IV, rGO nanosheets decorated with junction disrupting peptide were investigated as penetration-improving combination. The junction destroying peptide was protected by tumor releasing enzyme cleavable peptide. Once the peptide loaded rGO nanosheets close to tumor site, the protecting peptide was chopped out and the functional peptide which can disrupt the regularity of intercellular junctions were liberated. Then the enlarged space between cancer cells were eligible enough for nanoparticle to go deep. Thus, the NIR irradiation stimuli the rGO nanosheets distributed all around and the center of the tumors to generate heat. Both spheroid models and tumor bearing mice model, specific delivery and effective tumor treatment were observed.

5. References

- [1] Bonnans C, Chou J, Werb Z. Remodelling the extracellular matrix in development and disease. *Nat Rev Mol Cell Biol* 2014;15(12):786–801.
- [2] Shen Y, Shen R, Ge L, Zhu Q, Li F. Fibrillar type I collagen matrices enhance metastasis/invasion of ovarian epithelial cancer via beta1 integrin and PTEN signals. *Int J Gynecol Cancer*. 2012;22(8):1316–1324.
- [3] Raglow Z, Thomas SM. Tumor matrix protein collagen XI α 1 in cancer. *Cancer Lett*. 2015;357(2):448–453.
- [4] Kenny HA, Chiang CY, White EA, Schryver EM, Habis M, Romero IL. Mesothelial cells promote early ovarian cancer metastasis through fibronectin secretion. *J Clin Invest*. 2014;124(10):4614–4628.
- [5] Kramer M, Pierredon S, Ribaux P, Tille JC, Petignat P, Cohen M. Secretome identifies tenascin-X as a potent marker of ovarian cancer. *Biomed Res Int* 2015; 2015:9.
- [6] Ween MP, Oehler MK, Ricciardelli C. Role of versican, hyaluronan and CD44 in ovarian cancer metastasis. *Int J Mol Sci* 2011;12(2):1009–1029.
- [7] Zigrino P, Löffek S, Mauch C. Tumor-stroma interactions: their role in the control of tumor cell invasion. *Biochimie*. 2005;87(3–4):321–328.

- [8] Gialeli C., Theocharis A.D., Karamanos N.K. Roles of matrix metalloproteinases in cancer progression and their pharmacological targeting. *FEBS J.* 2011;278:16-27.
- [9] Ji F, Wang Y, Qiu L, Li S, Zhu J, Liang Z, et al. Hypoxia inducible factor 1 α -mediated LOX expression correlates with migration and invasion in epithelial ovarian cancer. *Int J Oncol* 2013;42(5):1578–1588.
- [10] Weiss I, Trope CG, Reich R, Davidson B. Hyaluronan synthase and hyaluronidase expression in serous ovarian carcinoma is related to anatomic site and chemotherapy exposure. *Int J Mol Sci* 2012;13(10):12925–12938.
- [11] Tsuyada A., Chow A., Wu J., Somlo G., Chu P., Loera S., Luu T., Li A.X., Wu X., Ye W., Chen S., Zhou W., Yu Y., Wang Y., Ren X., Li H., Scherle P., Kuroki Y., Wang S.E. CCL2 mediates cross-talk between cancer cells and stromal fibroblasts that regulates breast cancer stem cells. *Cancer Res.* 2012;72:2768-2779.
- [12] Wang Q., Tang Y., Yu H., Yin Q., Li M., Shi L., Zhang W., Li D., Li L. CCL18 from tumor-cells promotes epithelial ovarian cancer metastasis via mTOR signaling pathway. *Mol. Carcinog.* 2016;55:1688-1699.

- [13] Gupta P., Sharma P.K., Mir H., Singh R., Singh N., Kloecker G.H., Lillard Jr. J.W., Singh S. CCR9/CCL25 expression in non-small cell lung cancer correlates with aggressive disease and mediates key steps of metastasis. *Oncotarget*. 2014;5:10170-10179.
- [14] Chen L., Fan J., Chen H., Meng Z., Chen Z., Wang P., Liu L. The IL-8/CXCR1 axis is associated with cancer stem cell-like properties and correlates with clinical prognosis in human pancreatic cancer cases. *Sci. Rep.* 2014;4:5911.
- [15] Jung M., Rho J., Kim Y., Jung J.E., Jin Y..B., Ko Y., Lee J., Lee S., Lee J.C., Park M. Upregulation of CXCR4 is functionally crucial for maintenance of stemness in drug-resistant non-small cell lung cancer cells. *Oncogene*. 2013;32:209-221.
- [16] Pelicano H., Lu W., Zhou Y., Zhang W., Chen Z., Hu Y., Huang P. Mitochondrial dysfunction and reactive oxygen species imbalance promote breast cancer cell motility through a CXCL14-mediated mechanism. *Cancer Res.* 2009;69:2375-2383.
- [17] Lee W., Wang C., Lin T., Hsiao C, Luo C. CXCL17, an orphan chemokine, acts as a novel angiogenic and anti-inflammatory factor. *Am. J. Physiol. Endocrinol. Metab.* 2013;304:E32-E40.
- [18] Sukkurwala, A.Q., Martins I., Wang Y., Schlemmer F., Ruckstuhl C.,

Durchschlag M., Michaud M., Senovilla L., Sistigu A., Ma Y., Vacchelli E., Sulpice E., Gidrol X., Zitvogel L., Madeo F., Galluzzi L., Jepp O., Kroemer G. Immunogenic calreticulin exposure occurs through a phylogenetically conserved stress pathway involving the chemokine CXCL8. *Cell Death Differ.* 2014;21: 59-68.

[19] Tessema M., Klinge D.M., Yingling C.M., Do K., Neste L.V., Belinsky S.A. Re-expression of CXCL14, a common target for epigenetic silencing in lung cancer, induces tumor necrosis. *Oncogene.* 2010;29:5159-5170.

[20] Robinson S.C., Scott K.A., Balkwill F.R. Chemokine stimulation of monocyte matrix metalloproteinase-9 requires endogenous TNF- α . *Eur. J. Immunol.* 2002;32:404-412.

[21] Long H., Xiang T., Qi W., Huang J., Chen J., He L., Liang Z., Guo B., Li Y., Xie R., Zhu B. CD133+ ovarian cancer stem-like cells promote non-stem cancer cell metastasis via CCL5 induced epithelial-mesenchymal transition. *Oncotarget.* 2015;6:5846-5859.

[22] Romagnani P., Annunziato F., Laura L., Lazzeri E., Beltrame C., Francalanci M., Uguccioni M., Galli G., Cosmi L., Maurenzig L., Baggiolini M., Maggi E., Romagnani S., Serio M. Cell cycle-dependent expression of CXC chemokine receptor 3 by endothelial cells mediates angiostatic activity. *J. Clin. Invest.* 2001;107:53-63.

- [23] Tong RT, Boucher Y, Kozin SV, Winkler F, Hicklin DJ, Jain RK. Vascular normalization by vascular endothelial growth factor receptor 2 blockade induces a pressure gradient across the vasculature and improves drug penetration in tumors . *Cancer Res* 2004; 64: 3731-3736.
- [24] Horsman MR, Siemann DW. Pathophysiologic effects of vasculartargeting agents and the implications for combination with conventional therapies. *Cancer Res.* 2006; 24: 11520-11539.
- [25] Jain R.K. Normalizing tumor vasculature with anti-angiogenic therapy: a new paradigm for combination therapy. *Nat Med.* 2001;7:987-989.
- [26] Jain R.K. Normalization of tumor vasculature: an emerging concept in antiangiogenic therapy. *Science.* 2005;307:58-62.
- [27] Segers J., Fazio V.D., Ansiaux R., Martinive P., Feron O., Wallemacq P. Potentiation of cyclophosphamide chemotherapy using the antiangiogenic drug thalidomide: importance of optimal scheduling to exploit the “normalization” window of the tumor vasculature. *Cancer Lett.* 2006;244:129-135.
- [28] Horsman M.R., Siemann D.W. Pathophysiologic effects of vascular targeting agents and the implications for combination with conventional therapies. *Cancer Res.* 2006;24:11520-11539.

- [29] Curnis F., Sacchi A., Corti A. Improving chemotherapeutic drug penetration in tumors by vascular targeting and barrier alteration. *J Clin Invest.* 2002;110:475-482.
- [30] Emerich D.F., Dean R.L., Snodgrass P., Lafreniere D., Agostino M., Wiens T. Bradykinin modulation of tumor vasculature: II. activation of nitric oxide and phospholipase A2/prostaglandin signaling pathways synergistically modifies vascular physiology and morphology to enhance delivery of chemotherapeutic agents to tumors. *J Pharmacol Exp Ther.* 2001;296:632-641.
- [31] Batchelor T.T., Sorensen A.G., di Tomaso E., Zhang W.T., Duda D.G., Cohen K.S. AZD2171, a pan-VEGF receptor tyrosine kinase inhibitor, normalizes tumor vasculature and alleviates edema in glioblastoma patients. *Cancer Cell.* 2007;11:83-95.
- [32] Pietras K., Rubin K., Sjoblom T., Buchdunger E., Sjoquist M., Heldin C.H. Inhibition of PDGF receptor signaling in tumor stroma enhances antitumor effect of chemotherapy. *Cancer Res.* 2002;62:5476-5484.
- [33] Pietras K., Stumm M., Hubert M., Buchdunger E., Rubin K., Heldin C.H. STI571 enhances the therapeutic index of epothilone B by a tumor-selective increase of drug uptake. *Clin Cancer Res.* 2003;9:3779-3787.

- [34] Batchelor TT., Sorensen AG, di Tomaso E, Zhang WT, Duda DG, Cohen KS. AZD2171, a pan-VEGF receptor tyrosine kinase inhibitor, normalizes tumor vasculature and alleviates edema in glioblastoma patients. *Cancer Cell*. 2007; 11: 83-95.
- [35] Eikenes L, Bruland OS, Brekken C, Davies Cde L. Collagenase increases the transcapillary pressure gradient and improves the uptake and distribution of monoclonal antibodies in human osteosarcoma xenografts. *Cancer Res*. 200 ; 64: 4768-4773.
- [36] Brown E, McKee T, diTomaso E, Pluen A, Seed B, Boucher Y. Dynamic imaging of collagen and its modulation in tumors in vivo using second-harmonic generation. *Nat Med*. 2003; 9: 796-800.
- [37] Eikenes L., Bruland O.S., Brekken C., Davies Cde L. Collagenase increases the transcapillary pressure gradient and improves the uptake and distribution of monoclonal antibodies in human osteosarcoma xenografts. *Cancer Res*. 2004;64:4768-4773.
- [38] Brown E., McKee T., diTomaso E., Pluen A., Seed B., Boucher Y. Dynamic imaging of collagen and its modulation in tumors in vivo using second-harmonic generation. *Nat Med*. 2003;9:796-800.
- [39] Maeda H., Wu J., Sawa T., Matsumura Y., Hori K. Tumor vascular permeability and the EPR effect in macromolecular therapeutics: a

review, *J. Control Release* 2000;65:271-284.

- [40] Sharna P., Brown S., Walter G., Santra S., Moudgil B. Nanoparticles for bioimaging. *Adv. Colloid Interfac.* 2006;123:471-485.
- [41] Ferrari M., Cancer nanotechnology: opportunities and challenges. *Nat. Rev. Cancer* 2005;5:161-171.
- [42] Pan Q., Lv Y., Williams G.R., Tao L., Yang H., Li H., Zhu L. Lactobionic acid and carboxymethyl chitosan functionalized graphene oxide nanocomposites as targeted anticancer drug delivery systems. *Carbohydr Polym.* 2016;151:812-820.
- [43] Yang H., Bremner D.H., Tao L. Li H., Hu J., Zhu L. Carboxymethyl chitosan-mediated synthesis of hyaluronic acid-targeted graphene oxide for cancer drug delivery. *Carbohydr Polym.* 2016;135:72-78.
- [44] Li J., Fan C.m Pei H., Shi J., Huang Q. Smart drug delivery nanocarriers with self-assembled DNA nanostructures. *Adv Mater.* 2013;25:4386-4396.
- [45] Zhang Q., Jiang Q., Li N., Dai L., Liu Q., Song L., Wang J., Li Y., Tian J., Ding B., Du Y. DNA origami as an in vivo drug delivery vehicle for cancer therapy. *ACS Nano.* 2014;8(7):6633-6643.

- [46] Bovis M.J., Woodhams J.H., Loizidou M., Scheglmann D., Bown S.G., MacRobert A.J. Improved in vivo delivery of m-THPC via pegylated liposomes for use in photodynamic therapy. *J. Control Release.* 2012;157:196-205.
- [47] Kopelman R., Koo Y.E.L., Philbert M., Moffat B.A., Reddy G.R., McConville P., Hall D.E., Chenevert T.L., Bhojani M.S., Buck S.M., Rehemtulla A., Ross B.D. Multifunctional nanoparticle platforms for in vivo MRI enhancement and photodynamic therapy of a rat brain cancer. *J. Magn. Magn. Mater.* 2005;293:404-410.
- [48] Kataoka K., Harada A., Nagasaki Y. Block copolymer micelles for drug delivery: design, characterization and biological significance. *Adv. Drug Deliv. Rev.* 2001;47:113-131.
- [49] Bechet D., Couleaud P., Frochot C., Viriot M-L., Guillemin F., Barberi-Heyob M. Nanoparticles as vehicles for delivery of photodynamic therapy agents. *Trends Biotechnol.* 2008;26:612-621.
- [50] Liechty W.B., Peppas N.A., Expert opinion: responsive polymer nanoparticles in cancer therapy. *Eur. J. Pharm. Biopharm.* 2012;80:241-246.
- [51] Haley B., Frenkel E. Nanoparticles for drug delivery in cancer treatment. *Urol. Oncol.* 2008;26:57-64.

- [52] Ruan J., Song H., Qian Q., Li C., Wang K., Bao C. HER2 monoclonal antibody conjugated RNase-A-associated CdTe quantum dots for targeted imaging and therapy of gastric cancer. *Biomaterials*. 2012;33(29):7093-7102.
- [53] Wartlick H., Michaelis K., Balthasar S., Strebhardt K., Kreuter J., Langer K. Highly specific HER2-mediated cellular uptake of antibody-modified nanoparticles in tumour cells. *J Drug Target*. 2004;12(7):461-471.
- [54] Harding J., Burtneß B. Cetuximab: an epidermal growth factor receptor chimeric human-murine monoclonal antibody. *Drugs Today*. 2005;41(2):107-127.
- [55] Cherukuri P., Curley S.A. Use of nanoparticles for targeted, noninvasive thermal destruction of malignant cells. *Methods Mol Biol*. 2010;624:359-373.
- [56] Daniels T.R., Bernabeu E., Rodriguez J.A., Patel S., Kozman M., Chiappetta D.A. The transferrin receptor and the targeted delivery of therapeutic agents against cancer. *Biochim Biophys Acta*. 2012;1820(3):291-317.
- [57] Gosk S., Vermehren C., Storm G., Moos T. Targeting antitransferrin receptor antibody (OX26) and OX26-conjugated liposomes to brain

capillary endothelial cells using in situ perfusion. *J Cereb Blood Flow Metab.* 2004; 24(11):1193-1204.

- [58] Hrkach J., Von H.D., Mukkaram A.M., Andrianova E., Auer J., Campbell T. Preclinical development and clinical translation of a PSMA-targeted docetaxel nanoparticle with a differentiated pharmacological profile. *Sci Transl Med* 2012;4(128):128-139.
- [59] Taylor R.M., Huber D.L., Monson T.C., Ali A.M., Bisoffi M., Sillerud L.O. Multifunctional iron platinum stealth immunomicelles: targeted detection of human prostate cancer cells using both fluorescence and magnetic resonance imaging. *J Nanopart Res.* 2011;13(10):4717-4729.
- [60] Dhar S., Gu F.X., Langer R., Farokhzad O.C., Lippard S.J. Targeted delivery of cisplatin to prostate cancer cells by aptamer functionalized Pt(IV) prodrug-PLGA-PEG nanoparticles. *Proc Natl Acad Sci U S A* 2008;105(45):17356-17361.
- [61] Kolishetti N., Dhar S., Valencia P.M., Lin L.Q., Karnik R., Lippard S.J. Engineering of self-assembled nanoparticle platform for precisely controlled combination drug therapy. *Proc Natl Acad Sci U S A.* 2010; 107(42):17939-17944.
- [62] Estevez M.C., Huang Y.F., Kang H., O'Donoghue M.B., Bamrungsap S., Yan J. Nanoparticle-aptamer conjugates for cancer cell targeting and

detection. *Methods Mol Biol.* 2010;624:235-248.

- [63] Huang Y.F., Chang H.T., Tan W. Cancer cell targeting using multiple aptamers conjugated on nanorods. *Anal Chem* 2008;80(3):567-572.
- [64] Gu F.X., Karnik R., Wang A.Z., Alexis F., Levy-Nissenbaum E., Hong S., Langer R.S., Farokhzad O.C. Targeted nanoparticles for cancer therapy. *Nano Today.* 2007;2:14-21.
- [65] Phillips M.A., Gran M.L., Peppas N.A. Targeted nanodelivery of drugs and diagnostics. *Nano Today.* 2010;5:143-159.
- [66] Bisker G., Yeheskely-Hayon D., Minai L., Yelin D. Controlled release of Rituximab from gold nanoparticles for phototherapy of malignant cells. *J Control Release.* 2012;162(2):303-309.
- [67] Nobs L., Buchegger F., Gurny R., Allemann E. Biodegradable nanoparticles for direct or two-step tumor immunotargeting. *Bioconjug Chem.* 2006;17(1):139-145.
- [68] Marty C., Schwendener R.A. Cytotoxic tumor targeting with scFv antibody-modified liposomes. *Methods Mol Med.* 2005;109:389-402.
- [69] Lu R.M., Chang Y.L., Chen M.S., Wu H.C. Single chain anti-c-Met antibody conjugated nanoparticles for in vivo tumor-targeted imaging

and drug delivery. *Biomaterials*. 2011;32(12):3265-3274.

- [70] Sugano M., Egilmez N.K., Yokota S.J., Chen F.A., Harding J., Huang S.K. Antibody targeting of doxorubicin-loaded liposomes suppresses the growth and metastatic spread of established human lung tumor xenografts in severe combined immunodeficient mice. *Cancer Res*. 2000;60(24):6942-6949.
- [71] Hwang do W., Ko H.Y., Lee J.H., Kang H., Ryu S.H., Song I.C. A nucleolin-targeted multimodal nanoparticle imaging probe for tracking cancer cells using an aptamer. *J Nucl Med*. 2010;51(1):98-105.
- [72] Yu C., Hu Y., Duan J., Yuan W., Wang C., Xu H. Novel aptamer-nanoparticle bioconjugates enhances delivery of anticancer drug to MUC1-positive cancer cells in vitro. *PLoS ONE*. 2011;6(9):e24077.
- [73] Li N., Larson T., Nguyen H.H., Sokolov K.V., Ellington A.D. Directed evolution of gold nanoparticle delivery to cells. *Chem Commun*. 2010;46(3):392-394.
- [74] Zhao N., Bagaria H.G., Wong M.S., Zu Y. A nanocomplex that is both tumor cell-selective and cancer gene-specific for anaplastic large cell lymphoma. *J Nanobiotechnol*. 2011;9:2.
- [75] Anabousi S., Bakowsky U., Schneider M., Huwer H., Lehr C.M.,

- Ehrhardt C. In vitro assessment of transferrin-conjugated liposomes as drug delivery systems for inhalation therapy of lung cancer. *Eur J Pharm Sci.* 2006;29(5):367-374.
- [76] Corbin I.R., Ng K.K., Ding L., Jurisicova A., Zheng G. Near infrared fluorescent imaging of metastatic ovarian cancer using folate receptor-targeted high-density lipoprotein nanocarriers. *Nanomedicine.* 2012;8(6):875-890.
- [77] Zhou A., Wei Y., Wu B., Chen Q., Xing D. Pyropheophorbide A and c(RGDyk) comodified chitosan-wrapped upconversion nanoparticle for targeted near infrared photodynamic therapy. *Mol. Pharm.* 2012;9:1580-1589.
- [78] Nasongkla N., Shuai X., Ai H., Weinberg B.D., Pink J., Boothman D.A., Gao J. CRGD-functionalized polymer micelles for targeted doxorubicin delivery. *Angew. Chem., Int. Ed.* 2004;116:6483-6487.
- [79] Xin H., Jiang X., Gu J., Sha X., Chen L., Law K., Chen Y., Wang X., Jiang Y., Fang X. Angiopep-conjugated poly(ethylene glycol).co-poly(ϵ -caprolactone) nanoparticles as dual-targeting drug delivery system for brain glioma. *Biomaterials* 2011;32:4293-4305.
- [80] Zhang J., Chen H., Xu L., Gu Y. The targeted behavior of thermally responsive nanohydrogel evaluated by NIR system in mouse model. *J.*

Control. Release. 2008;131:34-40.

- [81] Chen K., Liang H., Chen H., Wang Y., Cheng P., Liu H., Xia Y., Sung H. A thermoresponsive bubble-generating liposomal system for triggering localized extracellular drug delivery. ACS Nano. 2013;7:438-446.
- [82] Smith B., Lyakhov I., Loomis K., Needle D., Baxa U., Yavlovich A., Capala J., Blumenthal R., Puri A. Hyperthermia-triggered intracellular delivery of anticancer agent to HER2+ cells by HER2-specific affibody (ZHER2-GS-Cys)-conjugated thermosensitive liposomes (HER2+ affisomes). J. Control. Release. 2011;153:187-194.
- [83] Zhang L., Wang T., Yang L., Liu C., Wang C., Liu H., Wang A., Su Z. General route to multifunctional uniform yolk/mesoporous silica shell nanocapsules: a platform for simultaneous cancer-targeted imaging and magnetically guided drug delivery. Chem. Eur. J. 2012;18:12512-12521.
- [84] Plassat V., Wilhelm C., Marsaud V., Menager C., Gazeau F., Renoir J., Lesieur S. Anti-estrogen-loaded superparamagnetic liposomes for intracellular magnetic targeting and treatment of breast cancer tumors. Adv. Funct. Mater. 2011;21:83-92.
- [85] Zhang F., Braun G.B., Pallaoro A., Zhang Y., Shi Y., Cui D., Moskovits M., Zhao D., Stucky G.D. Mesoporous multifunctional

upconversion luminescent and magnetic “nanorattle” materials for targeted chemotherapy. *Nano Lett.* 2012;12:61-67.

[86] Schroeder A., Honen R., Turjeman K., Gabizon A., Kost J., Barenholz Y. Ultrasound triggered release of cisplatin from liposomes in murine tumors. *J. Control. Release.* 2009;137:63-68.

[87] Rapoport N.Y., Kennedy A.M., Shea J.E., Scaife C.L., Nam K.H. Controlled and targeted tumor chemotherapy by ultrasound-activated nanoemulsions/microbubbles. *J. Control. Release.* 2009;138:268-276.

[88] Wang C., Kang S., Lee Y., Luo Y., Huang Y., Yeh C. Aptamer-conjugated and drug-loaded acoustic droplets for ultrasound theranosis. *Biomaterials.* 2012;33:1939-1947.

[89] He D., He X., Wang K., Cao J., Zhao Y. A light-responsive reversible molecule-gated system using thymine-modified mesoporous silica nanoparticles. *Langmuir.* 2012;28:4003-4008.

[90] Azagarsamy M.A., Alge D.L., Radhakrishnan S.J., Tibbitt M.W., Anseth K.S. Photocontrolled nanoparticles for on-demand release of proteins. *Biomacromolecules.* 2012;13:2219-2224.

[91] Tong R., Hemmati H.D., Langer R., Kohane D.S. Photoswitchable nanoparticles for triggered tissue penetration and drug delivery. *J. Am.*

Chem. Soc. 2012;134:8848-8855.

- [92] Ge J., Neofytou E., Cahill T.J., Beygui R.E., Zare R.N. Drug release from electric-field-responsive nanoparticles. *ACS Nano*. 2011;6:227-233.
- [93] Im J.S., Bai B.C., Lee Y. The effect of carbon nanotubes on drug delivery in an electro-sensitive transdermal drug delivery system. *Biomaterials*. 2010;31:1414-1419.
- [94] Deng Z., Zhen Z., Hu X., Wu S., Xu Z., Chu P.K. Hollow chitosan-silica nanospheres as pH-sensitive targeted delivery carriers in breast cancer therapy. *Biomaterials*. 2011;32:4976-4986.
- [95] Gao G.H., Park M.J., Im G.H., Kim J., Kim H.N., Lee J.W., Jeon P., Bang O.Y., Lee J.H., Lee D.S. The use of pH-sensitive positively charged polymeric micelles for protein delivery. *Biomaterials*. 2012;33:9157-9164.
- [96] Li J., Huo M., Wang J., Zhou J., Mohammad J.M., Zhang Y., Zhu Q., Waddad A.Y., Zhang Q. Redox-sensitive micelles self-assembled from amphiphilic hyaluronic acid-deoxycholic acid conjugates for targeted intracellular delivery of paclitaxel. *Biomaterials*. 2012;33:2310-2320.
- [97] Li Y., Xiao K., Luo J., Xiao W., Lee J.S., Gonik A.M., Kato J., Dong T.A., Lam K.S. Well-defined, reversible disulfide cross-linked micelles

for on demand paclitaxel delivery. *Biomaterials*. 2011;32:6633-6645.

- [98] Kim H., Kim S., Park C., Lee H., Park H.J., Kim C. Glutathione-induced intracellular release of guests from mesoporous silica nanocontainers with cyclodextrin gatekeepers. *Adv. Mater.* 2010;22:4280-4283.
- [99] Zhu L., Kate P., Torchilin V.P. Matrix metalloprotease 2-responsive multifunctional liposomal nanocarrier for enhanced tumor targeting. *ACS Nano*. 2012;6:3491-3498.
- [100] Harris T.J., Maltzahn G.V., Lord M.E., Park J., Agrawal A., Min D., Sailor M.J., Bhatia S.N. Protease-triggered unveiling of bioactive nanoparticles. *Small*. 2008;4:1307-1312.
- [101] Xiong M., Bao Y., Yang X., Wang Y., Sun B., Wang J. Lipase-sensitive polymeric triple-layered nanogel for “on-demand” drug delivery. *J. Am. Chem. Soc.* 2012;134:4355-4362.
- [102] Yao Y., Zhao L., Yang J., Yang J. Glucose-responsive vehicles containing phenylborate ester for controlled insulin release at neutral pH. *Biomacromolecules*. 2012;13:1837-1844.

Chapter II

Stemmed DNA nanostructure for selective delivery of therapeutics

1. Introduction

DNA has recently emerged as a biocompatible biomaterial whose biodegradable and nonimmunogenic features make it attractive for biomedical applications. DNA strands have been enzymatically amplified to construct three-dimensional nanostructures [1,2], and complicated DNA sequences have been used to form nanostructures of various shapes [3,4]. Despite this progress, however, there is need to further develop a DNA-based nanostructure that can confer targeted and efficient drug delivery to target cells.

Oligomers of guanine have been reported to form defined three dimensional structures [5,6]. Quadruplex structures of oligoguanine have been reported to show thermostability and nuclease resistance [7,8]. However, although oligoguanine have shown the potential to form ordered characteristic three-dimensional structures, the previous studies have focused on the elucidation of nanostructure formation, and basic biophysical mechanistic studies. Few studies have examined their potential application for the cell-specific delivery of therapeutic substances by introduction of specific target-recognition moieties.

In this study, we hypothesized that DNA aptamer-modified oligoguanine quadruplex nanostructures could be used to specifically deliver therapeutic molecules to target cells. To test this hypothesis, we used a photosensitizer as an example of a therapeutic molecule, and applied a protein tyrosine kinase (PTK)7-specific DNA aptamer for delivery to PTK7-overexpressing cancer cells. We show that aptamer-tethered oligoguanine nucleotides self-assembled to form Y shape DNA structure, DNA nanostructures have strong potential for cell-specific drug delivery and improved therapeutic effects.

2. Materials and methods

2.1. Construction of DNA nanostructures

DNAs with a consecutive 15-mer guanine (G15) sequence were constructed through self-assembly [7]. Linear single-stranded DNAs (5 μ M ssDNAs; Macrogen Inc., Daejeon, Republic of Korea) corresponding to the aptamer or a scrambled sequence-linked G15 were annealed in a buffer (90 mM Tris-Borate, 5 mM MgCl₂, pH 8.3) by heating at 95°C for 5 min followed by gradual cooling to room temperature in a 1-L beaker of water over 3 h. Aptamer-modified 15-mer cytosine was prepared as another control. The resulting DNA products were stored at 4°C until use. The oligodeoxynucleotide sequences of the PTK7 aptamer (Apt), PTK7 aptamer-linked C15 (AptC15), scrambled aptamer-linked G15 (ScrG15), and PTK7 aptamer-linked G15 (AptG15) are presented in Fig. 1A. The concentration of DNA in each sample was measured using a NanoDrop spectrophotometer (Thermo Scientific, Waltham, MA, USA).

2.2. Gel migration analysis

To assess the self-aggregations of Apt, AptC15, ScrG15, and AptG15, we analyzed the product sizes by native polyacrylamide gel electrophoresis. The hybridized DNA products were loaded onto a 15% sodium dodecyl sulfate-polyacrylamide gel. After electrophoresis at 100 V, the DNA bands were visualized by silver staining. Briefly, the gel was treated with 7.5 % acetic acid (CH_3COOH ; Samchun Pure Chemical Co., Ltd., Pyungtack, Republic of Korea) for 10 min to immobilize the DNA. After 2 min-wash with deionized water three-times, the gel was treated with 15% formaldehyde (Samchun Pure Chemical Co., Ltd.) for 10 min. Then the gel was treated with 0.1% silver nitrate (AgNO_3 ; Sigma-Aldrich, St.Louis, MO, USA) for 20 min. The silver impregnated DNA was visualized after treating cold 3% sodium carbonate (Na_2CO_3 ; Sigma-Aldrich) and 0.4 % sodium thiosulfate ($\text{Na}_2\text{S}_2\text{O}_3$; Samchun Pure Chemical Co. Ltd.) and the development was stopped with cold 7.5% acetic acid treatment. The gel was washed with deionized water and photographed using a digital camera (Canon PC 1089, Canon Inc., Tokyo, Japan).

2.3. Characterization of DNA nanostructures

The formation of DNA nanostructures was characterized by assessing

morphology, circular dichroism (CD), and Raman scattering spectroscopy. The morphology of the DNA nanostructures was investigated by transmission electron microscopy (TEM) using a JEM 1010 transmission electron microscope (JEOL, Tokyo, Japan). For TEM imaging, DNA samples (5 μ M) were incubated in 20 mM phosphate buffer, pH 8.3, containing 1 mM magnesium acetate and 11 mM chloroauric acid (HAuCl₄; Sigma-Aldrich) at room temperature for 1 h. The reducing agent, dimethylamine borane (Sigma-Aldrich), was added at a concentration of 1.1 mM. After 5 min, the excess HAuCl₄ and dimethylamine borane were removed from the DNA samples with a PD-10 desalting column (GE Healthcare, Buckinghamshire, UK).

For the analysis of CD and Raman spectra, samples were prepared to a final concentration of 20 μ M DNA. CD spectra were recorded with a Chirascan-plus CD spectrometer (Applied Photophysics Ltd., Surrey, UK) in a 0.1-cm-path-length quartz cell at a scan rate of 100 nm/min. Raman spectra were measured with a Horiba Jobin-Yvon Lab Ram Aramis spectrometer (Horiba Scientific, Boston, MA, USA). The Raman system used a HeNe diode laser with an emission wavelength of 785 nm and a power of 4 mW.

For NMR analysis, samples were prepared to a final concentration of 0.12

mM. After adding 10% deuterium oxide (D₂O, Sigma-Aldrich), 1D ¹H NMR experiments were performed on a 800 MHz spectrometer (Bruker AVANCE, Billerica, MA, USA) at 288 K.

2.4. Measurement of MB loading efficiency

Apt, AptC15, ScrG15, and AptG15 were loaded with MB (Sigma-Aldrich) at various weight ratios and incubated at room temperature for 10 min, and the unloaded free MB was removed with a PD-10 desalting column (GE Healthcare). The extent of MB loading to Apt, AptC15, ScrG15, or AptG15 was determined by the measuring the DNA-binding-based quenching of MB fluorescence. The fluorescence of MB was measured at an excitation wavelength of 630 nm and an emission wavelength of 680 nm, using a fluorescence microplate reader (Gemini XS; Molecular Devices, Sunnyvale, CA, USA).

2.5. Cell culture

Human T-cell acute lymphoblastic leukemia (CCRF-CEM) cells and human Burkitt's lymphoma (Ramos) cells (Korean Cell Line Bank, Seoul, Republic of Korea) were maintained in RPMI-1640 (Welgene, Daegu, Republic of Korea) supplemented with 10% fetal bovine serum (FBS), 100 units/mL

penicillin, and 100 µg/mL streptomycin. The cells were grown at 37°C in a humidified 5% CO₂ atmosphere.

2.6. siRNA-mediated knockdown of PTK7 in CCRF-CEM cells

siRNAs against PTK7 (siPTK7) were purchased from Bioneer (Daejeon, Republic of Korea). The sequences the utilized siRNAs were as follows: siPTK7, 5'-ACA ACC GCU UUG UGC AUA AGG AC(dTdT)-3' (sense) and 5'-GUC CUU AUG CAC AAA GCG GUU GU(dTdT)-3', (antisense). CCRF-CEM cells were seeded at a density of 1×10^5 cells/well in 6-well plates. After 24 h, the cells were transfected with siRNA using Lipofectamine 2000 (Invitrogen Corp., Carlsbad, CA, USA) according to the manufacturer's instructions. Briefly, siRNA (100 nM) was mixed with 2 µL of Lipofectamine 2000 in 100 µL of Opti-MEM (Gibco BRL, Grand Island, NY, USA). The mixtures were incubated for 20 min at room temperature and applied to the cells. The cells were then incubated for 72 h and used for further experiments.

2.7. Flow cytometry analysis of PTK7-knockdown

The silencing of PTK7 protein expression by siPTK7 transfection was

evaluated by flow cytometry [26]. CCRF-CEM cells and siPTK7-transfected CCRF-CEM cells were treated with 2 % bovine serum albumin-containing PBS for 1 h at room temperature. After PBS washing, the cells were incubated for 1 h at room temperature with a fluorescein-conjugated PTK7 antibody at a dilution of 1:100. PTK7-positive cell populations were evaluated using BD FACSCalibur equipped with Cell Quest Pro software (BD Bioscience).

2.8. In vitro cellular uptake study

Flow cytometry and confocal microscopy were used to evaluate the cellular uptake of free MB, Apt, MB-loaded ScrG15 (MB/ScrG15), and MB-loaded AptG15 (MB/AptG15). Ramos or CCRF-CEM cells with or without siPTK7 treatment were seeded to a 48-well plate at a density of 8×10^4 cells/well and incubated overnight. The next day, the cells were treated for 15 min with 5 μ M of MB in free form or incorporated in 10 μ M of AptG15 or ScrG15. The cells were washed with 2% FBS-containing phosphate-buffered saline (PBS), and analyzed using a BD FACSCalibur flow cytometer and the Cell Quest Pro software (BD Biosciences, San Jose, CA, USA). For confocal microscopy, the cells were transferred onto poly-L-lysine coated plates (BD Biosciences) and incubated for 1 h. The cells were fixed with

4% paraformaldehyde-containing PBS for 15 min and then stained with 4',6-diamidino-2-phenylindole dihydrochloride (DAPI, Sigma-Aldrich). The fluorescence intensity was measured using a confocal laser scanning microscope (LSM 5 Exciter; Carl Zeiss, Inc., Jena, Germany).

2.9. Detection of cellular reactive oxygen species (ROS)

To test the activity of MB delivered by AptG15, production of cellular ROS upon 660-nm light irradiation was measured using a cell-permeating fluorescent ROS indicator. Ramos or CCRF-CEM cells with or without siPTK7 treatment were seeded onto cover glasses at a density of 8×10^4 cells/well in 48-well plates. The next day, the cells were treated with 5 μM of MB in free form or incorporated in 10 μM of AptG15 or ScrG15. After 15 min of incubation, the cells were washed with cold PBS and irradiated for 10 min using a 660-nm light emitting diode (LED; Shenzhen Ezoneda Technology Co., Guangdong, China) with a luminous intensity of 8000 mCd. After irradiation, the cells were resuspended in 10 μM of the ROS indicator, H2DCFDA (2',7'-dichlorodihydro fluorescein diacetate; Sigma-Aldrich) for 30 min, and nuclei was stained with DAPI for 10 min. The cells were washed with fresh PBS for three times. The fluorescence intensity of the ROS indicator and DAPI was observed under fluorescence microscopy

(Leica DM IL; Leica, Wetzlar, Germany).

2.10. In vitro photodynamic efficacy study

The ROS-mediated photodynamic effects were measured by testing the viability of variously treated cell groups upon 660-nm irradiation using a light-emitting diode (LED, Mikwhang Co., Pusan, Republic of Korea) at a power density of 20 mW cm^{-2} [28, 29]. Cell viability was examined using the MTT (3-(4, 5-dimethylthiazol-2-yl)-2, 5-diphenyltetrazolium bromide; Sigma-Aldrich) assay and by fluorescent staining of live cells. Ramos or CCRF-CEM cells with or without siPTK7 treatment were seeded onto cover glasses at a density of 8×10^4 cells/well in 48-well plates. The next day, the cells were treated with $5 \mu\text{M}$ of MB in free form or incorporated in $10 \mu\text{M}$ of AptG15 or ScrG15 for 15 min. The cells were washed with cold PBS, re-suspended in fresh medium, irradiated at 660 nm for 10 min, and further incubated for 24 h. For MTT assays, $500 \mu\text{M}$ MTT solution was added to each well. After 2 h, the medium was discarded, the obtained crystals were dissolved in $200 \mu\text{L}$ dimethyl sulfoxide (Sigma-Aldrich), and absorbance was measured at 570 nm using a microplate reader (Tecan Group Ltd., Seestrasse, Mannedorf, Switzerland). For fluorescence microscopy, live cells were stained with $2 \mu\text{M}$ of calcein-AM

(Sigma-Aldrich) for 10 min, and observed under a fluorescence microscope (Leica DM IL).

2.11. Statistics

ANOVA was used for statistical evaluation of data, with the Student-Newman-Keuls test applied as a post-hoc test. All statistical analyses were carried out using the SigmaStat software (version 3.5; Systat Software, Richmond, CA, USA), and a p-value < 0.05 was considered significant.

3. Results

3.1. Schematic illustration of DNA nanostructures

The expected structures of the various DNA aggregation products are illustrated in Fig. II-1B. ScrG15 and AptG15 shared the 15G sequence, which was designed to self-assemble into stem-like structures, and were decorated with scrambled sequences and aptamer sequences, respectively. For comparison with AptG15, we also synthesized AptC15, which had 15 successive cytosine sequences, and not expected to self-assemble for comparison with AptG15.

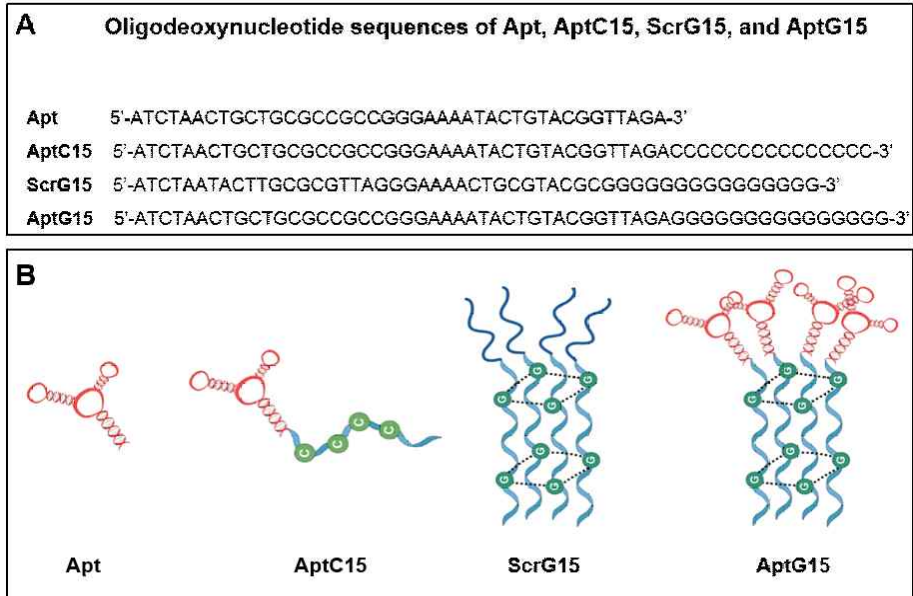


Fig. II -1. Oligodeoxynucleotide sequences and schematic structures.

Sequences (A) and schematic drawings (B) of the putative structures of Apt, AptC15, ScrG15, and AptG15 are illustrated. ScrG15 and AptG15 contain 15G sequences, which are predicted to enable the formation of stem-like structures by self-assembly.

3.2. Characterization of self-assembly nanostructures

SDS-polyacrylamide gel electrophoresis revealed that the mobility of Apt decreased in ScrG15 and AptG15, but not AptC15 (Fig. II -2A). Consistent with this gel retardation pattern, CD spectroscopy showed evidence of DNA oligodeoxyribonucleotide self-assembly in ScrG15 and AptG15, but not Apt or AptC15 (Fig. II -2B). The spectroscopic peaks of AptC15 near 280 nm were shifted to red in AptG15; the distinct peak at 262 nm for AptG15 indicates the existence of guanine-based G-quadruplexes (Fig. II -2B).

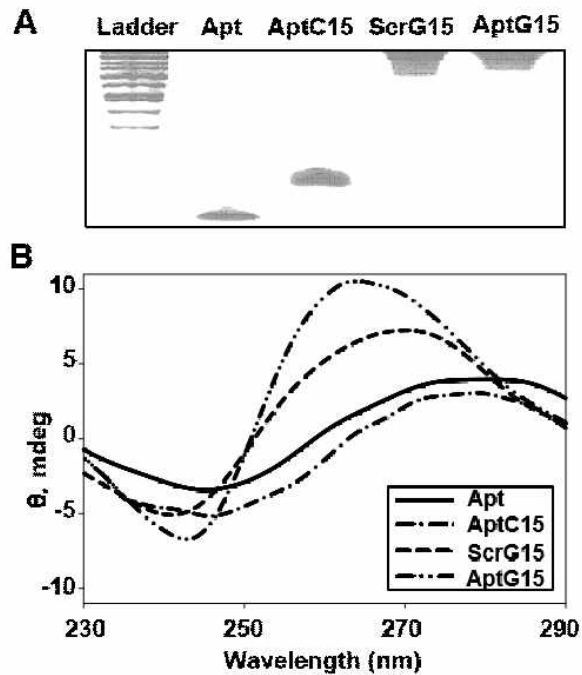


Fig. II-2. Electrophoresis and circular dichroism (CD) spectroscopy.

(A) The gel migration patterns of Apt, AptC15, ScrG15, and AptG15 were evaluated by 15% polyacrylamide gel electrophoresis. (B) Apt, AptC15, ScrG15, and AptG15 were subjected to CD spectroscopy.

3.3. Characterization of G-quadruplex in self-assembled DNA nanostructures

Transmission electron microscopic (TEM) images of gold-incorporated Apt, AptC15, ScrG15, and AptG15 showed that the 15 3'-guanine residues affected the morphology of the obtained DNA-based structures. No regular shape was observed in Apt or AptC15, whereas AptG15 and ScrG15 showed the regular Y-shape structures (Fig. II -3A, Fig. II -4). The Raman spectra also differed between AptC15 and AptG15: Hoogsteen hydrogen bonding was observed at 1480 cm^{-1} (N7 hydrogen bonding), 1578 cm^{-1} (C2-NH₂ group), and 1605 cm^{-1} (N1) in AptG15, but not in AptC15 (Fig. II -3B). The 1D ¹H NMR spectra of the stemmed DNAs indicated the quadruplex structures of Scr G15 and AptG15. No peaks were observed between 10 and 12 ppm at Apt or AptC15. However, ScrG15 or AptG15 showed specific peaks at a range of 10 to 12 ppm (Fig. II -4).

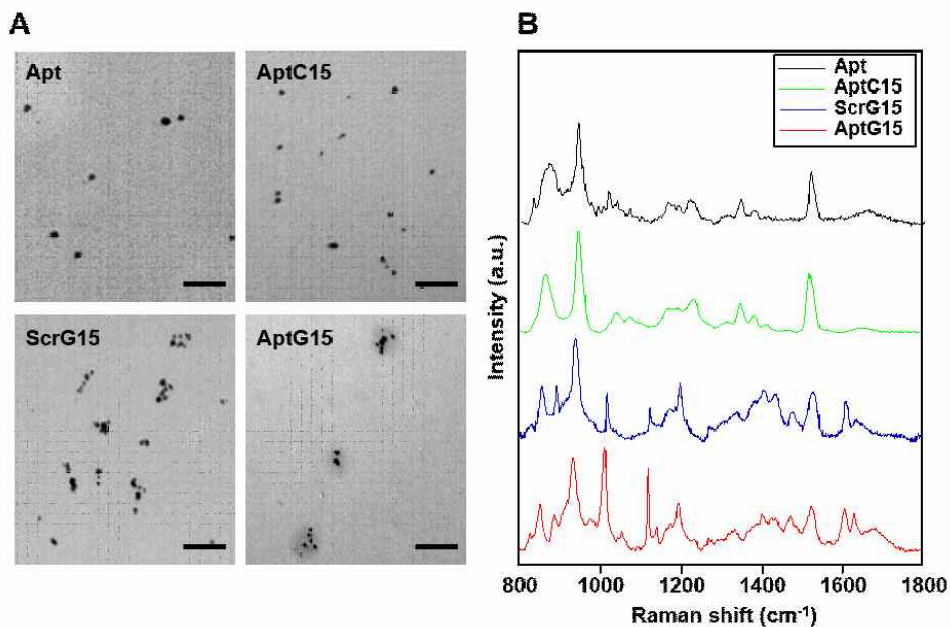


Fig. II -3. TEM imaging and Raman spectroscopy.

(A) The morphologies of gold-incorporated Apt, AptC15, ScrG15, and AptG15 were observed by TEM. Scale bar: 100 nm for all groups. (B) Raman spectra of Apt, AptC15, ScrG15, and AptG15.

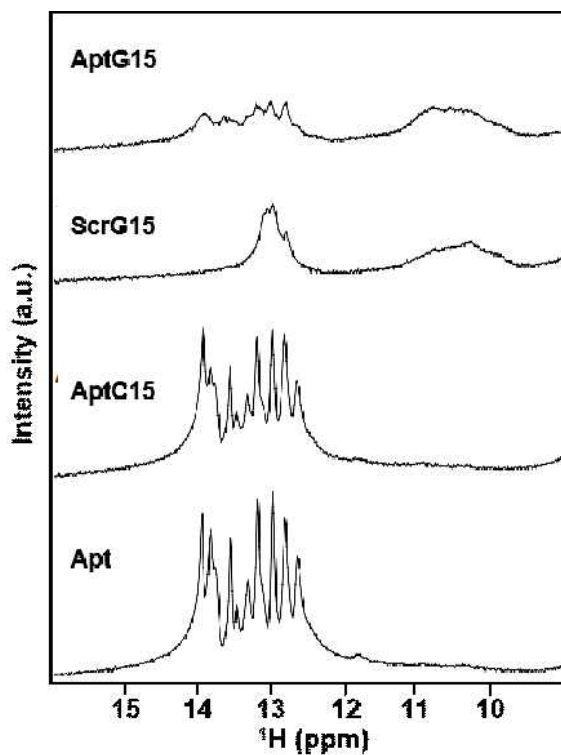


Fig. II -4. NMR spectra of stemmed DNA nanostructures.

The 1D ¹H NMR was performed to evaluate the imino regions of the DNA nanostructures. The DNAs were prepared at a final concentration of 0.12 mM and the NMR spectra were recorded at 288 K under 10 % D₂O condition.

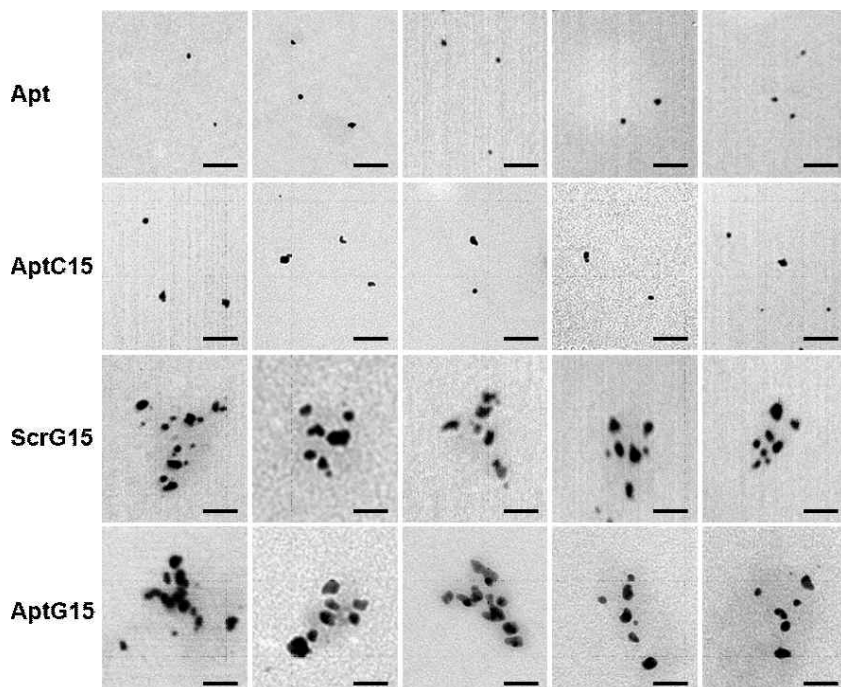


Fig. II -5. The morphologies of gold-incorporated DNA nanostructures. For transmission electron microscopy (TEM) imaging, chloroauric acid was added to DNA-based nanostructures for 1 h at room temperature. After removal of free chloroauric acid following reduction, the gold-loaded DNA nanostructures were visualized by TEM. For each condition, five pictures were presented. Scale bar: 25 nm.

3.4. Nanostructure dependence of drug loading

To support the application of the generated Y-shaped DNA nanostructure as drug carriers, we examined their ability to be loaded with methylene blue (MB), as detected by fluorescence quenching. We found that the loading efficiency of MB depended on the nanostructure of the hybridized DNA product: MB incubated with Apt or AptC15 exhibited little quenching (Fig. II -6A, B), whereas dose-dependent quenching was observed in the presence of ScrG15 or AptG15 (Fig. II -6C, D). The loading efficiencies of Apt and AptC15 were less than 7% and 6%, respectively, regardless of the DNA:MB weight ratio, while those of ScrG15 and AptG15 were similar at $84.0\% \pm 2.4\%$ and $84.6\% \pm 1.9\%$, respectively, at the optimal weight ratio of 10:1 (Fig. II -6E).

In addition to MB (Fig. II -6), doxorubicin (DOX, Fig. II -7), mitoxantrone (MTO, Fig. II -8) and protoporphyrin IX (PPIX, Fig. II -9) were tested for loading to the stemmed DNA nanostructures. Similar to MB, DOX, MTO, and PPIX showed negligible loading efficiencies to Apt or AptC15. Unlike Apt and AptC15, both ScrG15 and AptG15 revealed greater loading efficiencies for DOX, MTO, and PPIX.

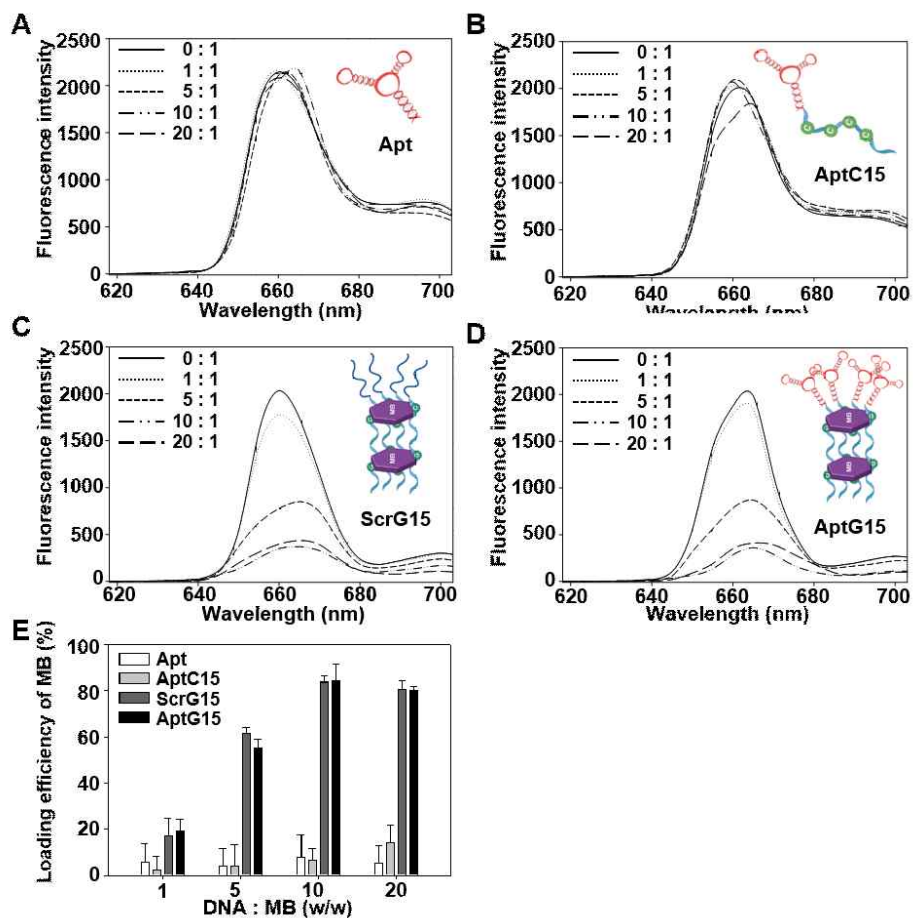


Fig. II -6. Binding of MB to DNA nanostructures.

Various weight ratios of DNA:MB were mixed, and the loadings of MB to Apt (A), AptC15 (B), ScrG15 (C), and AptG15 (D) were analyzed by fluorescence spectroscopy and quantified (E). The results were expressed as a mean of four separate experiments

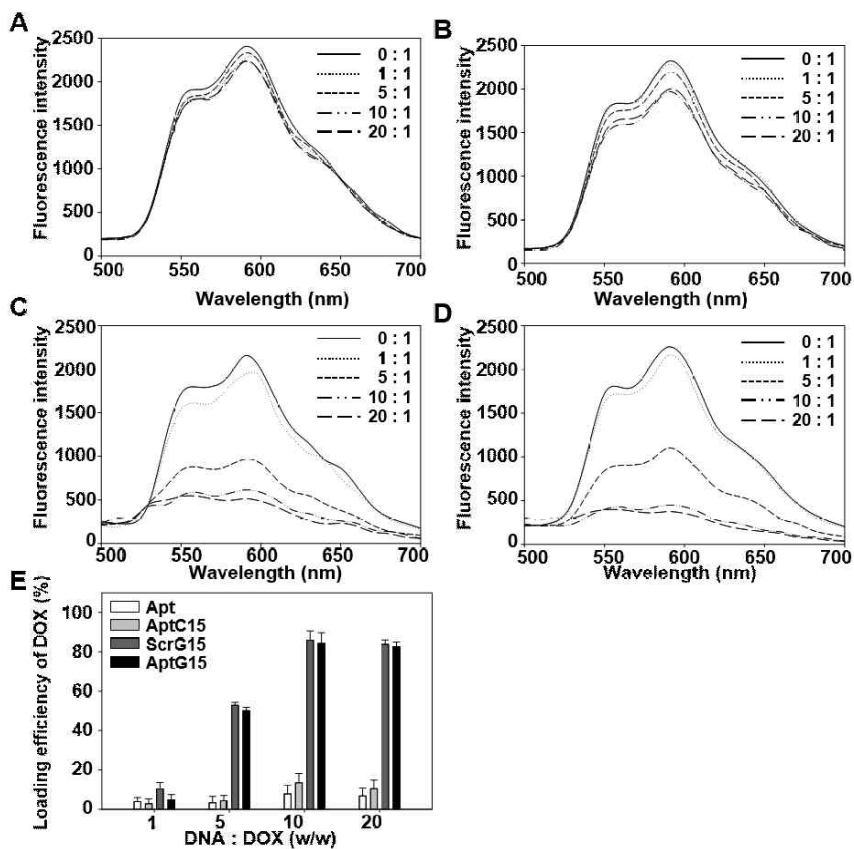


Fig. II -7. DOX loading onto stemmed DNA nanostructures.

Various weight ratios of DNA:DOX were mixed, and the loadings of DOX to Apt (A), AptC15 (B), ScrG15 (C) or AptG15 (D) were analyzed by fluorescence spectroscopy and quantified (E). The results were expressed as a mean of four separate experiments.

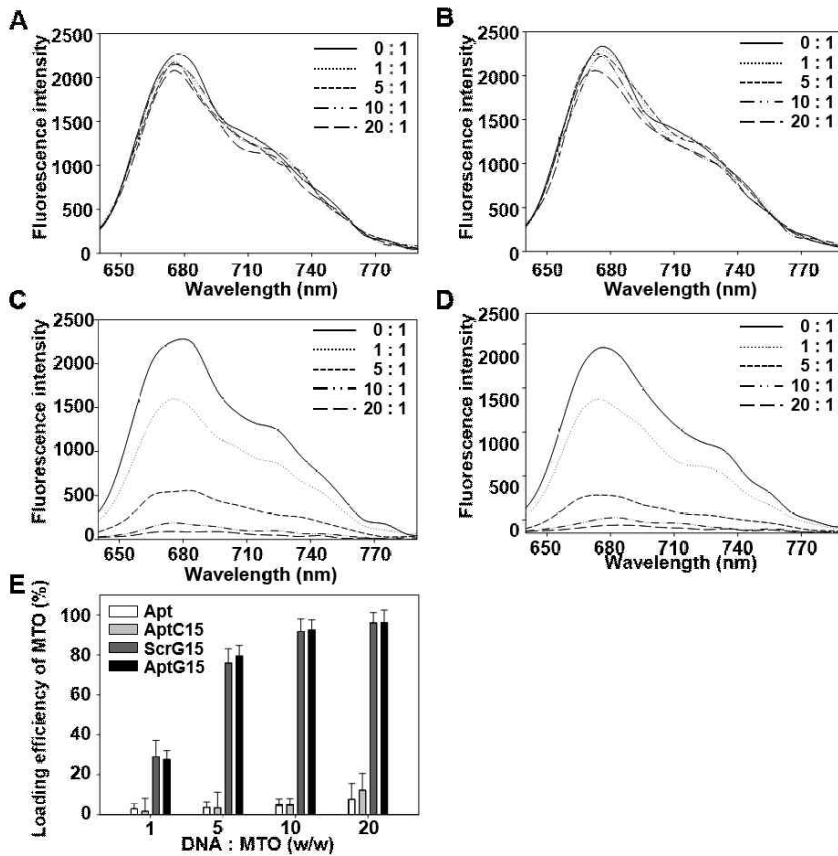


Fig. II-8. MTO loading onto stemmed DNA nanostructures.

Various weight ratios of DNA:MTO were mixed, and the loadings of MTO to Apt (A), AptC15 (B), ScrG15 (C) or AptG15 (D) were analyzed by fluorescence spectroscopy and quantified (E). The results were expressed as a mean of four separate experiments.

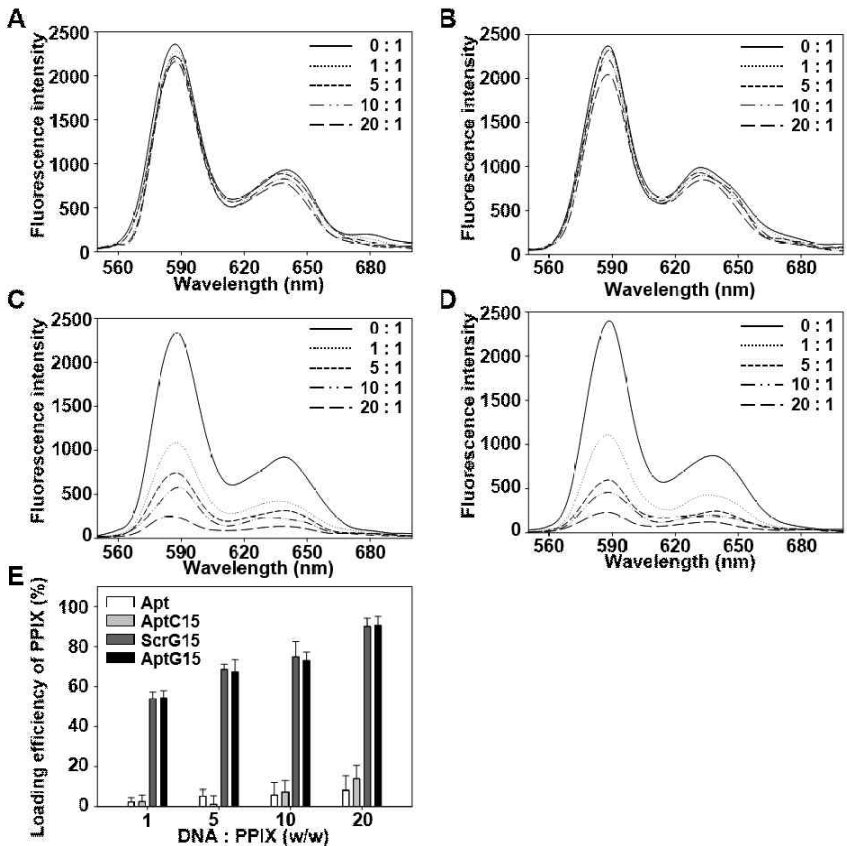


Fig. II-9. PPIX loading onto stemmed DNA nanostructures.

Various weight ratios of DNA:PPIX were mixed, and the loadings of PPIX to Apt (A), AptC15 (B), ScrG15 (C) or AptG15 (D) were analyzed by fluorescence spectroscopy and quantified (E). The results were expressed as a mean of four separate experiments.

3.5. Cellular uptake of drug-loaded DNA nanostructures

To test the cell-specific delivery of AptG15-loaded MB (MB/AptG15), we first treated CCRF-CEM cells with siPTK7 which knocked down PTK7 protein expression (Fig. II -10) as confirmed by flow cytometry. We then used flow cytometry to test whether MB uptake depended on the presence of the PTK7-targeting aptamer (Apt). Flow cytometry (Fig. II -11) revealed that the cellular uptake of MB/AptG15 was higher than those of MB/ScrG15, Apt, or free MB in PTK7-positive CCRF-CEM cells (Fig. II -11C), but no such difference was seen in PTK7-negative Ramos cells (Fig. II -11A) or PTK7-silenced CCRF-CEM cells (Fig. II -11B). Consistent with the flow cytometric data of MB/AptG15, DOX/AptG15, MTO/AptG15 and PPIX/AptG15 showed higher uptake in CCRF-CEM cells than other groups (Fig. II -12).

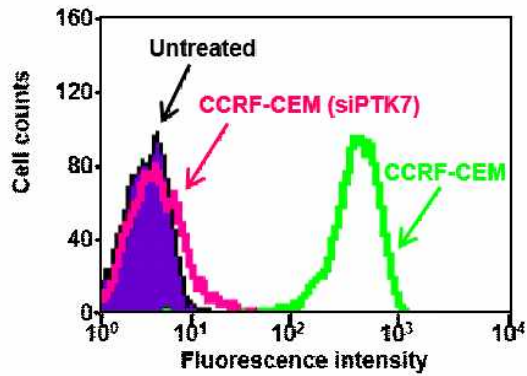


Fig. II -10. *In vitro* reduction of target PTK7 expression.

CCRF-CEM cells were transfected with siPTK7. Seventy-two hours post transfection, PTK7 proteins on the cell surfaces were stained with fluorescein-conjugated anti-PTK7 antibody and then analyzed by flow cytometry.

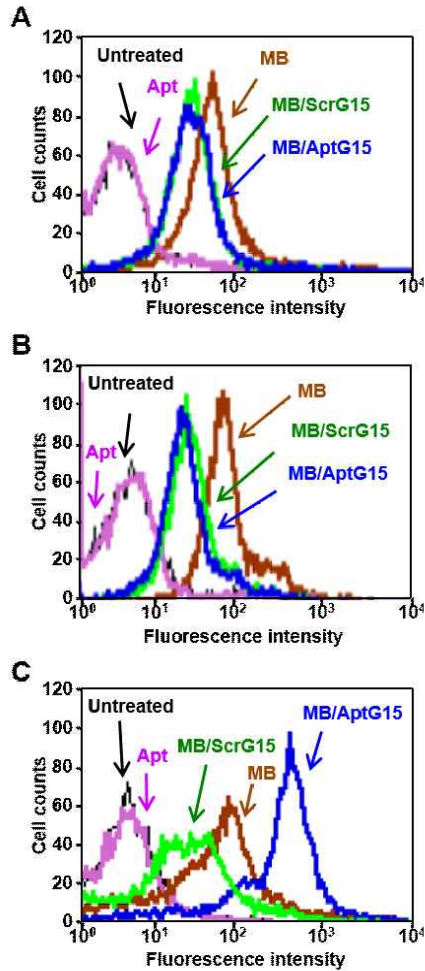


Fig. II -11. Cellular uptake of MB/AptG15 in PTK7-negative, PTK7-knockdown, and PTK7-positive cells.

Ramos cells (A), PTK7-knockdown CCRF-CEM cells (B), or CCRF-CEM cells (C) were left untreated or were treated with Apt, MB, MB/ScrG15, or MB/AptG15. After incubation for 15 min, cellular fluorescence was observed by flow cytometry.

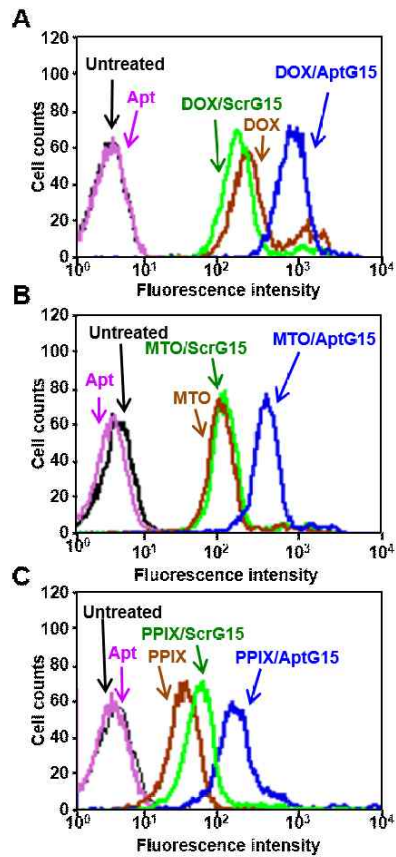


Fig. II -12. Cellular uptake of various drugs delivered by AptG15.

CCRF-CEM cells were seeded onto a 48-well plate at a density of 8×10^4 cells/well. On the next day, the cells were left untreated or treated with Apt, drug, drug/ScrG15, or drug/AptG15. Apt/G15-loaded drugs were DOX (A), MTO (B), or PPIX (C), respectively. After 15 min of incubation, the cellular fluorescence was evaluated by flow cytometry.

3.6. Light-induced cellular production of ROS

The cellular patterns of MB uptake (i.e., fluorescence quenching) were consistent with the cellular levels of ROS upon 660-nm light irradiation. In the absence of 660-nm LED irradiation, almost no cellular ROS was detected, and there was no significant between-group difference in the ROS levels of PTK7-negative Ramos cells (Fig. II-13A), PTK7-knockdown CCRF-CEM cells (Fig. II-13B), or PTK7-positive CCRF-CEM cells (Fig. II-13C) treated with the various nanostructures. Following LED irradiation, the ROS levels significantly differed among the nanostructure-treated groups in CCRF-CEM cells (Fig. II-14F), but not in Ramos cells (Fig. II-14B) or PTK7-knockdown CCRF-CEM cells (Fig. II-14D). MB/AptG15 triggered the highest level of ROS generation in CCRF-CEM cells, compared to MB/ScrG15, Apt, and free MB.

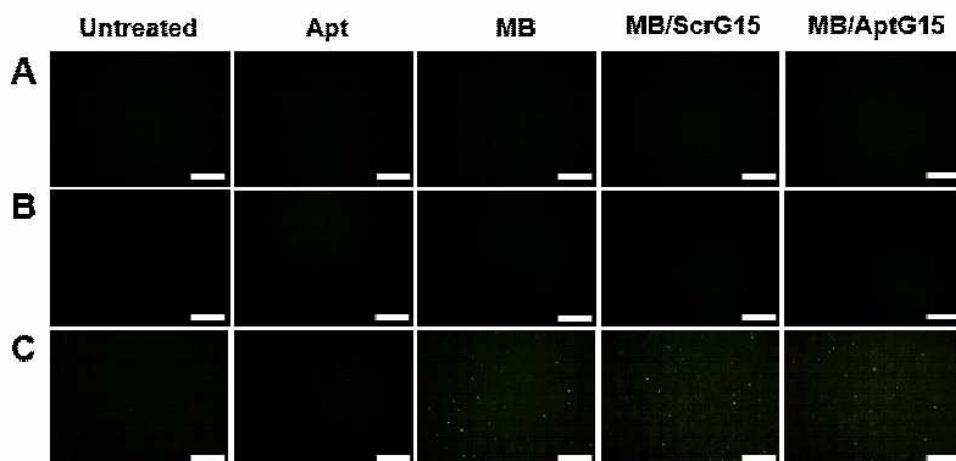


Fig. II -13. ROS production of PTK7-negative, -knockdown and -positive cells.

Ramos cells (A), PTK7-knockdown CCRF-CEM cells (B) and CCRF-CEM cells (C) were left untreated or treated with Apt, MB, MB/ScrG15, or MB/AptG15. After 10-min incubation, the fluorescence intensity of ROS indicator was observed using a fluorescence microscopy. Scale bar: 100 μ m.

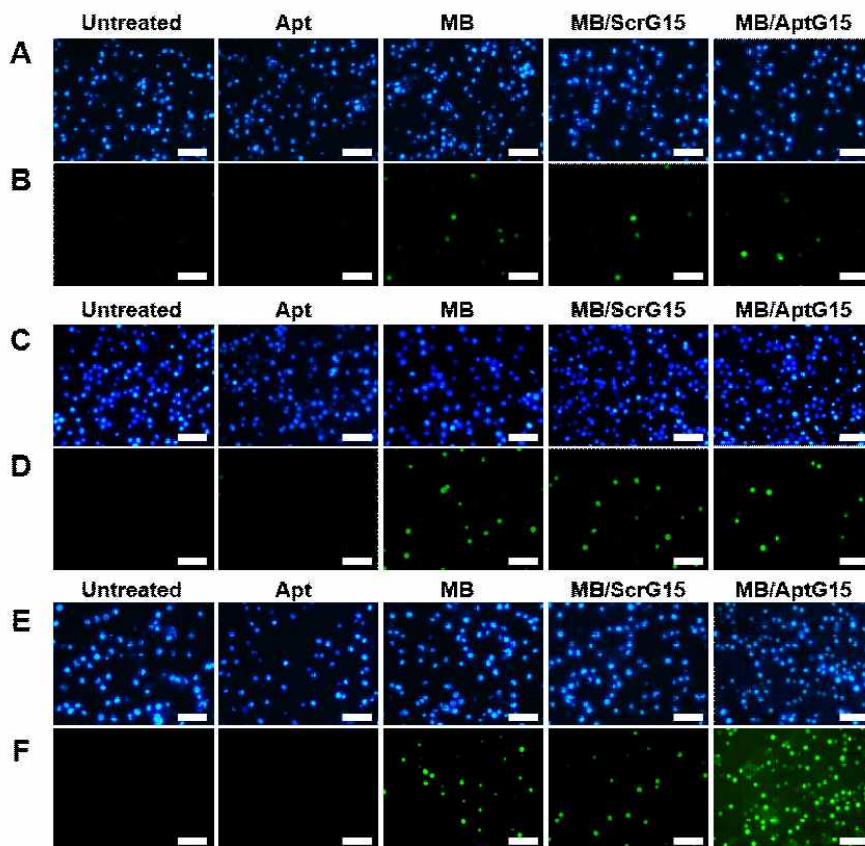


Fig. II -14. ROS production of PTK7-negative, PTK7-knockdown and PTK7-positive cells upon LED irradiation.

Ramos cells (A, B), PTK7-knockdown CCRF-CEM cells (C, D) and CCRF-CEM cells (E, F) were left untreated or treated with Apt, MB, MB/ScrG15, or MB/AptG15. After incubation for 10 min, the fluorescence intensity of DAPI (A, C, E) or ROS indicator (B, D, F) was observed using a fluorescence microscopy after 660-nm light irradiation. Scale bar: 100 μm .

3.7. Photodynamic anticancer activity

Cells were treated with the various formulations of MB and exposed to 660-nm light irradiation, and the photodynamic anticancer activity was evaluated by the MTT assay. In the absence of photo-irradiation, little cytotoxicity was observed regardless of treatment in PTK7-negative Ramos cells, PTK7-knockdown CCRF-CEM cells, and PTK7-positive CCRF-CEM cells (Fig. II -15A). In PTK7-negative Ramos cells and PTK7-knockdown CCRF-CEM cells, no significant differences were observed among groups after irradiation (Fig. II -15B). However, in PTK7-positive CCRF-CEM cells, LED irradiation (660-nm) triggered the highest cytotoxicity in cells treated with MB/AptG15 versus MB/ScrG15 or free MB, with MB/AptG15 significantly decreasing cell viability from $98.3\% \pm 7.8\%$ to $31.2\% \pm 1.0\%$ following LED irradiation (Fig. II -15B). In CCRF-CEM cells, fluorescence-dye-based live-cell staining revealed that the lowest fraction of viable cells was found in the MB/AptG15-treated group (Fig. II -16). Thus, our results indicate that the photodynamic anticancer effect was the highest in CCRF-CEM cells treated with MB/AptG15 plus 660-nm irradiation.

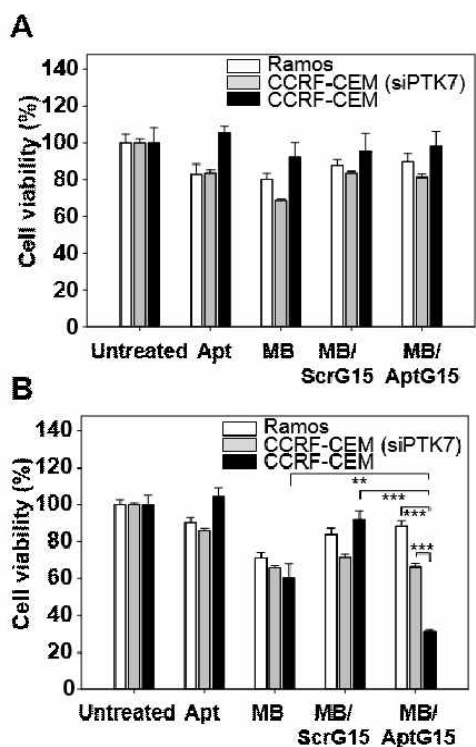


Fig. II -15. Photodynamic anticancer activity of DNA-nanostructure-treated PTK7-negative, -knockdown and -positive cells.

Ramos cells, PTK7-knockdown CCRF-CEM cells, or CCRF-CEM cells were left untreated or were treated with Apt, MB, MB/ScrG15, or MB/AptG15. The medium was replaced, and the cells were treated without (A) or with (B) irradiation using a 660-nm LED. The survivals of these cancer cell lines were measured by MTT assays. Data are presented as means of 4 separate experiments \pm SE.

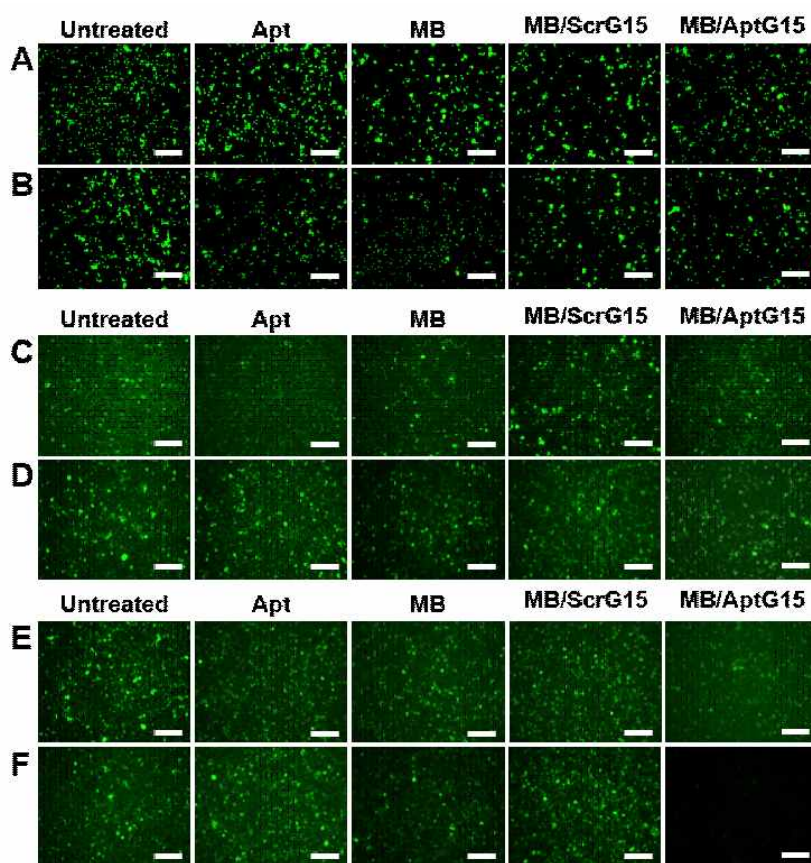


Fig. II -16. ROS production-inducing cell killing effect.

Ramos cells (A, B), PTK7-knockdown CCRF-CEM cell (C, D), and PTK7-positive CCRF-CEM cells (E, F) were left untreated or treated with Apt, MB, MB/ScrG15, or MB/AptG15. After incubation for 15 min, some cells (B, D, F) were irradiated using the 660-nm for 10 min. On the next day, cells were stained with 2 μ M of calcein-AM for 10 min. The stained live cell images were obtained using fluorescence microscopy (Leica DM IL). Scale bar: 100 μ m.

3.8. Illustration of the proposed mechanism through which MB/Apt15 induces ROS production and anticancer effects upon photo-irradiation

A mechanism for the anticancer effect of MB/AptG15 plus 660-nm light irradiation is proposed in Fig. II -17. Briefly, MB/AptG15 is taken up by PTK7 receptors on CCRF-CEM cells, MB is released, the liberated MB responds to 660-nm light irradiation by triggering ROS generation, and the generated ROS induces cell death.

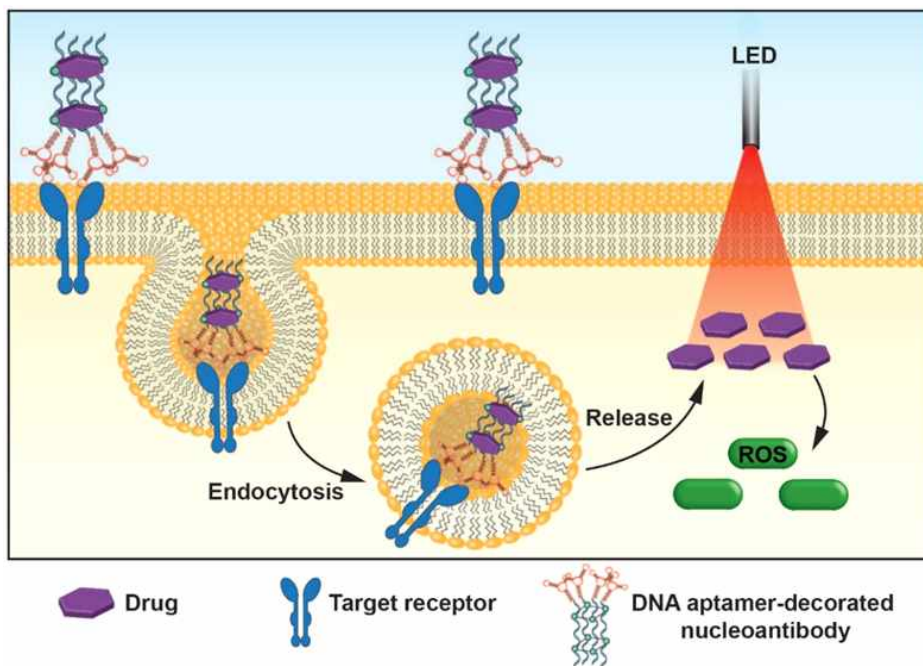


Fig. II -17. Schematic of the mechanism for the delivery and therapeutic effect of MB/AptG15.

Illustration of the proposed mechanism through which MB/Apt15 induces ROS production and anticancer effects upon photo-irradiation. MB/AptG15 enters CCRF-CEM cells via PTK7-mediated endocytosis due to the presence of the aptamer sequence. In an endolysosome, the MB, used as a model drug, is liberated by the degradation of DNA. In the cytosol, MB responds to photo-irradiation by producing ROS, which results in enhanced cell death.

4. Discussion

Here, we demonstrate that PTK7 aptamer-decorated AptG15 forms a Y-shaped configuration that includes a G-quadruplex DNA structure at stem part and describe the loading of MB as a model drug. We further report that MB bound to AptG15 shows enhanced cellular uptake to PTK7-positive cancer cells, leading to ROS production and cytotoxicity upon irradiation with 660-nm light.

AptG15 and ScrG15 self-assembled to form regular Y-shaped structures, whereas Apt and AptC15 did not. The Y-shaped structure of AptG15 is consistent with the previously observed self-assembly of 3'-terminal guanine residues [8]. The driving force for Y-shaped assembly is speculated to be the formation of G-quadruplex structures by 3'-end guanine residues. Indeed, guanine-rich DNA sequences have been shown to form G-quadruplexes in the presence of monovalent cations via interactions between guanine residues [9,10].

We herein used CD, Raman spectra and NMR analysis, which have previously been used to characterize DNA conformations [11-14], to characterize the structures of the generated DNA nanostructures. The CD spectra of AptG15 and ScrG15 were similar, indicating that the aptamer at the 5'-end of the oligodeoxyribonucleotide did not affect the stem structures

of the G-quartet. Previously, peak changes in absorbance spectra at 245 nm were shown to reflect an increase in the overall DNA concentration [15]. Thus, the similar 245-nm peaks obtained for AptG15 and ScrG15 indicate that their DNA concentrations were comparable. Previously, G-quadruplex structures were reported to show characteristic Raman bands [16,17]. In this study, the presence of Raman bands at 1480 cm⁻¹, 1578 cm⁻¹, and 1605 cm⁻¹ in ScrG15 and AptG15 but not in AptC15 or Apt supports the existence of G-quadruplex structures in the former pair.

The NMR spectra of ScrG15 and AptG15 showed peaks between 12 and 14 ppm originating from Watson-Crick hydrogen bonds. However, the spectra of ScrG15 and AptG15 exhibited additional peaks between 10 and 12 ppm which were originating from unusual G:G hydrogen bonds. The line broadening at the imino region of ScrG15 and AptG15 compared to Apt and AptC15 might be resulting from the large molecular weight of ScrG15 and AptG15.

As a model drug, we used MB, which we bound to the DNA nanostructures. Work in other laboratories has demonstrated that MB binds non-covalently to G-quadruplex DNA [18-20]. MB also has been reported to bind to single-stranded DNA [21,22]; however, the binding affinity of MB to G-quadruplex DNA is much greater higher than that to single-stranded

DNA [23].

To test the wide applicability of the stemmed DNA nanostructure for the delivery of various therapeutics, we further tested the loading and delivery of three drugs, namely DOX, MTO, and PPIX. Similar to MB, these drugs were loaded onto stemmed DNAs but not onto single-stranded DNAs (Fig. II 7-9). Moreover, the enhanced cellular uptake of these anticancer drugs delivered by Apt/G15 (Fig. II -12) supports the versatile applications of stemmed DNA structures for various therapeutics.

Previously, a G-quadruplex forming aptamer was reported to incorporate the photosensitizer for tumor-targeted delivery [24]. In the study, the AS1411 aptamer *per se* formed the G-quadruplex, limiting its application to other functional aptamers. However, in this study, the G15 oligomer-based quadruplex lacking target-recognizing activity was used as a separate stem structure. Such separation between the drug-loading stem part and the target-recognizing aptamer can allow the wide application of this system to various aptamers. Although in this study, we used PTK7 as a model aptamer to be linked to the stem part for targeted delivery.

We attribute the enhanced cellular uptake of MB/AptG15 over MB/ScrG15 to the overexpression of PTK7 on the surfaces of CCRF-CEM cells, as the DNA aptamer portion of AptG15, *sgc8*, is known to be taken up after

binding to the target receptor [25,26]. The similarity of cellular uptake between MB/AptG15 and MB/ScrG15 in PTK7-negative Ramos cells supports the idea that MB/Apt15 enters CCRF-CEM cells *via* PTK7. Moreover, the uptake of MB/AptG15 by CCRF-CEM was inhibited by transfection with siPTK7, further validating the notion that MB/AptG15 was taken up by cell-surface PTK7 receptors. We confirmed the knockdown of PTK7 using the flow cytometry of anti-PTK7 antibody in order to confirm the expression pattern of the cell surface [27].

We observed light-sensitive anticancer effects in MB/AptG15-treated CCRF-CEM cells. The enhancement of these anticancer effects over those conferred by the other MB formulations is presumably related to a greater production of ROS upon irradiation with 660-nm light. Indeed, lower ROS production and no anticancer effect was associated with treatment of CCRF-CEM cells with Apt alone, supporting the notion that MB played a crucial role in triggering the observed ROS-induced anticancer effects.

In this study, we used a 660 nm LED as a light source for photodynamic therapy. LEDs have been used as a light source for photodynamic studies for *in vitro* and *in vivo* studies [28, 29]. As compared to laser, LEDs have the advantages of being portable and less costly. Moreover, LEDs were reported to exert an efficiency similar to that of long-wave laser light [30].

Photodynamic therapy has been studied as a modality for noninvasive anticancer treatment [31], and the irradiation of photosensitizer-pretreated cancer tissues has been shown to induce ROS generation and subsequent cell death [32]. MB has been studied as a photosensitizer for photodynamic therapy, and reported to exert anticancer effects upon light irradiation [33].

In addition to MB, other therapeutics such as DOX, MTO, and PPIX were shown to be loadable to the stemmed DNA nanostructure. Here, the PTK7-dependent cellular delivery and photodynamic effect of various therapeutics suggest that AptG15 may minimize the nonspecific killing of normal cells while increasing the killing of aptamer-recognizable cancer cells.

5. References

- [1] Ouyang X., Li J., Liu H., Zhao B., Yan J., Ma Y., Xiao S., Song S., Huang Q., Chao J., Fan C. Rolling circle amplification-based DNA origami nanostructures for intracellular delivery of immunostimulatory drugs. *Small*. 2013; 18 (9): 3082-3087.
- [2] Hartman M.R., Yang D., Tran T. N. N., Lee K., Kahn J.S., Kiatwuthinon P., Yancey K.G., Trotsenko O., Minko S., Luo D. Thermostable branched DNA nanostructures as modular primers for polymerase chain reaction. *Angew. Chem. Int. Ed.* 2013; 52: 8699-8702.
- [3] Zhang Q., Jiang Q., Li N., Dai L., Liu Q., Song L., Wang J., Li Y., Tian J., Ding B., Du Y. DNA origami as an in vivo drug delivery vehicle for cancer therapy. *ACS Nano*. 2014a; 7 (8): 6633-6643.
- [4] Bi S., Dong Y., Jia X., Chen M., Zhong H., Ji B. Self-assembled

multifunctional DNA nanospheres for biosensing and drug delivery into specific target cells. *Nanoscale*. 2015; 7: 7361-7367.

- [5] Poon K., Macgregor Jr. R.B. Formation and structural determinants of multi-stranded guanine-rich DNA complexes. *Biophys. Chem.* 2000; 84: 205-216.
- [6] Abu-Ghazalah R.M., Irizar J., Helmy A.S., Macgregor Jr. R.B. A study of the interactions that stabilize DNA frayed wires. *Biophys. Chem.* 2010; 147: 123-129.
- [7] Protozanova E., Macgregor, Jr. R.B. Frayed Wires: A thermally stable form of DNA with two distinct structural domains. *Biochemistry*. 1996; 35: 16638-16645.
- [8] Poon K., Macgregor, Jr. R.B. Probing the structure of multi-stranded guanine-rich DNA complexes by Raman spectroscopy and enzymatic degradation. *Biophys. Chem.* 1999; 79: 11-23.
- [9] Galer P., Wang B., S`ket P., Plavec J. Reversible pH switch of two-quartet G-quadruplexes formed by human telomere. *Angew. Chem.* 2016; 128: 2033-2037.

- [10] Marchand A., Granzhan A., Iida K., Tsushima Y., Ma Y., Nagasawa K., Teulade-Fichou M.P., Gabelica V. Ligand-Induced Conformational changes with cation ejection upon binding to human telomeric DNA G quadruplexes. *J. Am. Chem. Soc.* 2015; 137: 750-756.
- [11] Gattuso H., Spinello A., Terenzi A., Assfeld X., Barone G., Monari A. Circular dichroism of DNA G-quadruplexes: combining modeling and spectroscopy to unravel complex structures. *J. Phys. Chem. B.* 2016; 6b00634.
- [12] Arte's J.M., Li Y., Qi J., Anantram M.P., Hihath J. Conformational gating of DNA conductance. *Nat. Commun.* 2015; 6: 8870.
- [13] Friedman S.J. and Terentis A.C. Analysis of G-quadruplex conformations using Raman and polarized Raman spectroscopy. *J. Raman Spectrosc.* 2016; 47: 259-268.
- [14] Lu L., Zhong H.J., He B., Leung C.H., Ma D.L. Development of a luminescent G-quadruplex-selective iridium(III) complex for the label-free detection of adenosine. *Sci. Rep.* 2016; 6: 19368.
- [15] Protozanova E., Macgregor, Jr. R.B. Circular Dichroism of DNA frayed wires. *Biophys. J.* 1998; 75: 982-989.
- [16] Wang C., Jia G., Zhou J., Li Y., Liu Y., Lu S., Li C.

Enantioselective Diels-Alder reactions with G-quadruplex DNA based catalysts. *Angew. Chem. Int. Ed.* 2012; 51: 9352-9355.

- [17] Wei C., Jia G., Yuan J., Feng Z., Li C. A spectroscopic study on the interactions of porphyrin with G-quadruplex DNAs. *Biochemistry.* 2006; 45: 6681-6691.
- [18] Chan D.S, Yang H., Kwan M. H., Cheng Z., Lee P., Bai L., Jiang Z., Wong C., Fong W., Leung C., Ma D. Structure-based optimization of FDA-approved drug methylene blue as a c-myc G-quadruplex DNA stabilizer. *Biochimie.* 2011; 93: 1055-1064.
- [19] Rodríguez-Llansola F., Miravet J.F., Escuder B. Aldehyde responsive supramolecular hydrogels: towards biomarker-specific delivery systems. *Chem. Commun.* 2011; 47: 4706-4708.
- [20] Peters G.M., Skala L.P., Plank T.N., Hyman B.J., Reddy G.N.M., Marsh A., Brown S.P., Davis J.T. A G4·K⁺ hydrogel stabilized by an anion. *J. Am. Chem. Soc.* 2014; 136: 12596-12599.
- [21] Xu P., Wang J., Xu Y., Chu H., Shen H., Zhang D., Zhao M., Liu J., Li G. Chapter 12 Binding modes and interaction mechanism between different base pairs and methylene blue trihydrate: a quantum mechanics study. *Adv. Struct. Eng.* 2015; 827: 187-203.

- [22] Tong C., Hu Z., Wu J. Interaction between methylene blue and calf thymus deoxyribonucleic acid by spectroscopic technologies. *J. Fluoresc.* 2010; 20: 261-267.
- [23] Zhang F.T., Nie J., Zhang D.W., Chen J.T., Zhou Y.L., Zhang X.X. Methylene blue as a G quadruplex binding probe for label-free homogeneous electrochemical biosensing. *Anal. Chem.* 2014b; 86: 9489-9495.
- [24] Xiao Z., Shangguan D., Cao Z., Fang X., Tan W. Cell-specific internalization study of an aptamer from whole cell selection. *Chem. Eur. J.* 2008; 14: 1769-1775.
- [25] Kim M.G, Park J.Y., Miao W., Lee J., Oh Y.K. Polyaptamer DNA nanothread-anchored, reduced graphene oxide nanosheets for targeted delivery. *Biomaterials.* 2015; 48: 129-136.
- [26] Dolmans D. E.J.G.J., Fukumura D., Jain R. K. Photodynamic therapy for cancer. *Nat Rev Cancer.* 2003;3:380-387.
- [27] Prebet T., Lhoumeau A.C., Arnoulet C., Aulas A., Marchetto S., Audebert S. Puppo F., Chabannon C., Sainty D. Santoni M.J. Sebbagh M., Summerour V., Huon Y., Shin W.S., Lee S.T., Esterni B., Vey N., Borg J.P. The cell polarity PTK7 receptor acts as a modulator of the chemotherapeutic response in acute myeloid leukemia and impairs

clinical outcome. *Blood*. 2010;116(13): 2315-2323.

- [28] Lin L.S., Gong Z.X., Li J., Ke K.M., Guo S.S., Yang H.H., Chen G.N. Graphitic-phase C₃N₄ nanosheets as efficient photosensitizers and pH-responsive drug nanocarriers for cancer imaging and therapy. *J Mater Chem B*. 2014; 2: 1031-1037.
- [29] Zhang Q., Cai Y., Li Q.Y., Hao L.N., Ma Z., Wang X.J., Yin J. Targeted delivery of a mannose-conjugated BODIPY photosensitizer by nanomicelles for photodynamic breast cancer therapy. *Chem.-Eur.J*. 2017;23:14307-14315.
- [30] Takahashi H., Nakajima S., Ogasawara K., Asano R. Nakae Y., Sakata I., Iiuka H. Photodynamic therapy using a novel irradiation source, LED lamp, is similarly effective to photodynamic therapy using diode laser or metal-halide lamp on DMBA- and TPA-induced mouse skin papillomas. *J Dermatol*. 2014;41:729-731.
- [31] Castano A.P., Mroz P., Hamblin M.R. Photodynamic therapy and anti-tumour immunity. *Nat Rev Cancer*. 2006; 6: 536-545.
- [32] Robertson C. A., Evans E. H., Abrahamse h. Photodynamic therapy (PDT): a short review on cellular mechanisms and cancer research applications for PDT. *J Photochem Photobiol B*. 2009;96:1-8.

- [33] Sahu A., Choi W.I., Lee J.H., Tae G. Graphene oxide mediated delivery of methylene blue for combined photodynamic and photothermal therapy. *Biomaterials*. 2013; 34: 6239-6248.

Chapter III

Serial-controlled delivery of nanomaterials by sequential activation in tumor microenvironment

1. Introduction

Tumor-targeted delivery has been long studied using ligand-modified nanomaterials. As tumor-targeting ligands, folic acid [1], transferrin [2], and RGD peptide [3,4] have been extensively studied. Although progresses have been made using these single ligand-modified nanomaterials, the importance of tumor microenvironments has increased for the delivery of nanomaterials to tumor tissues. Recent studies reported that tumor microenvironment-responsive activation of drug delivery may increase the selectivity of tumor-directed nanomaterial delivery [5].

In some tumors, cathepsin L and urokinase-type plasminogen activator receptor (UPAR) have been known to be overexpressed in tumor microenvironment and tumor cell surfaces, respectively. Cathepsin L has been known to be secreted to the tumor microenvironment. Cathepsin L secreted to the tumor microenvironment has been known to play an important role for tumor metastasis [6], and neovascularization [7]. UPAR has been known to be overexpressed on various cancer cell surfaces such as breast cancer cells [8-10].

In this study, taking advantage of cathepsin L and UPAR, we designed multi-controlled peptide-modified nanomaterials for activation in tumor microenvironment and sequential recognition to UPAR on tumor cells. Using

reduced graphene oxide (rGO) nanosheets as a model nanomaterial, we coated the surfaces of rGO with cyclic peptide which can be cleaved to linear UPAR-binding peptide by cathepsin L in tumor microenvironment. The cathepsin L-cleaved linear UPAR-binding peptide on rGO would then bind to UPAR-overexpressing tumor cells. The delivery efficiency of cyclic peptide-loaded rGO to tumor was evaluated by photothermal anticancer activity of rGO upon near infrared (NIR) irradiation (Fig. III-1).

2. Materials and methods

2.1. Synthesis of peptide derivatives

Synthesis schemes for peptides, polyethyleneglycol (PEG) conjugation, and chlorin e6 (Ce6) conjugation are depicted in Fig. III-2. Peptides were chemically synthesized by Fmoc (9-fluorenylmethyloxycarbonyl) solid-phase peptide synthesis on Wang resins. Amino acid sequences of scrambled peptide, cathepsin L-sensitive scrambled peptide, UPAR-binding peptide, and cathepsin L-sensitive UPAR-binding peptide are listed in Fig. III-1.

PEG conjugation of the peptides was conducted by treatment with 1.5 equivalent of Fmoc-PEG-succinimide, diisopropylethylamine in dimethylformamide (DMF) for 12 h. For conjugation of pegylated peptide with Ce6 in cyclic structure, O-(6-chlorobenzotriazol-1-yl)-N,N,N',N'-tetramethyluroniumhexafluorophosphate / diisopropyl-ethylamine was employed. In brief, Dde (1-(4,4-dimethyl-2,6-dioxocyclohex-1-ylidene)ethyl) group was deprotected with 2% hydrazine hydrate in DMF, and followed by cyclization with O-(6-Chlorobenzotriazol-1-yl)-N,N,N',N'-tetramethyluroniumhexafluorophosphate and diisopropylethylamine in DMF for 12h. After synthesis, resin detachment were performed using trifluoroacetic acid-water-triisopropyl silane (95:2.5:2.5) at room temperature for 4h followed by purification via revers-phase

high-performance liquid chromatography (HPLC).

The structures of cyclic Ce6-conjugated pegylated scrambled peptide (SP), Ce6-conjugated pegylatedcathepsin L-sensitive scrambled peptide (CSP), Ce6-conjugated pegylatedUPAR-binding peptide (UP), and Ce6-conjugated pegylatedcathepsin L-sensitive scrambled peptide (CUP) are depicted in Fig. 1. The fidelity of the products was ascertained by matrix-assisted laser desorption ionization time-of-flight mass spectrometry (MALDI-TOFMS): SP: observed, 4700~5300 [expected for 5200]; CSP: observed, 5700~6300 [expected for 5900]; UP: observed, 5100~5300 [expected for 5200]; CUP: observed, 5400~6200 [expected for 5900], respectively.

2.2. Synthesis of rGO nanosheets

rGO nanosheets were synthesized using a modified Hummer's method [11]. Briefly, graphite powder (0.5 g; Sigma-Aldrich) was dissolved in cold H₂SO₄ (23 mL). Then KMnO₄ (3 g; Sigma-Aldrich) and NaNO₃ (0.5 g; Sigma-Aldrich) were added to the solution. The mixture was stirred for an additional 1 h and incubated at 90 °C for 1 h after adding triple-distilled water (TDW, 46 mL). The reaction was halted by adding TDW (140 mL) and H₂O₂ (30 %, 10 mL). To exfoliate the GO layers into GO nanosheets, the TDW suspended final product was sonicated for 2 h at a power setting

of 400 W, centrifuged at 1600 ×g for 10 min, and the supernatant was filtered through 0.2 μm polycarbonate membrane filters (Millipore Corp., Billerica, MA, USA) using an extruder (Northern Lipid, British Columbia, Canada).

The purified GO nanosheets were subsequently reduced to generate rGO nanosheets according to the method of Li and colleagues. In short, GO nanosheets (5 mg/ml, 2 ml) were mixed with TDW (8 ml) containing ammonia solution (28 wt.% in water, 0.5 ml; Junsei Chemical, Tokyo, Japan) and hydrazine monohydrate (64 wt.% in water, 5 μl; Sigma-Aldrich) and stirred at 80 °C for 10 min. After cool down the mixture to room temperature, extra hydrazine and ammonia were discarded by dialysis (MWCO 100K; Spectrum Laboratories, Inc., Rancho Dominguez, CA, USA) against TDW. The resulting rGO nanosheets were stored at 4 °C until use.

2.3. Preparation of peptide derivative-tethered rGO

SP, CSP, UP or CUP was anchored on the surface of rGO nanosheets by mixing the same volume of each peptide (1.8 mmol/L) with the rGO nanosheets in TDW (1 mg/ml). Peptide-tethered rGO nanosheets were then obtained by centrifugation at 14,000×g for 30 min using an Amicon Ultra centrifugal filter (MWCO 100K; Millipore, Darmstadt, Germany). In filtrated

solution, the amounts of unbound peptide derivatives were evaluated at a wavelength of 400 nm (Gemini XS; Molecular Device, Sunnyvale, CA, USA). By subtracting the unbound peptide amount from initial amount, the loading amount of peptides onto rGO nanosheets were analyzed.

2.4. Characterization studies of surface-modified rGO nanosheets

The peptide derivative-tethered rGO nanosheets were characterized by analyzing morphology, size and zeta potential. The morphologies of each peptide-tethered rGOs were evaluated by transmission electron microscopy (TEM) using a JEM1010 transmission electron microscope (JOEL Ltd., Tokyo, Japan). The rGO nanosheets for TEM imaging were prepared onto a carbon grid (Agar Scientific Ltd., Stansted, United Kingdom) after dropping the rGO suspension and drying completely. The lateral diameters of the rGOs were measured using a 10 mW power of He-Ne laser equipped dynamic light scattering ELSZ-1000 instrument (Photal, Osaka, Japan). After diluted in TDW, the zeta potential values of rGOs were evaluated by laser Doppler microelectrophoresis at an angle of 22°.

2.5. In vitro assay of CTSL

Activity of CTSL released from various tumor cells were quantitated using a

commercial kit (Cathepsin L activity fluorometric assay kit, BioVision Inc., Milpitas, CA, USA). In brief, cells were seeded onto a 6-well plate at a density of 1×10^5 cells/well. After two days, the supernatant was mixed with AFC (amino-4-trifluoromethyl coumarin)-conjugated CTSL substrate (200 μ M) and dithiothreitol (10 mM). Culture media alone was used as a negative control. After 2 hr incubation at 37°C with gentle shaking, the fluorescence intensity was measured using a fluorescence microplate reader at an excitation wavelength of 400 nm and an emission wavelength of 505 nm. The resulting value was converted into CTSL activity by generating a standard curve of CTSL.

2.6. Photothermal properties of nanosheets

The photothermal properties of the peptide-coated rGO nanosheets were measured using an IR thermal imaging system after irradiation of each sample using near infrared (NIR) laser. The coated rGOs were irradiated using an 808 nm continuous wave NIR laser (PSU-FC, ChangChun New Industries Optoelectronics Tech. Co., LTD, Changchun, China) with an output power of 1.5 W. During laser irradiation, the temperature of the rGO suspensions was recorded in real time and the thermal images were obtained and processed using an IR thermal imaging system (FLIR T420; FLIR

Systems Inc., Danderyd, Sweden).

2.7. Measurement of UPAR expression on cell surfaces

The expression of UPAR on the surfaces of TCMK-1, mouse kidney cell or CCRF-CEM, leukemia cell or HT-29, colon cancer cell were evaluated by flow cytometry technique. The cells were incubated for 1 h with bovine serum albumin (BSA) containing PBS to prevent non-specific binding. After wash with cold PBS one time, the cells were incubated for another 1hr at room temperature with a PerCP-eFluor710 conjugated anti-UPAR monoclonal antibody (eBioscience Inc., SanDiego, CA, USA) at a dilution of 1:100. UPAR-expressing cell populations were proved using a Cell Quest Pro software equipped BD FACSCalibur system (BD Bioscience, San Jose, CA, USA).

2.8. Cellular uptake study

Cellular uptake of variously prepared rGO nanosheets was evaluated using flow cytometry and confocal microscopy. For flow cytometry, TCMK-1 or CCRF-CEM or HT-29 cells were seeded onto 24-well plates at a density of 5×10^4 cells/well. After overnight incubation, cells were treated with SP, CSP, UP or CUP loaded rGO for 20 min at an amount of 48 μg rGO with

20 μM of peptide. The cells were harvested then washed three times with 2% fetal bovine serum-containing cold PBS and analyzed by the BD FACSCalibur system. For confocal microscopy, TCMK-1 or HT-29 cells were seeded onto cover glasses at a density of 5×10^4 cells/well in 24 well plates. The next day, the cells were treated with 48 μg of rGO with or without 20 μM of peptide for 20 min. In case of CCRF-CEM cell line, cells were transferred onto poly-L-lysine coated glasses (BD Biosciences, San Jose, CA, USA) and incubated for 1 h for attachment and then treated as described above. The glass-attached cells were fixed with 4% paraformaldehyde in PBS for 15 min and stained with 4'6-diamidino-2-phenylindole dihydrochloride (Sigma-Aldrich). The fluorescence intensity of cellular Ce6 was observed using a confocal laser-scanning microscope (LSM Exciter; Carl Zeiss Inc., Jena, Germany).

2.9. In vitro photothermal effect measurement

TCMK-1, CCRF-CEM, or HT-29 cells were seeded onto 12 well plates at a density of 1×10^5 cells/well. The next day, the cells were treated with variously prepared rGO nanosheets at 48 μg of the rGO nanosheets with or without 20 μM peptide. After 4 hr of incubation at 37 $^{\circ}\text{C}$, the cells were harvested and centrifuged at 100g for 3 min. The 808 nm continuous wave

NIR diode laser irradiation was applied to the cells at an output power of 1.5 W/cm². During the 5 min irradiation, the temperature was monitored in real time and the photothermal images were recorded every minute using an IR thermal imaging system (FLIR T420).

2.10. In vitro cell viability study

The cell viability was quantified by MTT assay or live cell staining. The cells were seeded onto 12-well plates at a density of 1×10^5 cells/well. The next day, the cells were treated for 4 hr with plain rGO or variously prepared rGO at 48 µg of rGO with 20 µM of each peptide. The cells were collected after washing and irradiated with the 808 nm NIR laser for 5 min. After the irradiation, the cells were seeded onto 48-well plates and incubated for 24 h to evaluate the cell viability. For MTT assay, 500 µM of MTT (3-(4, 5-dimethylthiazol-2-yl)-2, 5-diphenyltetrazolium bromide, Sigma-Aldrich) solution was added to each well for 2 hr at 37 °C. After removal of the media, the resulting crystals were dissolved in 200 µL of dimethyl sulfoxide (Sigma-Aldrich) the absorbance was measured at 570 nm using a microplate reader (Tecan Group Ltd., Seestrasse, Mannedorf, Switzerland). For live cell staining, 2 µM calcein (Invitrogen Corp., Carlsbad, CA, USA) was added to each well to stain the cells fluorescently.

After 10 min incubation, the cells were washed and the images of stained live cells were obtained using fluorescence microscopy (Leica DM IL, USA).

2.11. Molecular imaging

Molecular whole body imaging was conducted to evaluate the distribution of peptide-loaded rGO in tumor-bearing mice. Five week-old athymic nude female mice (Orient Bio Inc., Seungnam, Republic of Korea; approved animal experimental protocol number SNU-150609-2-1) were subcutaneously inoculated at the dorsal middle part with 5×10^6 HT-29 cells in PBS or CCRF-CEM cells in 50% matrigel (BD Biosciences) containing PBS solution. The prepared SP/rGO, CSP/rGO, UP/rGO or CUP/rGO at the rGO dose of 10 mg/kg and peptide dose of 5 mg/kg were intravenously administered into the tumor established mice. At 1 hr, 24 hr, 48 hr post dose, the fluorescence signals of mice were scanned and the images were obtained using an eXploreOptix system (Advaned Research Technologies Inc., Montreal, Canada) with a laser power of 25 mW and a count time of 0.3 s/point. The Ce6 was excited by a 670 nm pulsed laser diode and the long-wave fluorescence emission was detected.

2.12. In vivo photothermal effect

The photothermal effect in vivo was examined by NIR laser irradiation at tumor site following variously prepared rGO administration. First, 5×10^6 HT-29 in PBS or CCRF-CEM cells in PBS with matrigel were subcutaneously injected at the dorsal left side of five-week old female Balb/c athymic nude mice (Orient Bio Inc.). When the tumor volumes reached 80-130 mm³, plain rGO or the peptide anchored rGOs were administrated to tail vein of the mice. After 4 hr, the mice were anesthetized by intraperitoneal Avertin injection. The tumor sites were left unirradiated or irradiated with an 808 nm NIR laser at an output power of 1.5 W/cm² for 10 min. The temperature changes during the irradiation was recorded using a real-time infrared thermal imaging system (FLIR T420) and the optical images were obtained using a digital camera (Canon PC 1089). The tumor size was measured using a slide caliper upto 33 days and the tumor volume was calculated according to the equation $0.5 \times (\text{largest diameter}) \times (\text{smallest diameter})^2$. Some tumor tissues were extracted 24h after the administration and/or NIR irradiation for immunostaining with an anti-proliferating cell nuclear antigen (PCNA) antibody and assayed by terminal deoxynucleotidyl transferase dUTP nick-endlabeling (TUNEL).

2.13. Statistics

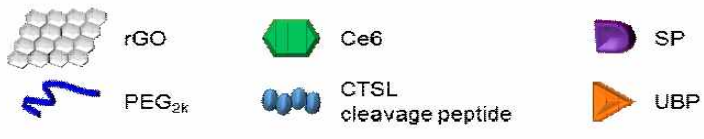
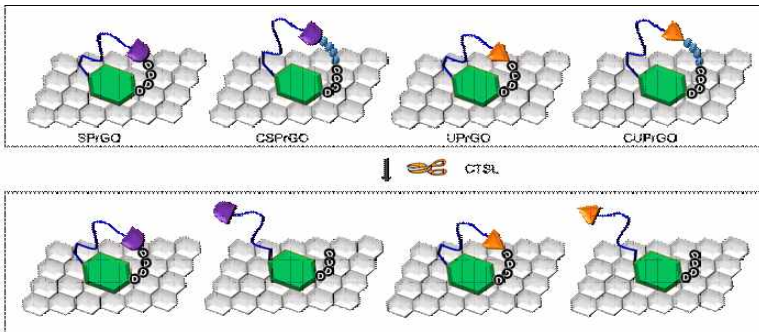
ANOVA was used for statistical evaluation of data, using Student-Newman-Keuls test as a post-hoc test. All statistical analyses were carried out using SigmaStat software (version 3.5, Systat Software, Richmond, CA, USA), and a p-value < 0.05 was considered significant.

3. Results

3.1. Characteristics of surface-modified rGO nanosheets

A possible working mechanism of CUP/rGO is illustrated in Figure III-1. Surfaces of rGO nanosheets were modified with SP, CSP, UP or CUP via physical adsorption with Ce6 as an anchoring moiety. The loading amounts of Ce6-conjugated peptides onto the rGO nanosheets were not significantly different regardless of amino acid sequences (Fig. III-4).

The adsorption of peptide derivatives onto rGO did not affect the morphologies. TEM imaging of SP/rGO, CSP/rGO, UP/rGO, and CUP/rGO did not differ from that of plain rGO (Fig. III-3A). The lateral size (Fig. III-3B) and zeta potential (Fig. III-3C) values of nanosheets were not affected by surface modification.



Peptide sequences are followed

SP: **Ce6**PEG_{2k}YSELPTFNHMQWALSPDDDDK

CSP: **Ce6**PEG_{2k}YSELPTFNHMQWALSPHRYRDDDDK

UP: **Ce6**PEG_{2k}A**EPMPHSLNFSQYLWYT**DDDDK

CUP: **Ce6**PEG_{2k}A**EPMPHSLNFSQYLWYTHR**YRDDDDK

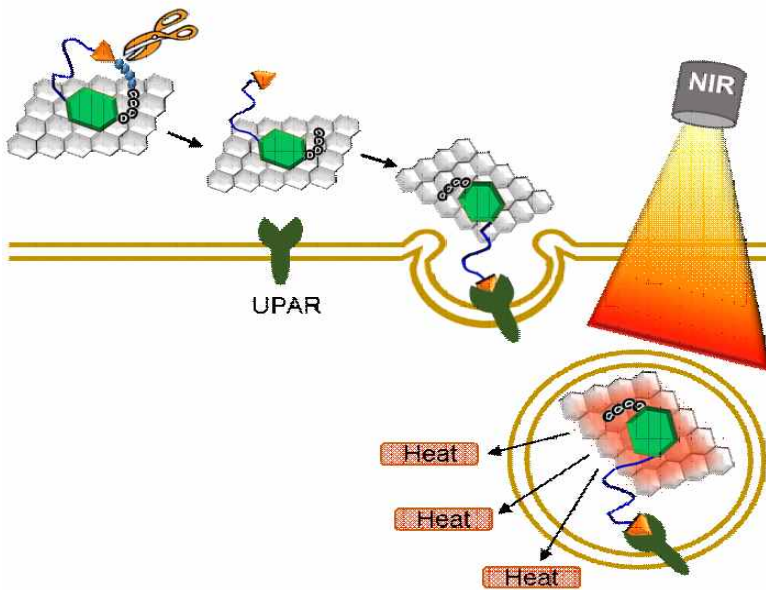


Fig. III-1. Nanostructure of CUP loaded rGO and a schematic illustration of mechanism of action.

Schematic diagram shows the mechanism of CUP/rGO. CUP/rGO was composed of the cleavage action peptide (CA), the UPAR targeting peptide (UPAR), the photothermal carrier (rGO), the fluorescence anchor(Ce6) and the hydrophilic PEG2k. The UPAR could be liberated upon the CA is cleaved by CTSL at near HT-29 cells. After CA missing, UPAR/rGO may enter the cells via UPAR-mediated endocytosis due to the presence of the UPAR ligand. The internalized complex was released to cytoplasm and the 808 nm NIR irradiation induced heat generation from rGO to exert photothermal activity. The variously prepared rGO groups were summarized below.

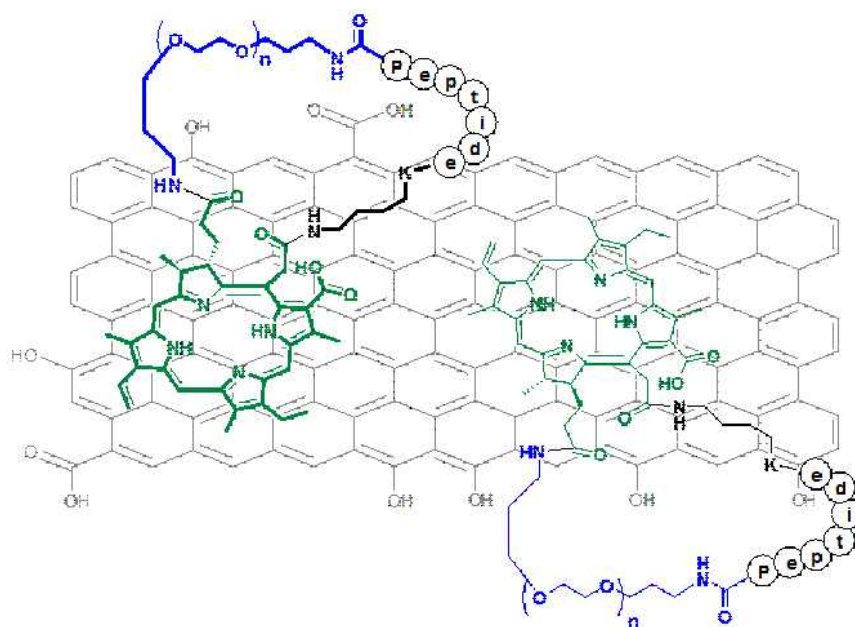


Fig. III-2. Synthesis scheme of PEG₂₀₀₀-Ce6 conjugated peptide.

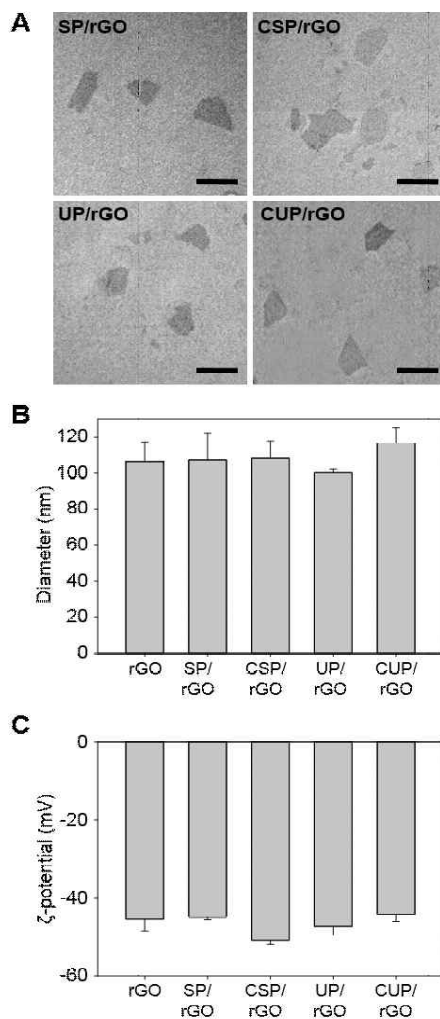


Fig. III-3. Size and zeta potentials of the surface-modified rGO nanosheets.

(A) Transmission electron microscopy images of plain rGO, SP/rGO, CSP/rGO, UP/rGO and CUP/rGO are presented (scale bars indicate 100 nm).

(B) The lateral sizes of the nanosheets were measured using dynamic light scattering method. (C) The zeta potential values of the prepared rGOs were determined by laser Doppler microelectrophoresis at an angle of 22° using an ELSZ-1000 instrument.

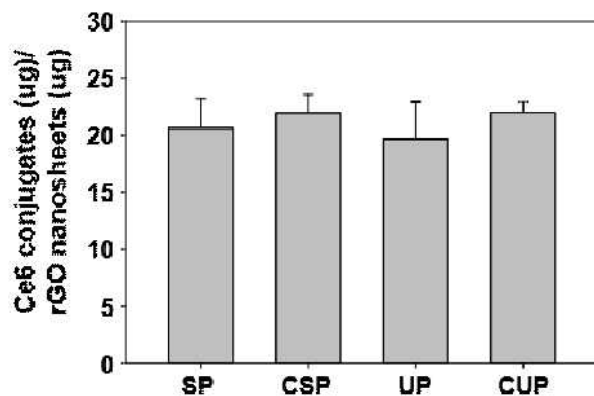


Fig. III-4. Loading amount of peptides onto rGO nanosheets.

The amounts of Ce6-conjugated peptides loaded onto the rGO nanosheets were quantified. Each complex of the amino acid sequences and rGO nanosheets was prepared by simple mixing and then condensed. The absorbance of fluorescence was evaluated using microplate reader.

3.2. CTSL-sensitive cleavage of peptide on rGO

The secretion levels of CTSL in culture media were significantly different among the cells. As compared to TCMK-1 and CCRF-CEM cells, HT-29 cells showed 18.4- and 122.3-fold higher activity of CTSL (Fig. III-5A). Using the binding of biotinylated and FITC-labeled peptide on streptavidin-coated plate, the cleavage of peptide was detected by the fluorescence of supernatant. In line with the cathepsin L levels, the cleavage of CUP depended on the type of the cells. Incubation of CUP in the culture media of TCMK-1 and CCRF-CEM cells showed little cleavage of CUP. In contrast, the incubation of CUP in cathepsin L-rich HT-29 cell culture media showed 12.9-fold and 12.0-fold higher cleavage of CUP compared to the samples treated with TCMK-1 and CCRF-CEM cells culture media, respectively (Fig. III-5B).

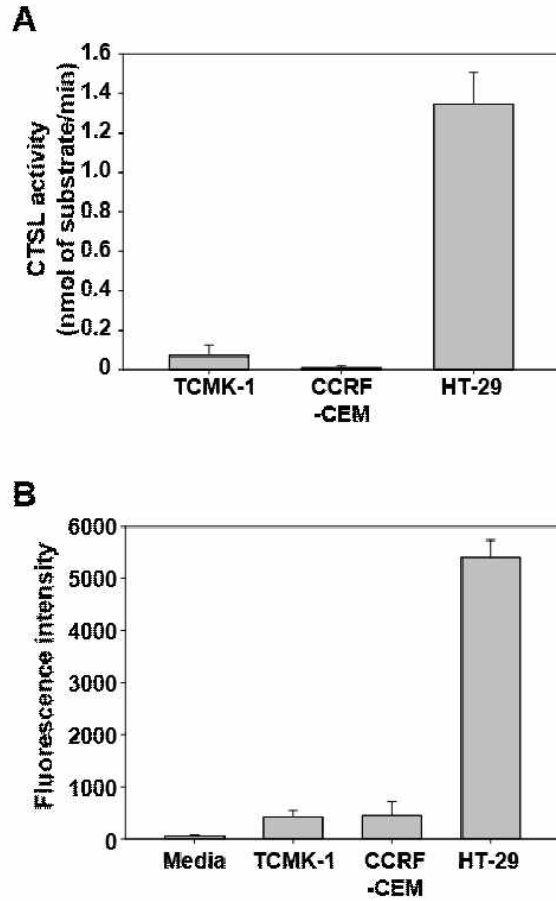


Fig. III-5. Enzyme cleavable activity analysis on TCMK-1, CCRF-CEM, and HT-29 cells.

(A) Commercially available kit and (B) streptavidin-biotin system was adapted to measure cleavage efficiency of cell releasing enzyme.

3.3. Cellular uptake of CUP/rGO nanosheet

The cellular uptake of CUP/rGO nanosheets depended on the surface expression levels of UPAR. Flow cytometry using fluorescence-labeled anti-UPAR antibody revealed that the expression levels of UPAR were negligible in TCMK-1 (Fig. III-6A) and CCRF-CEM cells (Fig. III-6B), but substantial in HT-29 cells (Fig. III-6C). In accordance with the UPAR expression levels, the uptake of CUP-loaded rGO nanosheets depended on the cell types. The uptake of CUP-loaded rGO nanosheets was not significantly different with those of other peptide-coated nanosheets in TCMK-1 (Fig. III-6D) and CCRF-CEM cells (Fig. III-6E). In HT-29 cells, the uptake of CUP-loaded rGO nanosheets was significantly higher than other peptide-modified nanosheets such as scrambled peptide-modified rGO nanosheets (Fig. III-6F).

In addition to the flow cytometry, confocal microscopy was used to evaluate the cellular uptake of surface-modified rGO nanosheets by the fluorescence of Ce6 liberated from rGO nanosheets after endocytosis. In HT-29 cells, the colocalization of DAPI and Ce6 was observed after treatment with UP/rGO and CUP/rGO, but not in SP/rGO (Fig. III-7).

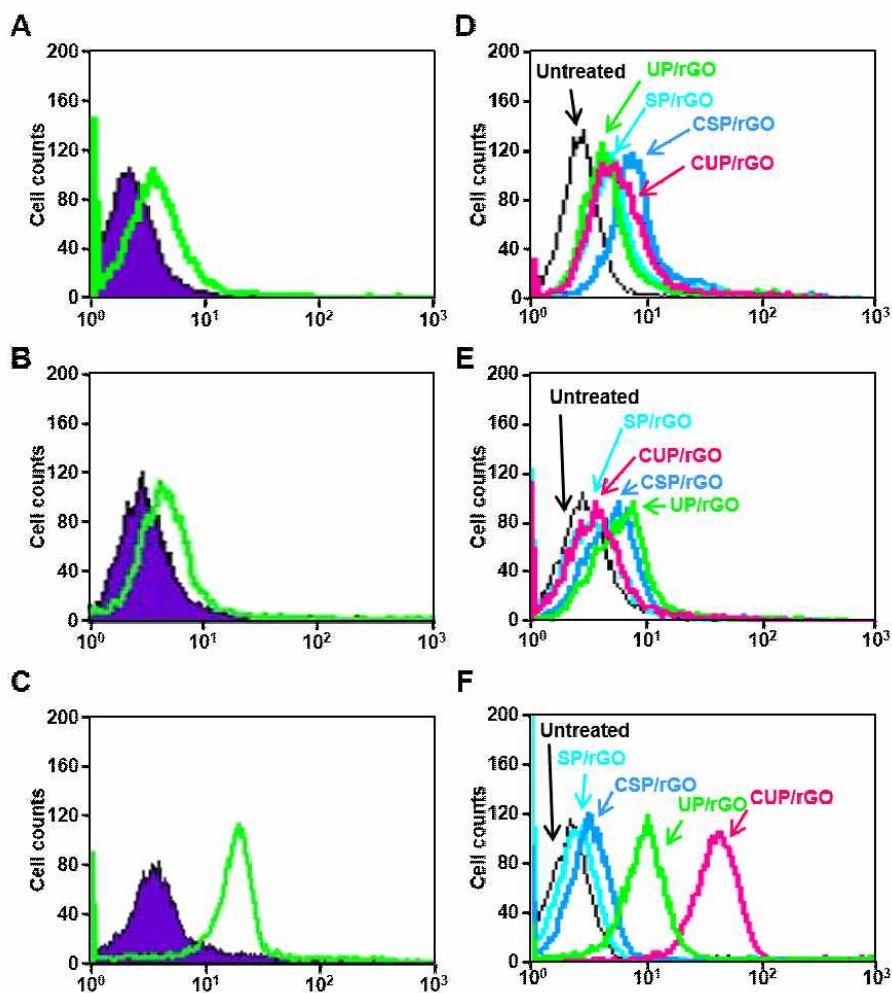


Fig. III-6. UPAR expression and targeting efficacy of CUP/rGO.

TCMK-1 (A), CCRF-CEM (B), or HT-29 (C) cells were stained with PerCP-eFluor 710-labeled anti-UPAR antibody and the receptor expression levels were analyzed using flow cytometry. Cells were left untreated or treated with SP/rGO, CSP/rGO, UP/rGO or CUP/rGO for 20 min and the representative flow cytometry data of TCMK-1 (D), CCRF-CEM (E), or HT-29 (F) cells are presented.

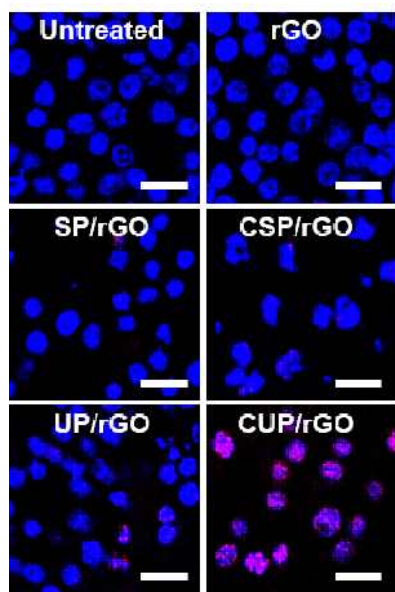


Fig. III-7. Uptake of CUP/rGO nanosheets in UPAR positive cancer cell.

HT-29 cells were left untreated or treated with plain rGO or SP/rGO, CSP/rGO, UP/rGO or CUP/rGO. After 20 min incubation, cellular fluorescence was observed by confocal microscopy. Scale bar indicates 25 μ m.

3.4. Photothermal anticancer effects of CUP/rGO

The NIR-responsive photothermal effect of CUP/rGO varied depending on the cell types. In UPAR-negative TCMK-1 (Fig. III-8A) and CCRF-CEM cells (Fig. III-8B), the increase of temperature upon NIR irradiation was similar among CUP/rGO-treated group and other peptide-modified rGO-treated groups. In UPAR-positive HT-29 cells, scrambled UPAR/rGO-treated cells showed the temperature of 40°C, similar to plain rGO. However, in after treatment with CUP/rGO, the temperature increased to 63.0 ±1.6 °C upon NIR irradiation in UPAR-positive HT-29 cells (Fig. III-8C).

Consistent with the cellular uptake patterns, the viability of the nanosheet-treated cells upon NIR irradiation showed dependence on the UPAR expression levels of cells. In TCMK-1 (Fig. III-9A) and CCRF-CEM (Fig. III-9B) cells, the viability of the cells were not significantly decreased upon NIR irradiation, regardless of treatment groups. In HT-29 cells, the viability of the cells was significantly reduced in CUP/rGO-treated group after NIR irradiation (Fig. III-9C). Fluorescent live cell staining revealed the lowest population of live cells after NIR irradiation of HT-29 cells treated with CUP/rGO (Fig. III-9D).

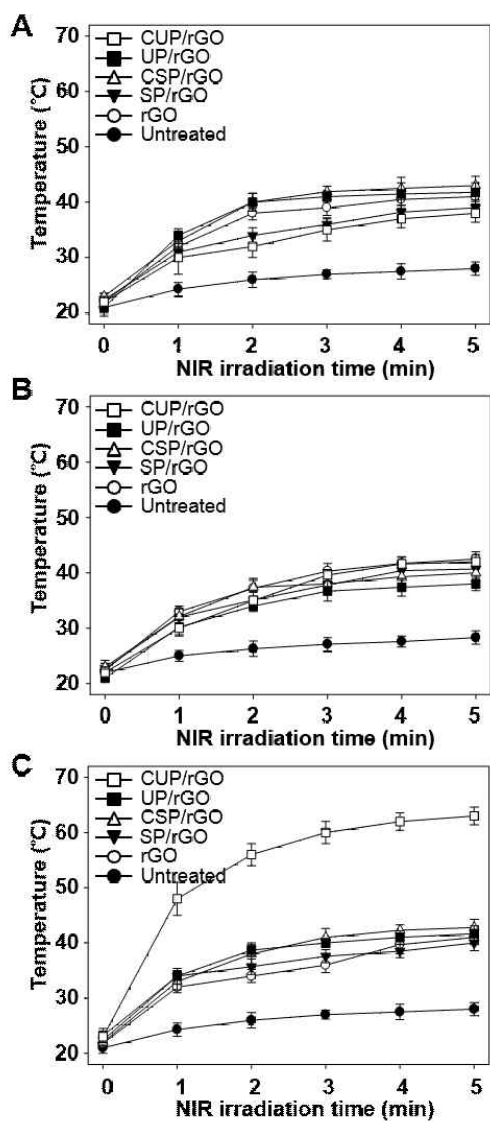


Fig. III-8. Photothermal activities of the surface-modified rGO following treated to cells.

TCMK-1 (A), CCRF-CEM (B), or HT-29 (C) cells were irradiated using NIR laser following treatment with the variously prepared rGO. The temperature increase aspects were observed real time using an IR thermal imaging camera.

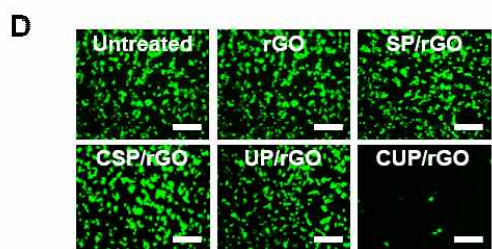
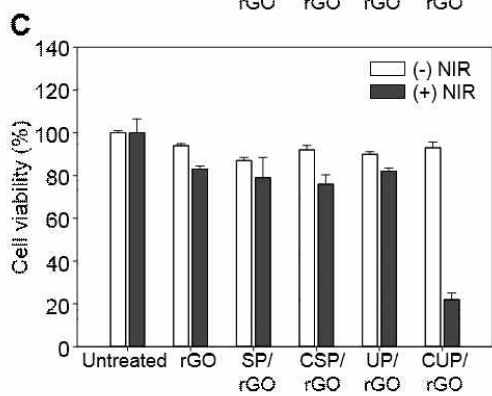
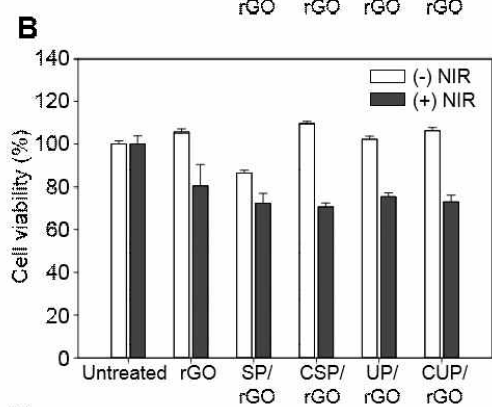
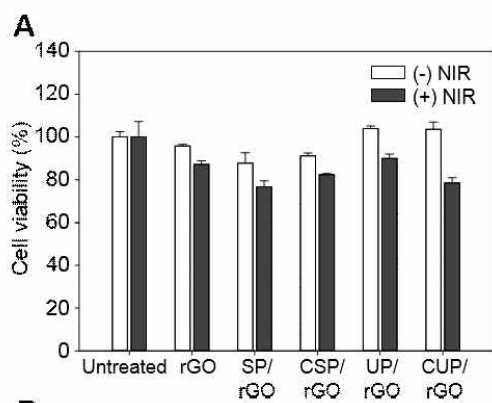


Fig. III-9. Photothermal anticancer effects.

TCMK-1, CCRF-CEM, or HT-29 cells were remained intact or treated with plain rGO or SP/rGO, CSP/rGO, UP/rGO or CUP/rGO and 808 nm laser irradiation was followed for some groups. After 24h, the viable TCMK-1 (A), CCRF-CEM (B), or HT-29 (C) cell population was measured using the MTT assay. Results are reported as the mean \pm SD of three independent experiments. Also, on the next day of NIR irradiation, live HT-29 cells were stained with calcein and observed using a fluorescence microscopy (D). The scale bar indicates 100 μ m.

3.6. Biodistribution of CUP/rGO nanosheets

The distribution patterns of CUP/rGO differed between CCRF-CEM tumor-bearing mice and HT-29 tumor-bearing mice. In CCRF-CEM tumor-bearing mice, the distribution of CUP/rGO to the tumor tissues was not notable (Fig. III-10A). However, in HT-29 tumor-bearing mice, the distribution of CUP/rGO to the tumor tissues was observed at various time points after intravenous administration (Fig. III-10B). In HT-29 tumor-bearing mice, the photon counts were recorded to be the highest in CUP/rGO compared to other peptide-modified nanosheets (Fig. III-10C).

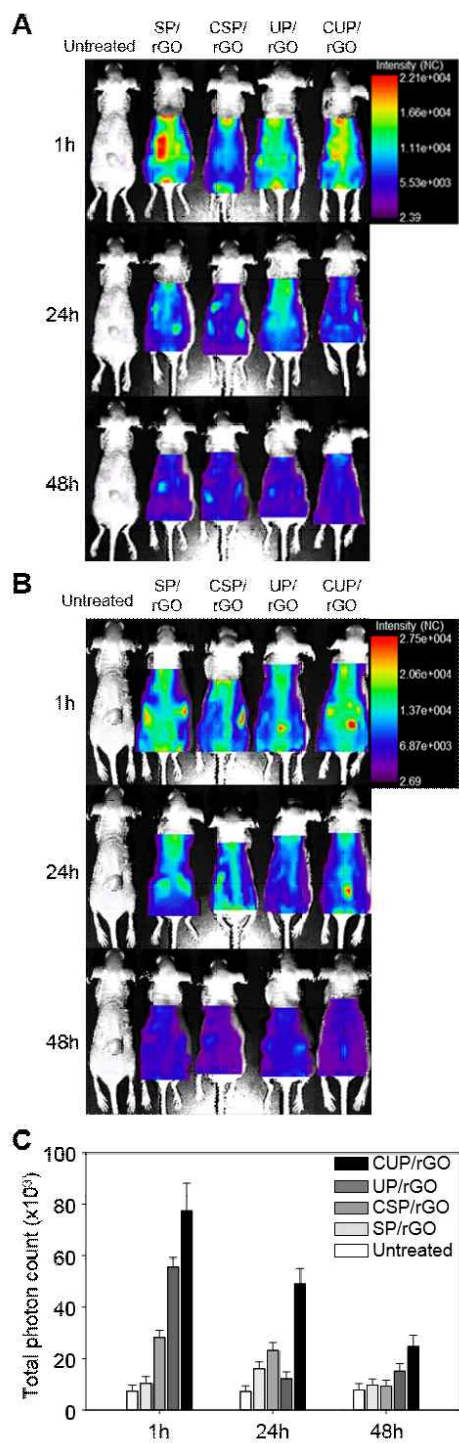


Fig. III-10. Biodistribution of Ce6 conjugates-loaded rGO in tumor-bearing mice.

CCRF-CEM (A) and HT-29 (B) tumor bearing mice were intravenously injected with SP/rGO, CSP/rGO, UP/rGO or CUP/rGO. After 1, 24, 48 h, the in vivo distribution of modified rGO was visualized using a molecular imaging system. Total photon counts in tumor sites of HT-29 tumor bearing mice were quantified (C).

3.7. In vivo photothermal antitumor effect of CUP/rGO nanosheets

Intravenous administration of CUP/rGO exerted photothermal antitumor effect upon NIR irradiation in HT-29 tumor-bearing mice, but not in CCRF-CEM tumor-bearing mice. In CCRF-CEM tumor-bearing mice, no difference was observed in the temperature of tumor sites upon NIR irradiation (Fig. III-11A). In contrast, in HT-29 tumor-bearing mice, the temperature of NIR-irradiated tumor tissues increased upto $55.4 \pm 1.6^{\circ}\text{C}$ (Fig. III-11B). In CCRF-CEM tumor-bearing mice, the tumor growth curves were not different regardless of treatment groups, and NIR irradiation (Fig. III-11C). However, in HT-29 tumor-bearing mice, the tumor ablation was observed in CUP/rGO-treated group upon NIR irradiation (Fig. III-11D). Immunohistochemistry revealed the lowest number of PCNA-positive population (Fig. III-12A,C) and the highest population of apoptotic cells (Fig. III-12B,D) in the tissues of tumors treated with CUP/rGO-treated group upon NIR irradiation.

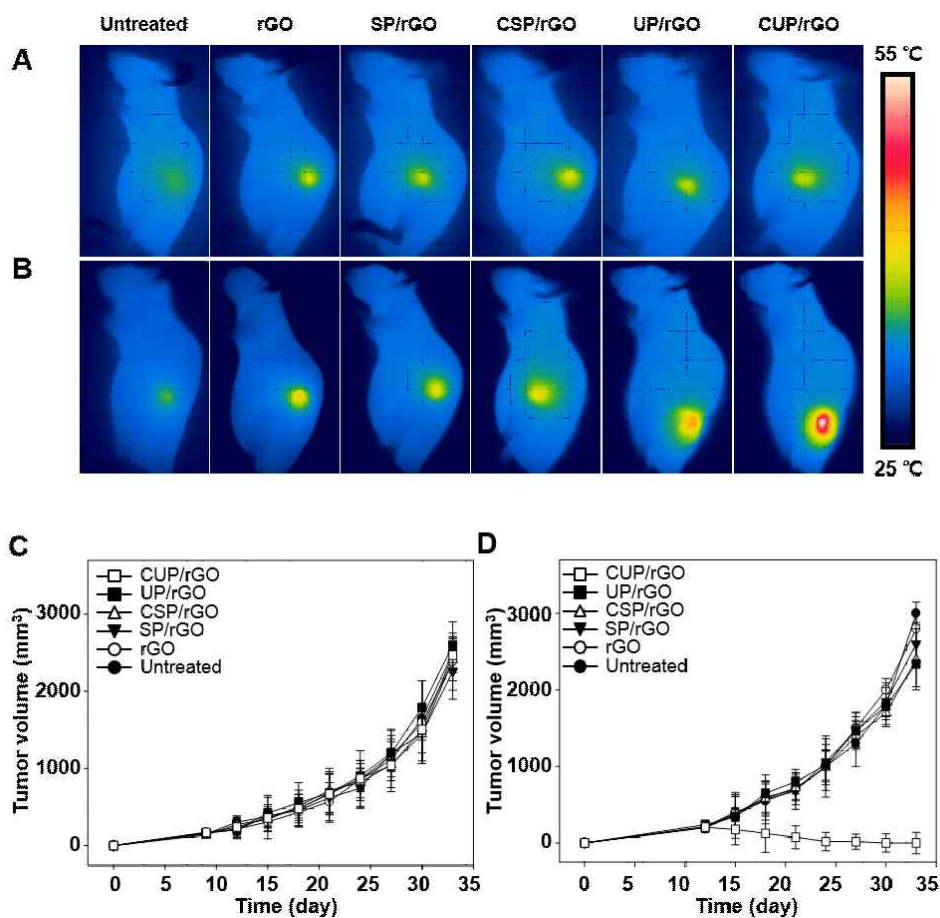


Fig. III-11. Photothermal effect of the CUP/rGO in mice.

CCRF-CEM (A) and HT-29 (B) tumor bearing mice were intravenously administered with rGO, SP/rGO, CSP/rGO, UP/rGO or CUP/rGO. After 4 hr, the tumor site was irradiated using 808 nm NIR laser for 10 min and the thermal images were obtained at the irradiation completion. The temperature of the tumor site was recorded every minute. Moreover, the tumor volumes of CCRF-CEM (C) and HT-29 (D) bearing mice were measured every 3 days.

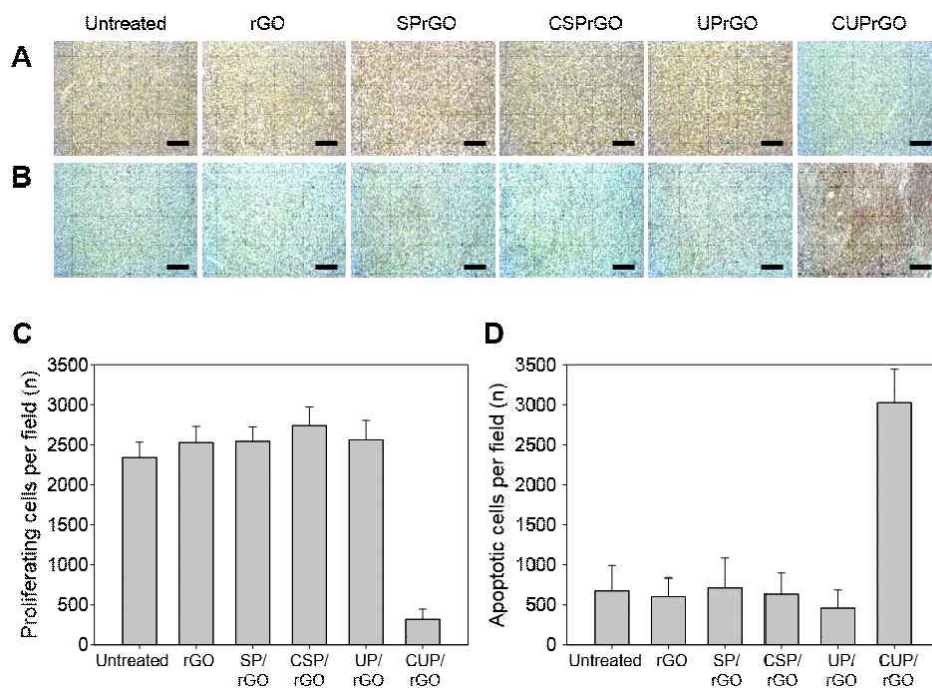


Fig. III-12. Immunohistochemistry of laser irradiated tumor tissues after various rGO treatment.

Tumor tissues of HT-29 tumor bearing mice were extracted and sectioned for anti-PCNA antibody immunostaining (A) and TUNEL assay (B) on day 33 after inoculation. The proliferating populations (C) and apoptotic cell numbers (D) in isolated tumor tissues were quantified. Scale bar indicates 100 μm .

4. Discussion

We demonstrated that CUP-loaded rGO nanosheets were activated in cathepsin L-rich tumor microenvironment and taken up by UPAR-positive tumor cells. The environment-responsive and UPAR-mediated delivery of CUP-loaded rGO nanosheets provided higher tumor distribution and enhanced NIR-responsive photothermal anticancer effects in cathepsin L-secreting and UPAR-positive HT-29 cells. This study indicates the potential of triple-controlled activation of nanomaterials by tumor microenvironment, overexpressed receptor, and light irradiation.

To tether various peptides onto rGO nanosheets by physical adsorption with similar affinity, we conjugated Ce6 to the N-terminal of peptide as an anchor molecule. Ce6 was shown to be adsorbed onto rGO nanosheets via π - π stacking and hydrophobic interactions [12,13]. Another use of Ce6 is to measure the loading efficiency of each peptide onto rGO nanosheets. The concentrations of unadsorbed Ce6 were measured to calculate the extent of quenched and bound Ce6-based conjugates.

Hydrophilic PEG moiety was inserted between Ce6 and peptide moiety to reduce the nonspecific adsorption of peptide moiety with rGO surfaces. Previously, PEG was introduced to reduce the interaction of ligand molecules with rGO nanosheets [14]. The prevention of nonspecific

interaction between peptide and rGO surfaces may contribute to retain the three dimensional conformation of peptide structure to be responsive to cathepsin L and binding to UPAR on target tumor cells.

For comparison with HT-29 cells which were positive with cathepsin L and UPAR, we used TCMK-1 and CCRF-CEM cells. TCMK-1 cells were derived from C3H normal mouse kidney cells, and double negative with cathepsin L and UPAR. CCRF-CEM cells are human T-cell acute lymphoblastic leukemia cell line, and also tested to be double negative with cathepsin L (Fig. III-5A) and UPAR (Fig. III-6B). In HT-29 cells, the secretion of cathepsin L cleaved CUP to UPAR-binding peptide, and make it bind to UPAR. Distinct presence of UPAR expression on colon cancer cells was previously reported [15].

Cathepsin L is one of the lysosomal proteases and it exerts proteolytic activity at low pH [16,17]. The acidic conditions are generated at extracellular space of tumors as the results of abnormal vascularization, accumulation of metabolites or hypoxia [18]. The low pH-adapted tumor cells proliferate for tumor progression and further metastasis [19]. Moreover, the secreted cathepsin L induce the generation of endostatin from collagen and then perform the critical role in ECM remodelling [20].

Biodistribution study reveal the higher tumor distribution of CUP/rGO in

HT-29 tumor-bearing mice. The higher tumor tissue distribution of CUP/rGO might be contributed to the cleavage of CUP by cathepsin L, and recovery of UPAR-binding activity of cleaved peptide in tumor microenvironment. Moreover, the overexpression of UPAR on HT-29 may contribute to the receptor-mediated endocytosis of UPAR-binding peptide on rGO nanosheets. Although we used rGO as a model photoresponsive nanomaterial of multi-controlled systems, CUP surface coating can be used to other photoresponsive nanomaterials [21] such as carbon nanotube [22], gold nanoparticle [23], metal-based nanostructure [24], and polydopamine nanoparticles [25]. Moreover, the concept of CUP can be applied to other nanomaterials loaded with anticancer drugs for tumor microenvironment and tumor cell-dual controlled delivery of anticancer chemotherapeutic drugs. In conclusion, we constructed triple controlled CUP/rGO for cathepsin L-sensitive, UPAR binding, and NIR-activable systems. The existence of CUP/rGO as inactive form in the bloodstream and activation to UPAR-binding form in tumor microenvironment can reduce the nonspecific distribution of CUP/rGO. Moreover, the NIR irradiation at tumor tissues can further control the photothermal anticancer effect of CUP/rGO focused on tumor sites.

5. References

- [1] Lee DJ, He D, Kessel E, Padari K, Kempter S, Lächelt U, Rädler JO, Pooga M, Wagner E. Tumoral gene silencing by receptor-targeted combinatorial siRNA polyplexes. *J Control Release*. 2016;244(Pt B):280-291.
- [2] Muthu MS, Kutty RV, Luo Z, Xie J, Feng SS. Theranostic vitamin E TPGS micelles of transferrin conjugation for targeted co-delivery of docetaxel and ultra bright gold nanoclusters. *Biomaterials* 2015;39:234-248.
- [3] Han H, Valdepérez D, Jin Q, Yang B, Li Z, Wu Y, Pelaz B, Parak WJ, Ji J. Dual enzymatic reaction-assisted gemcitabine delivery systems for programmed pancreatic cancer therapy. *ACS Nano*. 2017;11(2):1281-1291.
- [4] Belhadj Z, Ying M, Cao X, Hu X, Zhan C, Wei X, Gao J, Wang X, Yan Z, Lu W. Design of Y-shaped targeting material for liposome-based multifunctional glioblastoma-targeted drug delivery. *J Control Release*. 2017;255:132-141.
- [5] Kim MG, Shon Y, Kim J, Oh YK. Selective activation of anticancer chemotherapy by cancer-associated fibroblasts in the tumor microenvironment. *J Natl Cancer Inst*. 2017;109(1): djw186.

- [6] Sudhan D. R., Siemann D. W. Cathepsin L targeting in cancer treatment. *PharmacolTher.* 2015; 155: 105-116.
- [7] Urbich C., Heeschen C., Aicher A., Sasaki K., Bruhl T., Farhadi M. R., Vajkoczy P., Hofmann W. K., Peters C., Pennacchio L. A., Abolmaali N. D., Chavakis E., Reinheckel T., Zeiher A. M., Dimmeler S. Cathepsin L is required for endothelial progenitor cell-induced neovascularization. *Nat Med.* 2005; 11: 206-213.
- [8] Hau A. M., Leivo M. Z., Gilder A. S., Hu J., Gonias S. L., Hansel D. E. mTORC2 activation is regulated by the urokinase receptor (uPAR) in bladder cancer. *Cell Signal.* 2017;29:96-106.
- [9] Yang L., Sajja H.K., Cao Z., Qian W., Bender L., Marcus A.I., Lipowska M., Wood W.C., Wang Y.A. uPAR-targeted optical imaging contrasts as theranostic agents for tumor margin detection. *Theranostics.* 2014;4(1):106-118.
- [10] Hansen L., Larsen E. K. U., Nielsen E. H., Iversen F., Liu Z., Thomsen K., Pedersen M., Skrydstrup T., Nielsen N. C., Ploug M., Kjems J. Targeting of peptide conjugated magnetic nanoparticles to urokinase plasminogen activator receptor (UPAR) expressing cells. *Nanoscale.* 2013; 5: 8192-8201.

- [11] Miao W., Shim G., Kim G., Lee S., Lee H., Kim Y. B., Byun Y., Oh Y. Image-guided synergistic photothermal therapy using photoresponsive imaging agent-loaded graphene-based nanosheets. *J Control Release*. 2015;211:28-36.
- [12] Rong P., Yang K., Srivastan A., Kiesewetter D. O., Yue X., Wang F., Nie L., Bhirde A., Wang Z., Liu Z., Niu G., Wang W., Chen Xiaoyuan. Photosensitizer loaded nano-graphene for multimodality imaging guided tumor photodynamic therapy. *Theranostics*. 2014; 4 (3): 229-239.
- [13] Shen H., Zhang L., Liu M., Zhang Z. Biomedical applications of graphene. *Theranostics*. 2012; 2 (3): 283-294.
- [14] Mura S., Nicolas J., Couvreur P. Stimuli-responsive nanocarriers for drug delivery. *Nat Mater*. 2013; 12: 991-1003.
- [15] Boonstra M. C., van Driel P. B.A.A., van Willigen D. M., Stammes M. A., Prevo H. A.J.M., Tummers Q.R.J.G., Mazar A. P., Beekman F. J., Kuppen P.J.K., van de Velde C. J. H., Lowik C.W.G.M., Frangioni J.V., van Leeuwen F.W.B., Sier C.F.M., Vahrmeijer A.L. uPAR-targeted multimodal tracer for pre- and intraoperative imaging in cancer surgery. *Oncotarget* 2015; 6(16): 14260-14273.

- [16] Rozhin, J., Sameni, M., Ziegler, G., & Sloane, F. B. Pericellular pH affects distribution and secretion of cathepsin B in malignant cells. *Cancer Research*. 1994;54:6517-6525.
- [17] Webb, S. D., Sherratt, J. A., & Fish, R. G. Alterations in proteolytic activity at low pH and its association with invasion: a theoretical model. *Clin Exp Metastasis*. 1999;17:397-407.
- [18] Pouyssegur, J., Dayan, F., & Mazure, N. M. Hypoxia signalling in cancer and approaches to enforce tumour regression. *Nature*. 2006;441:437-443.
- [19] Provent, P., Benito, M., Hiba, B., Farion, R., Lopez-Larrubia, P., Ballesteros, P. Serial in vivo spectroscopic nuclear magnetic resonance imaging of lactate and extracellular pH in rat gliomas shows redistribution of protons away from sites of glycolysis. *Cancer Research*. 2007;67: 7638-7645.
- [20] Felbor U., Dreier L., A.R.Bryant R., L.Ploegh H., R.Olsen B., Mothes W. Secreted cathepsin L generates endostatin from collagen XVIII. *EMBO J*. 2000;19(6):1187-1194.
- [21] Jaque D, Maestro L. M., Rosal B. d., Haro-Gonzalez P., Benayas A., Plaza J. L., Rodríguez E. M., Sole J. G. Nanoparticles for photothermal therapies. *Nanoscale*. 2014; 6:

9494-9530.

- [22] Liang C., Diao S., Wang C., Gong H., Liu T., Hong G., Shi X., Dai H. Liu Z. Tumor metastasis inhibition by imaging-guided photothermal therapy with single-walled carbon nanotubes. *Adv Mater.* 2014; 26: 5646-5652.
- [23] Sun M., Liu F., Zhu Y., Wang W., Hu J., Liu J., Dai Z., Wang K., Wei Y., Bai J., Gao W. Salt-induced aggregation of gold nanoparticles for photoacoustic imaging and photothermal therapy of cancer. *Nanoscale.* 2016; 8: 4452-4457.
- [24] Yang Y., Liu J., Liang C., Feng L., Fu T., Dong Z., Chao Y., Li Y., Lu G., Chen M., Liu Z. Nanoscale metal-organic particles with rapid clearance for magnetic resonance imaging-guided photothermal therapy. *ACS Nano.* 2016; 10: 2774-2781.
- [25] Dong Z, Gong H, Gao M, Zhu W, Sun X, Feng L, Fu T, Li Y, Liu Z. Polydopamine nanoparticles as a versatile molecular loading platform to enable imaging-guided cancer combination therapy. *Theranostics.* 2016;6(7):1031-1042.

Chapter IV

**Enhanced delivery of nanomaterials by
overcoming inter-cellular junction
at tumor microenvironment**

1. Introduction

Tumor microenvironment is consisted of tumor and its neighbor such as extracellular matrix, immune cells. As materials at extracellular matrix (ECM), MMP [1,2] and collagen [3] have been well characterized. Although relaxing ECM components have been useful for nanoparticle deliveries, the approachable range is still restricted due to the dormancy of tumor itself [4]. Recently, delivery of nanomaterials to the center of the tumor has been highlighted for effective anticancer therapy.

In some tumors, tight junctions are exclusively expressed on the surface of cancer cells [5] and it is the main obstacle for drug delivery [6,7]. Among many subclasses of tight junctions, claudin4 is the most distinct receptor related to high density through cell-cell and cell-ECM interaction and it has been known to be paracellular barrier for drug delivery [8,9]. Tumor cells release component, such as cytokine [10,11], exosome [12,13] or enzymes [14,15], to metastasis or malignancy. Various tumor-secreting enzymes were identified.

Meprin is one of the enzymes playing an important role for ECM remodeling.

In this study, taking advantage of meprin and claudin4, we designed multi-controlled peptide-modified nanomaterials for activation in tumor microenvironment and sequential disruption of tight junctions between tumor cells. Using reduced graphene oxide (rGO) nanosheets as a model nanomaterial, we coated the surfaces of rGO with linear peptide which can be cleaved by tumor secreting meprin and release tight junction opening peptide in tumor microenvironment. The rGO would then flow through the loosened intercellular space. The delivery efficiency of the peptide-loaded rGO to tumor was evaluated as penetration depth by confocal microscopy and photothermal anticancer activity of rGO upon near infrared (NIR) irradiation (Fig. 1).

2. Materials and methods

2.1. Synthesis of peptide derivatives

The meprin sensitive and tight junction disrupting peptide was synthesized using standard Fmoc-mediated solid phase peptide synthesis methods on Wang resin. DSPE-PEG₂₀₀₀ was conjugated via a peptide bond to N-terminal of peptide by adding a 10% molar excess of DSPE-PEG₂₀₀₀ N-hydroxysuccinimide ester to peptide with diisopropylethylamine in dimethylformamide. After reaction at room temperature for 24 h, the resulting product was cleaved and deprotected with 95:2.5:2.5 by volume trifluoroacetic acid:H₂O:triisopropylsilane and was precipitated and washed several times with cold diethyl ether, dissolved in water, lyophilized, and stored as lyophilized powder at -20 °C. Crude, peptide mixture was purified by reverse-phase HPLC on a C8 column using acetonitrile/water mixture.

For cleavage activity evaluation, biotinylated and fluorescence probe labeled peptide was synthesized. The peptides were synthesized using standard Fmoc-mediated solid phase peptide synthesis methods on Wang resin. Biotin were conjugated via a peptide bond to N-terminal of peptide by adding a 10% molar excess of Biotin N-hydroxysuccinimide ester to peptide dissolved in 10 mM aqueous sodium carbonate buffer (pH 8.5). After reaction at room temperature for 24 h, the protecting group of Lysine were deprotected

with 2% hydrazine in dimethylformamide. FITC were conjugated by adding a 10% molar excess of FITC isothiocyanate to peptide with diisopropylethylamine in dimethylformamide. After reaction at room temperature for 24 h, the resulting products were cleaved and deprotected with 95:2.5:2.5 by volume trifluoroacetic acid:H₂O:triisopropylsilane and was precipitated and washed several times with cold diethyl ether, dissolved in water, lyophilized, and stored as lyophilized powder at -20 °C. Crude, peptides mixture were purified by reverse-phase HPLC on a C8 column using acetonitrile/water mixture.

For confocal imaging based penetration depth evaluation, Cy5.5 labeled peptide was synthesized. The peptides were synthesized using standard Fmoc-mediated solid phase peptide synthesis methods on Wang resin. Cy5.5 were conjugated via a peptide bond to N-terminal of peptide by adding a 10% molar excess of Cy5.5 N-hydroxysuccinimide ester to peptide with diisopropylethylamine in dimethylformamide. After reaction at room temperature for 24 h, the resulting products were cleaved and deprotected with 95:2.5:2.5 by volume trifluoroacetic acid:H₂O:triisopropylsilane and was precipitated and washed several times with cold diethyl ether, dissolved in water, lyophilized, and stored as lyophilized powder at -20 °C. Crude, peptides mixture were purified by reverse-phase HPLC on a C8 column

using acetonitrile/water mixture.

2.2. Preparation of rGO nanosheets

In tight junction disruption-induced photothermal activity improvement experiments as well as a nanocarrier, reduced graphene oxide nanosheets were synthesized using a modified Hummer's method [Miao et al., 2015]. In brief, graphite powder (0.5 g; Sigma-Aldrich) was added to cold H₂SO₄ (23 mL) then KMnO₄ (3 g; Sigma-Aldrich) and NaNO₃ (0.5 g; Sigma-Aldrich) were slowly added. The mixture was stirred on ice first and at 35 °C for an additional 1 h. Subsequently, triple-distilled water (TDW, 46 mL) was added to the mixture and then incubated at 90 °C for 1 h. To finalize the reaction, 30 % HCl (10 mL) and TDW (140 mL) were added. The resulting product was purified by three-time repeated centrifugation after 5% HCl-washing. The product is called graphene oxide (GO). GO was sonicated for 2 h to exfoliate GO layers to GO nanosheets. Unexfoliated GO layers were removed by centrifugation at 1600×g for 10 min. The GO nanosheets-containing supernatant was filtered through 0.2 µm polycarbonate membrane filters (Millipore Corp., Billerica, MA, USA) using an extruder (Northern Lipid, British Columbia, Canada). According to Li's method, the purified GO nanosheets were reduced to generate rGO nanosheets. Briefly,

GO nanosheets (5 mg/ml, 2 ml) were mixed with ammonia and hydrazine monohydrate containing TDW (8 ml) and stirred at 80 °C for 10 min; ammonia solution (28 wt.% in water, 0.5 ml; Junsei Chemical, Tokyo, Japan), hydrazine monohydrate (64 wt.% in water, 5 μ l; Sigma-Aldrich). The mixture was cool down to room temperature then the excess amount of hydrazine and ammonia were removed by dialysis (MWCO 100K; Spectrum Laboratories, Inc., Rancho Dominguez, CA, USA) against TDW. The resulting rGO nanosheets were stored at 4 °C until use.

2.3. Preparation of peptide tethered rGO nanosheets

The MEPTJ peptide was anchored on the surface of rGO nanosheets by mixing the same volume of each peptide (1.8 mmol/L) with the rGO nanosheets in TDW (1 mg/ml). The amount of peptide tethered on rGO nanosheets was quantified using an inorganic phosphate assay. Briefly, DSPE-PEG-Cy5.5 labeled-rGO or MEPTJ/rGO were digested with 400 ml of 5 M H₂SO₄ at 170 °C. Then the samples were cool down to room temperature and 100 ml of 30 % H₂O₂ was added. The mixtures were heated upto 170 °C to remove H₂O₂ completely. After cool the samples, 4.6 ml of 0.2 % ammonium molybdate and 100 ml of 15 % fresh ascorbic acid were sequentially added to the samples while vortexing. The resulting

mixtures were then boiled for 10 min at 100 °C then cooled down to room temperature. The absorbance at 830 nm was analyzed by a standard curve which was obtained using phosphorus standard solution (Sigma).

2.4. Cell culture

Mouse kidney (TCMK-1, Korean Cell Line Bank, Seoul, Republic of Korea) cells and human colon cancer (HT-29, Korean Cell Line Bank) were maintained in DMEM or RPMI-1640 (Welgene, Daegu, Republic of Korea), respectively. Each media was supplemented with 10% fetal bovine serum (FBS), 100 units/mL penicillin, and 100 µg/mL streptomycin. The cells were grown at 37°C in a humidified 5% CO₂ atmosphere.

2.5. Cleavage activity of meprin in cancer-conditioned media

The cleavage activity of meprin released from various tumor cells was evaluated using a streptavidin-biotin system. For this experiment, N-terminal FITC conjugated and C-terminal biotin conjugated peptides were synthesized. The prepared peptides were incubated in the streptavidin coated plate (Thermo Fisher Scientific Inc., Waltham, MA, USA) overnight at 37 °C. In the meantime, the supernatant of growing cell plate was normalized by dilution in culture media after cell counting. The peptide coated wells were

washed with cold phosphate buffered saline (PBS) two times and incubated with the normalized supernatant for 4 hr at 37 °C. Culture media was loaded into the well as a negative control. After washing with cold PBS two times, the fluorescence of each well was measured using a fluorescence microplate reader at an excitation wavelength of 485 and an emission wavelength of 525 nm. The fluorescence intensity value was quantified by subtracting the value from that of media containing well and the dividing it by the value of negative control. The calculated value was presented at percentage unit.

2.6. Expression of the Claudin4 receptors on the cancer cell surfaces

Flow cytometry was used to evaluate the expression of Claudin4 receptors on the surfaces of TCMK-1, mouse kidney cell or HT-29, colon cancer cell. To minimize non-specific binding, the cells were incubated for 1 h at room temperature with bovine serum albumin (BSA) containing PBS. After cold PBS wash one time, the fluorescein-conjugated mouse anti-claudin4 monoclonal antibody (R&D Systems, Inc., Minneapolis, MN, USA) was treated to the cells at a dilution of 1:100 and incubated at room temperature for 1 hr. Claudin4-expressing cell populations were identified using a Cell Quest Pro software-equipped BD FACSCalibur system (BD Bioscience, San

Jose, CA, USA).

2.7. Evaluation of intercellular resistance

The value of transepithelial electrical resistance (TEER) was measured using a portable Millicell-ERS voltohmmeter (Millipore UK Ltd., Watford, UK). The 0.4 μm sized pore-supported permeable membrane insert (Corning Inc., Troy, MI, USA) was assembled to a 24-well plate. The reservoir part was filled with 0.7 ml of culture media and TCMK-1 cells or HT-29 cells were seeded onto the membrane at a density of 1×10^5 . After incubation for two days at 37 °C with 5 % CO_2 , the membrane was completely filled with grown cells. Then the electrode was placed in the media of the cell-growing membrane insert and the reservoir part. The resistance was measured and displayed on the voltohmmeter in a real-time manner. In some groups, TJ peptide was treated to the membrane part at 100 μM or 400 μM and the TEER value was recorded at 1 h, 4 h, and 24 h post-dose.

2.8. Preparation of cell spheroid

To evaluate the penetration efficiency of TJ peptide, the HT-29 cells were grown to form a three dimensional spheroid. The spheroids were formed by a hanging drop method. On a hanging drop plate (Perfecta3D, 3D

Biomatrix, MI, USA), the cells were seeded at a density of 1×10^4 cells/well with a 50 μ l of warm culture media. 10 μ l of the supernatant was replaced with fresh warm culture media everyday. The spheroids were collected after three days from cell seeding.

2.9. In vitro penetrating evaluation of rGO nanosheets

Confocal microscopy imaging was conducted to analyze the depth of treated material on cell spheroid. The HT-29 cell spheroids were collected and washed two times with warm PBS. Then the spheroids were transferred to 96-well plate and treated with Cy5.5-conjugated DDDDD or Cy5.5-conjugated TJ peptide. After the incubation, the spheroids were washed with warm PBS two times and fixed by 10 % formalin-containing PBS for 20 min. Then the spheroids were transferred to 8-well chambered coverglass (Nalge Nunc Int., Rochester, NY, USA) and the images were obtained using confocal laser scanning microscope (LSM 5 Exciter, Carl Zeiss, Inc., Jena, Germany).

2.10. Photothermal effect on cell spheroids

Heat generation of delivered rGO nanosheets were evaluated using NIR irradiation. HT-29 cell spheroids were left untreated or treated with 400 μ M

of TJ peptide. After 4 hr of incubation at 37 °C, the spheroids were left untreated or treated with 48 µg of rGO nanosheets for additional 4 hr. Then the spheroids were washed with warm PBS and transferred to new EP tube with 100 µl of fresh media. The 808 nm continuous wave NIR diode laser (PSU-FC, ChangChun New Industries Optoelectronics Tech. Co., LTD, Changchun, China) irradiation was applied to the spheroids at an output power of 1.5 W/cm². During the 5 min irradiation, the temperature was monitored in a real time manner and the photothermal images were obtained every minute using an IR thermal imaging system (FLIR T420; FLIR Systems Inc., Danderyd, Sweden).

2.11. In vitro cell viability study

The cell viability was quantified by MTT assay. The material treated cell spheroids were washed with warm PBS and maintained in culture media. The next day, 500 µM of MTT (3-(4, 5-dimethylthiazol-2-yl)-2, 5-diphenyltetrazolium bromide, Sigma-Aldrich) solution was added to each spheroid for 2 hr at 37 °C. After removal of the media, the resulting crystals were dissolved in 200 µL of dimethyl sulfoxide (Sigma-Aldrich) and the absorbance was measured at 570 nm using a microplate reader (Tecan Group Ltd., Seestrasse, Mannedorf, Switzerland).

2.12. Biodistribution of MEPTJ/rGO

HT-29 cells were inoculated to the dorsal low right part of 5-week-old balb/c-nude female mice. To rGO group, Cy5.5 lipid tethered rGO or Cy5.5 lipid with MEPTJ tethered rGO was intravenously administered to rGO or rGO/TJ mice, respectively. Only to pre group, TJ peptide was intra-tumorally injected 4 hr in advance of systemic administration of MEPTJ/rGO. At 4, 12, 24, 48 h post-dose, the fluorescence signals of mice were scanned and the images were obtained using an eXploreOptix system (Advanced Research Technologies Inc., Montreal, Canada) with a laser power of 25 mW and a count time of 0.3 s/point.

2.13. In vivo penetration analysis

HT-29 cells were inoculated to the dorsal low right part of 5-week-old balb/c-nude female mice at a density of 5×10^6 cells. When the tumor volume reached to 90-120 mm³, the Cy5.5 labeled TJ peptide was locally injected to the tumor site. After 30 min, 4 hr and 24 hr, the fluorescence intensity was imaged using eXploreOptix system (Advanced Research Technologies Inc.). The distribution of fluorescence at tumor site was evaluated by Z-axis section.

3. Results

3.1. Expression of Claudin4 receptors on cell surface

Flow cytometric analysis was performed to evaluate the cell surface expression levels of claudin4. The fluorescence-labeled anti-claudin4 antibody was treated to the cells and the cellular claudin4 was fluorescently stained. The peak revealed that the expression levels of claudin4 receptor were significant in HT-29 (Fig. IV-2B) but negligible in TCMK-1 (Fig. IV-2A).

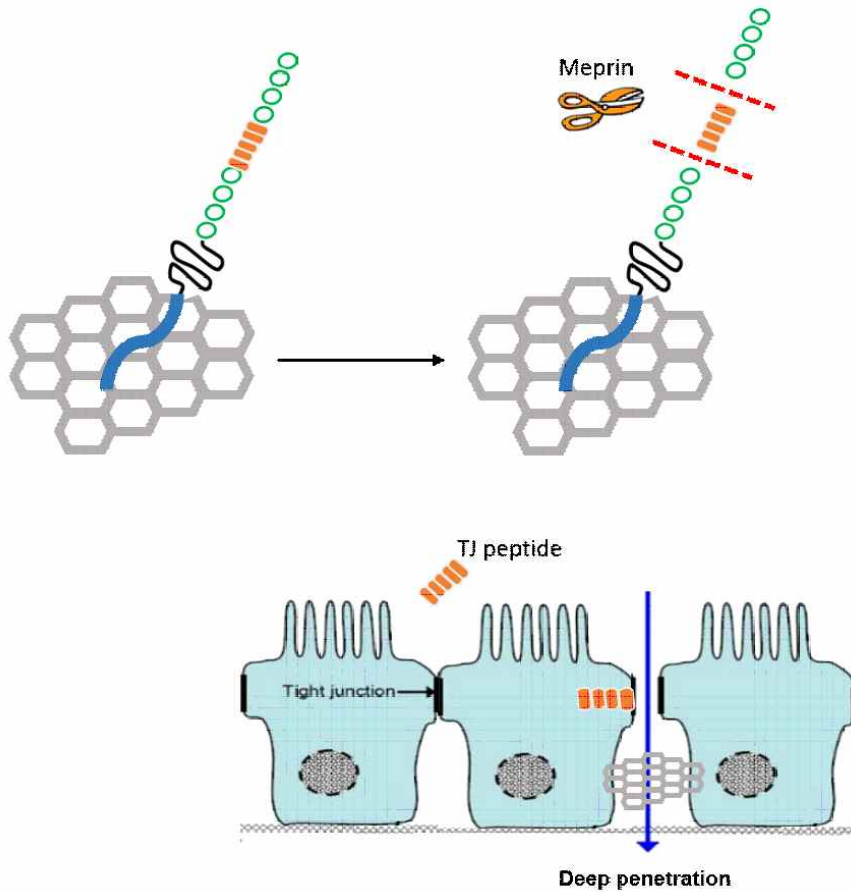
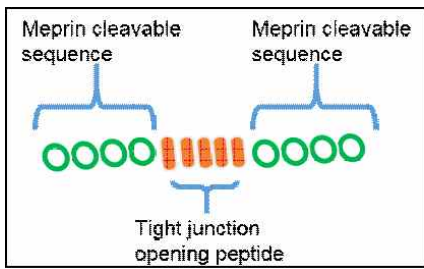


Fig. IV-1. Schematic diagram

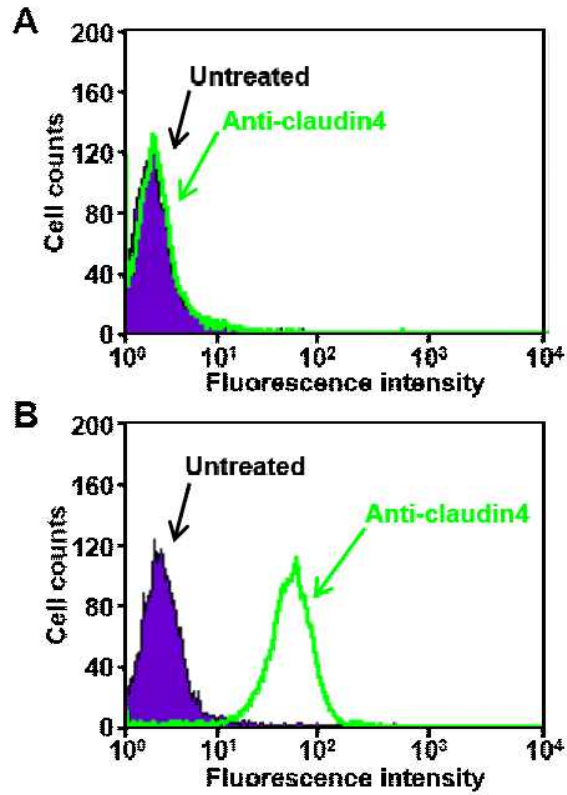


Fig. IV-2. Claudin4 expression

TCMK-1 (A) or HT-29 (B) cells were stained with a fluorescein-labeled anti-Claudin4 antibody and the fluorescence-positive cells were measured by flow cytometry.

3.2. Meprin-sensitive cleavage activity

The cleavable capability of meprin in cell conditioned media were significantly different among the cells. The fluorescence labeled peptide was bound to the streptavidin coated plated via streptavidin-biotin reaction. The fluorescence intensity was measured before and after the treatment of cell conditioned media. The intensity value was quantitatively analyzed and represented as percentage unit with negative control fresh media. While TCMK-1 showed only 18.7 % of peptide cutting activity, HT-29 cells showed 92% of target peptide cleavage functionality (Fig. IV-3).

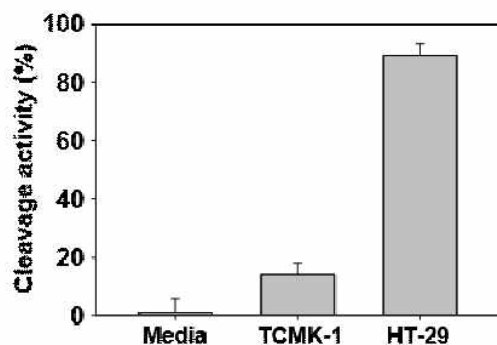


Fig. IV-3. Cleavage activity of cell secreting enzyme.

Using a streptavidin-biotin system, cell releasing enzyme was evaluated its cleavage functionality. Both end of meprin recognizing peptide sequence were modified as N terminal biotinylation and C terminal FITC conjugation. After the peptide was bound to the streptavidin coated plate, cell conditioned media was treated. Then the fluorescence intensity was analyzed using a fluorescence microplate reader. Media was used as a negative control.

3.3. Evaluation of tight junction disruption.

The peptide induced intercellular barrier loss was evaluated using a portable voltohmmeter. Prior to analysis the peptide effect to cell junction, the toxicity of TJ peptide was tested. TCMK-1 cells and HT-29 cells were seeded on a 48-well plate and incubated overnight. The TJ peptide was treated to the cells at a concentration up to 500 μM . On the next day, the cell survival rate was measured using MTT assay. Regardless of cell types, the cell viability was not affected at any treatment condition (Fig. IV-4).

To evaluate the TJ peptide effect on TEER value, TCMK-1 cells or HT-29 cells were grown confluent on a transwell plate (Fig. IV-5). The cell supernatant and the reservoir was exchanged with fresh media. The TJ peptide was treated at 0 μM , 100 μM or 400 μM and a blank transwell without cells was used as a negative control. No change was observed on the TEER value on TCMK-1 cells (Fig. IV-5A). However, the TEER value on HT-29 cells was decreased on dose- and time-dependent manner (Fig. IV-5B).

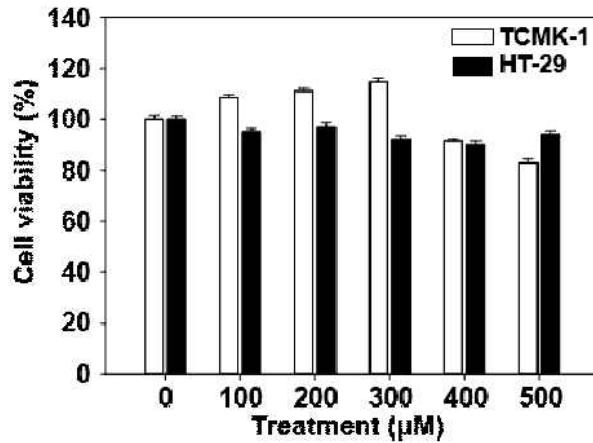


Fig. IV-4. Cytotoxicity of tight junction opening peptide.

Tight junction opening peptide was treated to the cells grown on a 48-well plate overnight. After 24h post treatment, the viability of cells were analyzed by MTT assay. The cell survival was maintained above 80 % at any peptide treatment concentration.

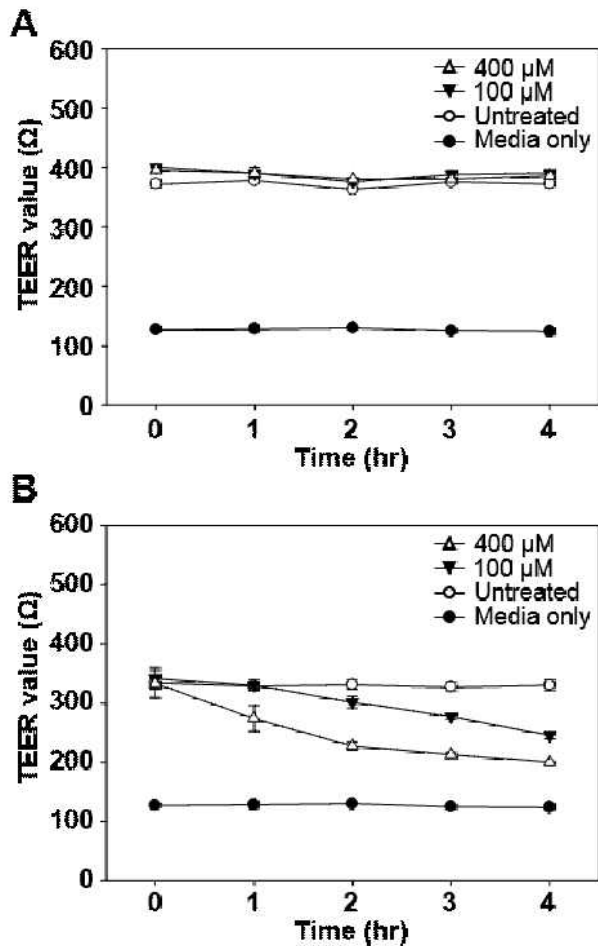


Fig. IV-5 TJ peptide effect on TEER value.

TCMK-1 (A) cells or HT-29 (B) cells were seeded on a transwell plate and fully grown. The media was freshly replaced and the TJ peptide was treated at 100 μ M or 400 μ M. Then the TEER value was measured every hour using a portable voltohmmeter device.

3.4. Photothermal effect on cell spheroids.

The rGO nanosheets could exert photothermal effect on cell spheroids and the extend could be vary depending on the regularity of intercellular junction. Upon NIR irradiation with 808 nm laser, rGO treated cells showed similar temperature increase regardless of TJ peptide treatment in no claudin4 expressing TCMK-1 cells (Fig. IV-6A). In contrast, rGO with TJ peptide treated cells showed over 50 °C as a final temperature which is 10 °C higher detected on rGO only treated HT-29 cells (Fig. IV-6B). In consistent with the photothermal temperature change pattern, the cell killing effect of rGO was improved (38.1%±8.6%) when treated with TJ peptide to claudin4 expressing cells (Fig. IV-7).

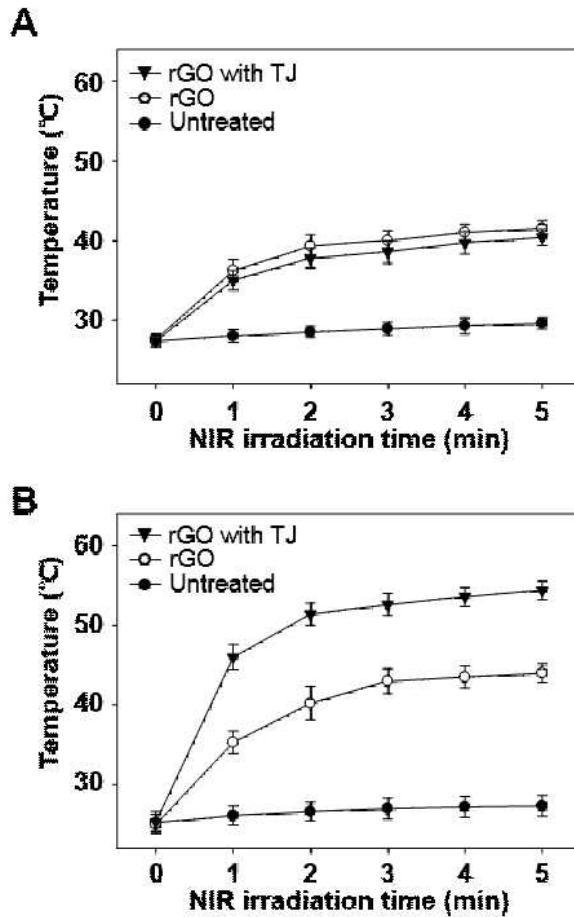


Fig. IV-6. In vitro photothermal effect on spheroids.

TCMK-1 cells (A) and HT-29 cells (B) were prepared as cell spheroids using a hanging-drop plate. TCMK-1 cell spheroids showed negligible temperature gap between rGO treated and rGO with TJ treated groups. On the other hand, the temperature of rGO with TJ treated HT-29 cell spheroids reached over 50 °C within 2 min of NIR irradiation and it was 10 °C higher than rGO treated HT-29 cell spheroids.

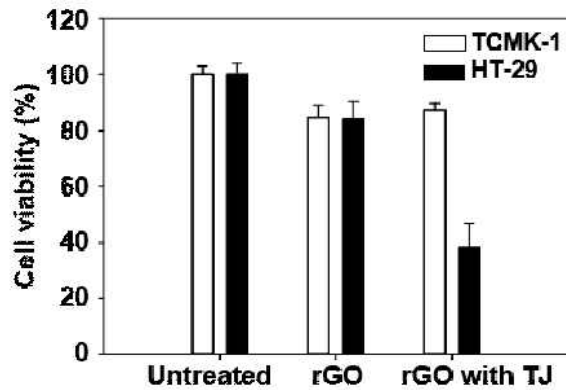


Fig. IV-7. In vitro anticancer effect

TCMK-1 cell spheroids and HT-29 cell spheroids were left untreated or treated with rGO only or rGO with TJ peptide. After 4 hr-treatment, 808 nm NIR irradiation was followed for 5 min and then the cell viability was evaluated. In TCMK-1 cells, cell survival was similar to all groups. In HT-29 cells, the live cell number of rGO with TJ peptide treatment group was lower than that of rGO only treated group.

3.5. In vitro penetration efficacy of TJ peptide

The TJ peptide binds and disrupts cell surface tight junctions. To evaluate the penetrating yield of TJ peptide, HT-29 cell spheroids were prepared. The spheroids were treated with Cy5.5 labeled DDDDD or the same fluorescence labeled TJ peptide. The treated spheroids then fixed and transferred to chambered coverglass. The treated peptide was visualized using confocal microscopy and the images were arranged according to the analyzing depth (Fig. IV-8). The 5D peptide was detected only at the border region of spheroids at all depths. In contrast, the TJ peptide was distributed to the center of the sectioned plane up to 120 μm from the bottom. The images demonstrate the enhanced penetration on claudin4 expressing cells was possible via TJ peptide treatment.

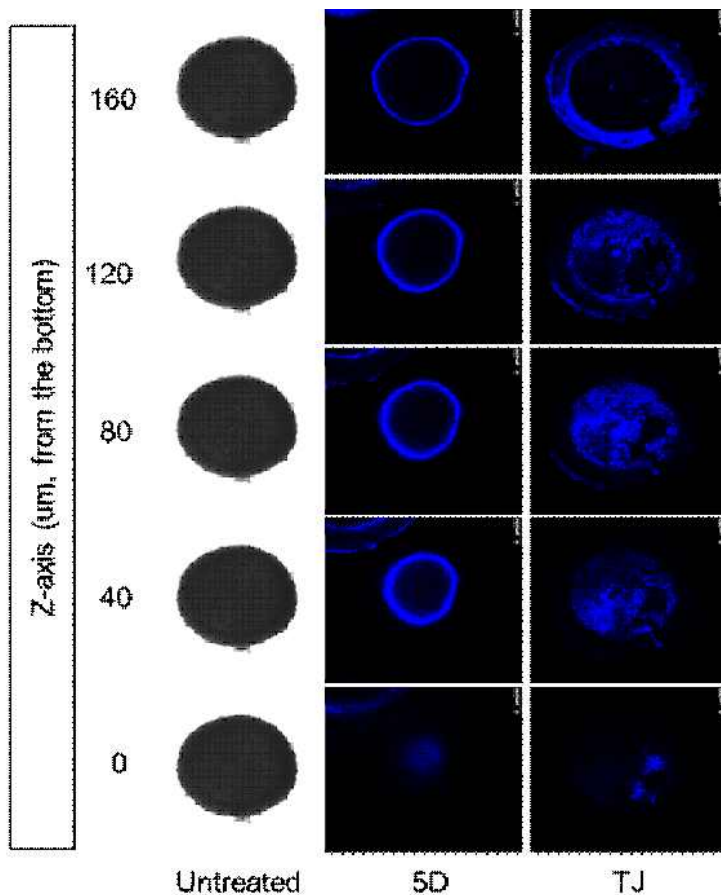


Fig. IV-8. Penetration analysis on cell spheroids.

Claudin4 expressing HT-29 cell spheroids were left untreated or treated with Cy5.5-5D or Cy5.5-TJ peptide. The spread peptide was visualized using confocal imaging after the spheroids were sectioned with 40 μm gap at Z-axis. The fluorescence intensity was observed only the spheroid border when 5D treatment. However, evenly distributed fluorescence intensity was observed on the TJ treated spheroid.

3.6. Biodistribution of MEPTJ tethered rGO nanosheets.

Localization of MEPTJ loaded rGO in HT-29 tumor bearing mice was examined. For molecular imaging, the same amount of Cy5.5-DSPE-PEG was administered to three rGO groups. To evaluate the TJ peptide mediated tight junction opening and efficacy of delivery improvement, TJ peptide was locally injected to the center of the tumor site 4 hr prior to systemic administration of MEPTJ/rGO. rGO treated mice showed nonspecific accumulation pattern. In MEPTJ/rGO treated mice, tumor specific significant fluorescence intensity was observed at 24 hr post-dose. In TJ pretreated mice, dramatically elevated fluorescence signal was detected at tumor site and the signal was relatively higher and maintained longer than no TJ pretreated mice (Fig. IV-9).

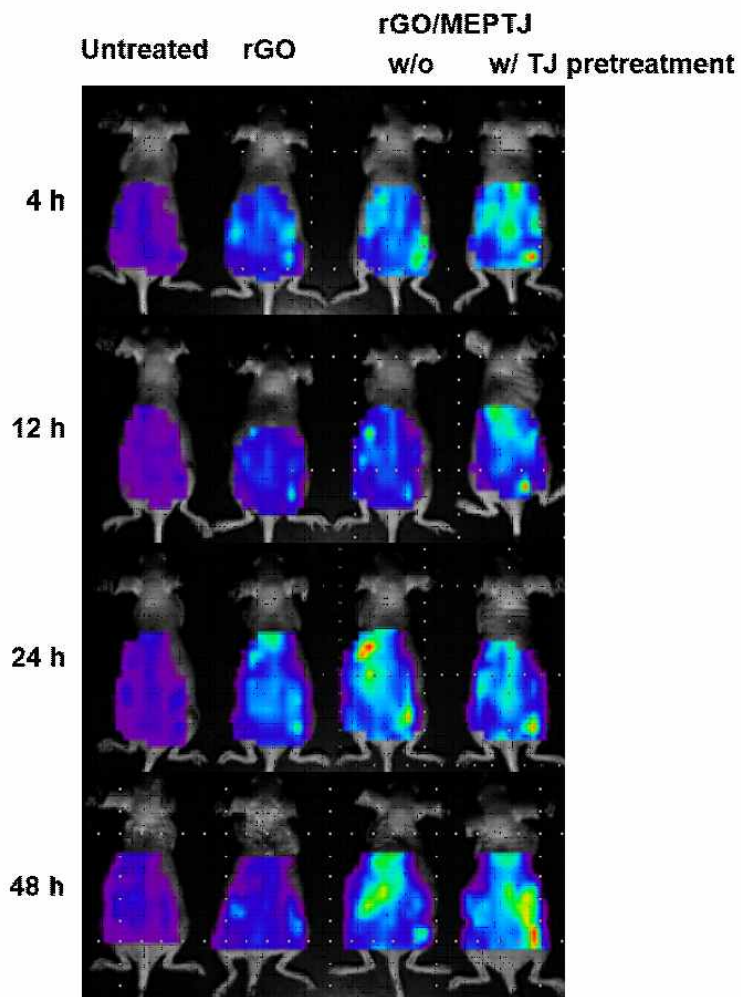


Fig. IV-9. Biodistribution of MEPTJ peptide loaded rGO nanosheets.

HT-29 tumor bearing mice were left untreated or treated with Cy/rGO, Cy/MEPTJ/rGO or Cy/MEPTJ/rGO with TJ pretreatment. In TJ pretreated mice, significantly high fluorescence signal was observed only at tumor site.

3.7. Penetration efficacy of TJ peptide in mice.

To evaluate the penetration capability of TJ peptide, fluorescence labeled TJ peptide was injected to the center of the tumor and the signal was examined up to 24 hr. HT-29 tumor bearing mice were constructed 5 days after HT-29 cells were inoculated at a density of 5×10^6 . Cy5.5-TJ peptide was injected to the tumor center and the molecular imaging was conducted 30 min, 4 hr and 24 hr post-dose. The locally accumulated signal was distributed to the tumor as time goes on (Fig. IV-10).

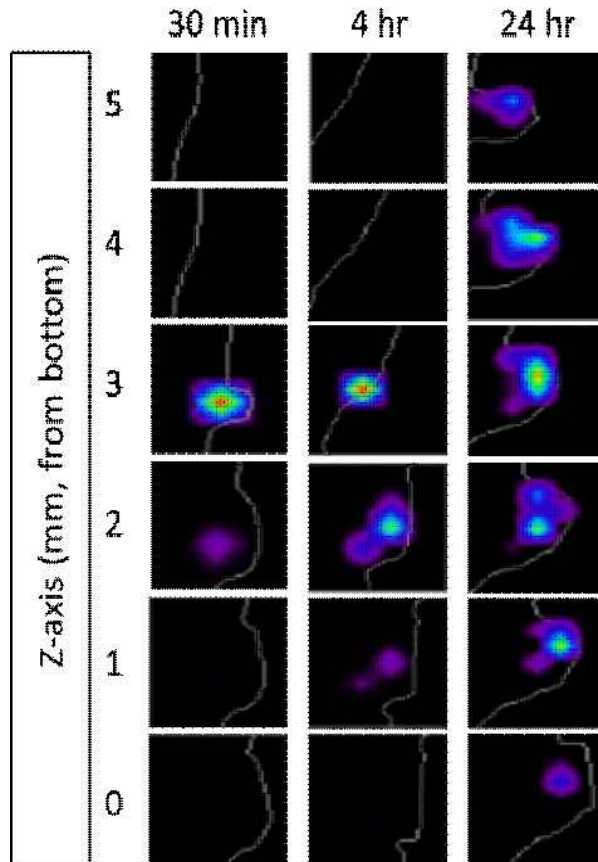


Fig. IV-10. In vivo penetration evaluation of TJ peptide.

HT-29 tumor bearing mice were locally treated with Cy5.5 labeled TJ peptide. Initially, fluorescence signal was detected at the center of the tumor. However, the signal was distributed all around the tumor site as time-dependent manner.

4. Discussion

In this study, the tight junction opening peptide played the critical role in remodeling extracellular matrix for nanoparticle delivery. The incorporation of meprin sensitive peptide increased the tumor specific peptide cleavage. Moreover, rGO nanosheets was delivered to deep cell spheroid and exerted photothermal anticancer effect.

The ultimate goal of this study was to evaluate the possibility that tight junction disruption mediated enhancement of nanomaterial delivery efficacy. Tight junction is major intercellular junction. Claudin4 is the cell surface transmembrane receptor its mechanism is well characterized and the expression on cancer cells is significant. The TJ peptide can bind to the secondary extracellular loop of claudin4. The binding site is originally cell to cell interaction region. Once the TJ peptide bound to the loop of claudin4, the cell misunderstood that it contacted to other cells. The number of cells decreased and space between cells were created. The formed gap supports the feasibility of nanomaterial delivery.

Though the claudin4 is highly expressed on tumor cell surfaces, claudin4 is found in normal cells as well. For tumor specific tight junction opening, additional tumor recognizing molecule was required. Tumor cells express

various proteins on their surfaces and releasing proteins (cytokine, enzyme, etc) as well. Meprin is one of the tumor cell secreting enzyme which is responsible for ECM dysfunction. By designing the peptide having TJ peptide as a core and conjugating meprin sensitive peptide at both ends, TJ peptide could be protected till it reaches to the target tumor site and its activation at normal tissues could be highly inhibited.

Delivery of rGO nanosheets into claudin4-overexpressing HT-29 cell spheroid was enhanced by opening the tight junctions (Fig. IV-6). The TJ peptide mediated gap formation was previously reported. This study demonstrated the TJ peptide worked on 3D cell spheroid and it resulted in enhanced photothermal effect (Fig. IV-7). The application of TJ peptide is expected to be broaden for various therapeutic strategy via effective nano-range material delivery.

Moreover, the tumor specific accumulation of rGO nanosheets was revealed by molecular imaging and the enhanced molecule accumulation was observed in MEPTJ loaded rGO treated mice (Fig. IV-9). When TJ peptide was pretreated to tumor site, the molecular accumulation at tumor was enhanced and it was maintained upto 48 hr. Delivery of high amount of TJ peptide to target site would be considered to enhance the delivery efficacy of drug loaded material and therapeutic effect.

Tight junction is composed of integral membrane proteins such as claudin and it contributes to epithelial tumorigenesis. Dysregulation of the barriers occurs mainly due to TJ proteins, protein kinase C signaling, and endocytosis of junctional proteins.

The loss of TJ significantly affects cell permeability and polarity resulting in making tumor cells invasive. The lack of cell to cell adhesion in neoplastic epithelium contributes the stroma invasion [16] and the enhanced TJ permeability improving tumor cell penetration through mesothelial cells [17]. Not only colorectal cancer [18,19] but various human diseases are linked to the disruption of structural and functional tight junction. Ovarian cancer [20], breast cancer [21], bladder cancer [22], nonalcoholic fatty liver disease [23], or else can be treated effectively through understanding of the mechanism between tight junction and disease development. Due to the high clinical importance, tight junction would be the major research target and promising key for bench-to-clinic.

In this study, TJ peptide was evaluated for in vitro and in vivo application of therapeutics. TJ peptide mediated tight junction disruption was examined in cell level by TEER value measurement and confocal imaging of 3D cell spheroid. In claudin4 overexpressing and meprin secreting HT-29 cell bearing mice model, the molecular imaging of biodistribution and Z-axis

based molecular distribution revealed that dual tumor microenvironment targeting strategy significantly increase the tumor specificity and penetration efficacy. Although the photothermal effect of delivered rGO nanosheets was examined in this study, the application of TJ peptide could be vary by replacing nanocarriers and drug loading. Results in this study suggest the potential of TJ peptide administration for solid and heterogenous tumor treatment.

5. References

- [1] Gialeli C., Theocharis A.D., Karamanos N.K. Roles of matrix metalloproteinases in cancer progression and their pharmacological targeting. *FEBS J.* 2011;278:16-27.

- [2] Hu J., Liu L., Li Z., Zhuo R., Zhang X. MMP-responsive theranostic nanoplatform based on mesoporous silica nanoparticles for tumor imaging and targeted drug delivery. *J. Mater. Chem. B.* 2016;4:1932.

- [3] Grossman M., Ben-Chetrit N., Zhuravlev A., Afik R., Bassat E., Solomonov I., Yarden Y., Sagi I. Tumor cell invasion can be blocked by modulators of collagen fibril alignment that control assembly of the extracellular matrix. *Cancer Res.* 2016;76(14):4249-4258.

- [4] Fukumura D., Jain R.K. Tumor microenvironment abnormalities: causes, consequences, and strategies to normalize. *J. Cell. Biochem.* 2007;101:937-949.

- [5] Webb P.G., Spillman M.A., Baumgartner H.K. Claudins play a role in normal and tumor cell motility. *BMC Cell Biol.* 2013; 14:19.

- [6] Kubo T., Sugimoto K., Kojima T., Sawada N., Sato N., Ichimiya S. Tight junction protein claudin-4 is modulated via Np63 in human

keratinocytes. *Biochem. Biophys. Res. Commun.* 2014;455:205-211.

- [7] Mitchell L.A., Ward C., Kwon M., Mitchell P.O., Quintero D.A., Nusrat A., Parkos C.A., Koval M. Junctional adhesion molecule A promotes epithelial tight junction assembly to augment lung barrier function. *Am J Pathol.* 2015;185:372-386.
- [8] Hou J., Renigunta A., Yang J., Waldegger S. Claudin-4 forms paracellular chloride channel in the kidney and requires claudin-8 for tight junction localization. *Proc Natl. Acad. Sci. USA.* 2010;107:18010-18015.
- [9] Van I.C., Rahner C., Anderson J.M. Regulated expression of claudin-4 decreases paracellular conductance through a selective decrease in sodium permeability. *J. Clin. Invest.* 2001;107:1319-1327.
- [10] Wilson J., Balkwill F. The role of cytokines in the epithelial cancer microenvironment. *Semin Cancer Biol.* 2002;12:113-120.
- [11] Koontongkaew S., Amornphimoltham P., Yapong B. Tumor-stroma interactions influence cytokine expression and matrix metalloproteinase activities in paired primary and metastatic head and neck cancer cells. *Cell Biol Int.* 2009;33:165-173.
- [12] Hoshino A., Costa-Silva B., Shen T., Rodrigues G., Hashimoto A.,

Mark M.T., Molina H., Kohsaka S., Giannatale A.D., Ceder S., Singh S., Williams C., Soplop N., Uryu K., Pharmed L., King T. Bojmar L., Davies A.E., Ararso Y., Zhang T., Zhang H., Hernandez J. Weiss J.M., Dumont-Cole V.D., Kramer K., Wexler L.H., Narendran A., Schwartz G.K., Healey J.H., Sandstrom P., Labori K.J., Kure E.H., Grandgenett P.M., Hollingsworth M.A., Sousa M.D., Kaur S., Jain M., Mallya K., Batra S.K., Jarnagin W.R., Brady M.S., Fodstad O., Muller V., Pantel K., Minn A.J., Bissell M.J., Garcia B.A., Kang Y., Rajasekhar V.K., Ghajar C.M., Matei I., Peinado H., Bromberg J., Lyden D. Tumour exosome integrins determine organotropic metastasis. *Nature* 2015;527:329-335.

[13] Kahlert C., Kalluri R. Exosome in tumor microenvironment influence cancer progression and metastasis. *J. Mol. Med.* 2013;91(4):31-437.

[14] Baker A-M., Bird D., Lang G., Cox TR., Eler JT. Lysyl oxidase enzymatic function increases stiffness to drive colorectal cancer progression through FAK. *Oncogene.* 2013;32:1863-1868.

[15] Heinecke J.L., Ridnour L.A., Cheng R.Y.S., Switzer C.H., Lizardo M.M., Khanna C., Glynn S.A., Hussain P. Young H.A., Ambs S., Wink D.A. Tumor microenvironment-based feed-forward regulation of NOS2 in breast cancer progression. *PNAS.* 2014;111(17):6323-6328.

[16] Kominsky S.L., Argani P., Korz D., Evron E., Raman V., Garrett E.,

Rein A., Sauter G., Kallioniemi O.P., Sukumar S. Loss of the tight junction protein claudin-7 correlates with histological grade in both ductal carcinoma in situ and invasive ductal carcinoma of the breast. *Oncogene*. 2003;22:2021-2033.

[17] Tobioka H., Sawada N., Zhong Y., Mori M. Enhanced paracellular barrier function of rat mesothelial cells partially protects against cancer cell penetration. *Br. J. Cancer*. 1996;74:439-445.

[18] Soler A.P., Miller R.D., Laughlin K.V., Carp N.Z., Klurfeld D.M., Mullin J.M. Increased tight junctional permeability is associated with the development of colon cancer. *Carcinogenesis*. 1999;20:1425-1431.

[19] Shiou S.R., Singh A.B., Moorthy K., Datta P.K., Washington M.K., Beauchamp R.D., Dhawan P. Smad4 regulates claudin-1 expression in a transforming growth factor-beta-independent manner in colon cancer cells. *Cancer Res*. 2007;67:1571-1579.

[20] D'Souza T., Agarwal R., J.Morin P. Phosphorylation of claudin-3 at threonine 192 by cAMP-dependent protein kinase regulates tight junction barrier function in ovarian cancer cells. *J Biol Chem*. 2005;280(28):26233-26240.

[21] Martin T.A., Watkins G., Mansel R.E., Jian W.G. Loss of tight junction plaque molecules in breast cancer tissues is associated with a

poor prognosis in patients with breast cancer. *Eur J Cancer*. 2004;40:2717-2725.

[22] Boireau S., Buchert M., Samuel M.S., Pannequin J., Ryan J.L., Choquet A., Chapuis H., Rebillard X., Avances C., Ernst M., Joubert D., Mottet N., Hollande F. DNA-methylation-dependent alterations of claudin-4 expression in human bladder carcinoma. *Carcinogenesis*. 2007;28:246-258.

[23] Miele L., Valenza V., Torre G.L., Montalto M., Gammarota G., Ricci R., Masciana R., Forgione A.m Gabrieli M.L., Perotti G., Vecchio F.M., Rapaccini G., Gasbarrini G. Day C.P., Grieco A. Increased intestinal permeability and tight junction alterations in nonalcoholic fatty liver disease. *Hepatology*. 2009;49:1877-1887.

Conclusion

As the tumor site targeting attracted huge interest of researchers, a wide range of targetable molecule has been identified and utilized to see their applicable capability for therapeutic purpose. Tumor microenvironment including cellular factors and their surroundings was significantly highlighted and the active drug delivery systems have been moving forward to understand and effectively control the environment.

DNA nanostructures were designed for cancer cell targeting and photodynamic therapy. The successive guanine sequences were introduced to the end of sgc8 aptamer sequence for G-quadruplex structure formation by self-assembly. The photoresponsive agent methylene blue was loaded onto the internal space of G-quadruplex for killing cells. The MB loaded DNA complexes specifically recognized the membrane protein PTK7 on CCRF-CEM cells and the following LED irradiation generated ROS resulting in ROS-induced CCRF-CEM cell deaths.

The cyclic peptide loaded rGO was developed for serial control of the complex activation and photothermal therapy. As some of the peptide sequence was designed for cell surface receptor (UPAR) targeting and some part of the peptide was substrate for the cancer releasing enzyme cathepsin L, the activation of the peptide was controlled serially depending on the TME condition. Once the peptide/rGO complex reached to the tumor site, CTSL digested its substrate and the rGO was accumulated into the UPAR overexpressing cancer cells then following NIR irradiation exerted hyperthermal cancer cell killing effect.

The environmental barriers were evaluated for enhancing drug delivery by making it unbalanced. Tight junctions between cancer cells are the major obstacles restricting drug delivery efficiency. By administering TJ binding peptide, the TEER value at claudin4 overexpressing tumor site dropped. Furthermore, the TJ-mediated penetration improvement was evaluated on cell spheroid models and tumor cell bearing mice.

In our studies, functional nanostructures for drug delivery were developed. The drug-loaded nanostructures were demonstrated their specificity to TME such as tumor cell surface proteins, tumor ECM-rich enzymes, and cell-to-cell junctional barriers. Not only the external stimuli shown here, also other external or endogenous stimuli can be considered for effective therapy. The applicable range would be more broaden as multi-targetable or controllable therapeutic systems. Overall, these TME specific functional nanostructures are promising treatment strategies for various human diseases.

요약

종양미세환경 특이적 나노구조체 기반 약물 전달

서울대학교 대학원

약학과 약제과학전공

진혜림

종양미세환경은 종양조직 및 그와 관련된 면역세포, 세포외기질, 분비 단백질 등을 종합적으로 일컫는 말로써, 효과적인 질병치료를 위하여 반드시 고려되어야 하는 핵심요소로 최근 그 중요성이 주목되고 있다. 암 세포 표면에 다량 발현하는 단백질을 타겟으로 하여 항암 물질을 전달했던 표적 약물 전달은 그 범위가 종양미세환경으로 확장되었으며, 암에 대한 포괄적인 이해를 기반으로 한 종양미세환경 특이적 표적약물전달은

항암제의 치료효과 증진 및 여러 질병 치료에의 적용도 기대되는 유망한 전략으로 부상하였다.

Protein tyrosine Kinase 7 (PTK7)에 특이적으로 결합하는 것으로 알려진 DNA aptamer의 말단에 연속적인 15개의 구아닌 서열을 연장하였고, 이는 self-assembly에 의해 DNA nanostructure가 되었다. 본 핵산 나노 구조에는 특이적인 G-quadruplex가 있어 메틸렌블루 (MB)를 탑재하였고, PTK7 과발현 세포주에 항암제 전달 효율을 증진시켰다. PTK7 과발현 세포주내로 전달된 MB는 LED 조사에 의해 활성산소 (reactive oxygen species)를 발생시켜 타겟 암세포주를 효과적으로 사멸시켰다.

Ce6 (Chlorin e6)를 매개로 cyclic 펩타이드를 만들어 환원 그래핀 나노시트 (rGO)에 수식하였다. Cyclic 펩타이드는 특정 종양미세환경에 다량 존재하는 효소에 의해 잘리고, 그로 인해 활성화된 펩타이드 서열은 특정 수용체를 과발현하는 암세포를 표적하여 rGO와 함께 해당 세포 안으로 전달된다. 근적외선은 암세포 내에 축적된 rGO에 조사되어 온도증가를 통한 세포사멸을 보였다. Cyclic 펩타이드가 수식된 rGO는 암세포가 이식된 쥐에 정맥주사를 통해 암조직에 효과적으로 축적되었고, 국소적 근적외선 조사에 의한 rGO의 광열효과는 암조직을 완전히 제거하였다.

암세포는 tight junction에 의해 과밀하게 암조직으로 성장하는데, 이는 치료물질이 암조직의 내부까지 도달하는 데 큰 장벽으로 인식되었다. rGO에 tight junction에 결합하는 펩타이드를 수식하였고, 이를 3차원적으로 세포를 배양한 스페로이드에 처리하여 투과 깊이의 향상 및 광열치료효과 증진을 확인하였다. 또한, 암조직이 이식된 쥐에 정맥주사 하였을 때, 해당 물질은 암조직에의 축적이 월등했고, 암조직 중심부까지 침투됨을 여러 동물 이미징 기법을 통해 평가하였다.

주요어: Tumor microenvironment, targeted drug delivery, DNA nanostructure, reduced graphene oxide, photodynamic therapy, photothermal therapy, tight junction, penetration depth